Investigating Energy Transport in High Density Plasmas Using Buried Layer Targets

Mohammed Shahzad

Doctor of Philosophy

University of York
Physics

May 2015

Abstract

The work presented in this thesis investigates energy transport in laser irradiated solid targets containing a diagnostic buried iron layer. Energy transport in laser-plasmas is important to inertial confinement fusion and other applications, for example laser ablation, particle acceleration and x-ray production.

The steep temperature and density gradients between the critical density (maximum penetration density for the laser) and ablation surface, plus the role of fast electron and radiation make energy transport in laser-plasmas a complex, non-linear issue. Laser energy can be transported into a solid target by thermal conduction, hot electron heating and radiation transport. To understand the interplay between these non-linear heating processes it is important to accurately characterise plasma conditions as the energy transport occurs. An experiment conducted at the Lawrence Livermore National Laboratory, USA irradiated buried iron layer targets using a 2 ps, 10^{17} Wcm^{-2} laser with the subsequent L-shell iron emission recorded using a high resolution (resolving power $\simeq$ 500) grating spectrometer. The HYADES 1D hydrodynamic fluid code and the PrismSPECT collisional-radiative code were used to simulate the plasma conditions and the L-shell iron emission. A comparison between the simulated spectra and experimentally recorded L-shell emission suggests that the iron layer is heated instantaneously by hot electrons and radiation transport and that this modifies thermal electron conduction. The thermal flux limiter and laser energy-hot electron conversion efficiency have been determined by comparing experimentally recorded L-shell emission to simulated synthetic spectra. As the iron layer expands and cools, the population of lower ionisation states increases. A novel technique has been developed to characterise the electron temperature and density from L-shell emission spectra using the Saha-Boltzmann equation and multiple line ratios of adjacent ionisation states.

An experiment at the LASERIX facility, France used an extreme ultraviolet (EUV) laser as a back-lighter, to probe high density laser irradiated buried iron layer targets. The transmission through the iron layer was simulated using TOPS, PROPACEOS, IMP and HYADES opacity models. This investigation has found that higher opacities are required for plasmas at 20 eV and 0.3 gcm^{-3} in order to account for the drop in transmission at 20 ps after laser irradiation. Radiation transport dominates the heating of the buried iron layer when irradiated by a well defined prepulse. The expanding coronal preplasma efficiently produces hot electrons, however because of the larger stopping distance associated with 'superthermal' electrons, the heating due to hot electrons is negligible compared to the radiation heating effect.

Contents

List of Figures

Acknowledgements

First and foremost I would like to thank my supervisor, Professor Greg Tallents for his guidance and support to complete the work presented here.

Although the road to a PhD was long and steep, the members of the York Plasma Institute have made it a truly pleasant journey. I would like to thank Dr John Pasley, Professor Nigel Woolsey and Dr Raoul Trines for access to HYADES and PrismSPECT simulation codes. I am grateful for the useful discussions with members of the laser plasma group namely L Wilson, A Rossall, R Al-Raddadi, O Culfa, R Crowston, V Aslanyan, D Blackman, E Tubman and P Durey. I would also like to thank fellow Fusion CDT members for their encouragement and support.

I have thoroughly enjoyed working with the team at Lawrence Livermore National Laboratory, USA and I thank all the staff from the Jupiter Laser Facility for making the experiment a success. I also thank Olivier Guilbaud and his team for their hard work during the experiment at the LASERIX facility, France.

Finally, I also thank my big loving family namely Abu-jee, Ami-jaan, Chunggaze, Sammy, Saffy, Saghir, Sehreen, Ayishah, Eliza, Alisha, Rayyan, Mehreen and Hunayn for their continuous support over the years.

Declaration

I, Mohammed Shahzad, declare that this thesis titled, 'Investigating energy transport in high density plasmas using buried layer targets' and the work presented in it are my own. I confirm that:

- This work was done wholly or mainly while in candidature for a research degree at this University.
- Where any part of this thesis has previously been submitted for a degree or any other qualification at this University or any other institution, this has been clearly stated.
- Where I have consulted the published work of others, this is always clearly attributed.
- Where I have quoted from the work of others, the source is always given. With the exception of such quotations, this thesis is entirely my own work.
- I have acknowledged all main sources of help.
- Where the thesis is based on work done by myself jointly with others, I have made clear exactly what was done by others and what I have contributed myself.

Dedicated to my family.

Chapter 1

Introduction

This thesis will investigate energy transport mechanisms in high density laser produced plasmas using buried layer targets[1]

The study of energy transport is important to both astrophysical (e.g stellar evolution, star and planetary formation) [1] and laboratory laser produced plasmas (e.g inertial confinement fusion (ICF), x-ray sources, particle accelerators). Energy transport processes can also influence laser-plasma interactions such as hydrodynamic instabilities, x-ray production and laser ablation. Energy transport can be a highly complex non-linear issue, due to the large temperature and density gradients produced between the critical density and the ablation surface in laser plasmas and the multiple heating process which occur simultaneously.

This thesis will demonstrate how the interplay between competing energy transport mechanisms can be diagnosed by using buried layer targets. As the laser propagates upto the critical density, the buried layer is heated by energy transport mechanisms that subsequently ensue between the critical density and the

[1] A buried layer target contains a solid thin diagnostic layer and is tamped either side with typically plastic layers. A laser irradiates the plastic and heat is transported to the buried layer material typically before significant expansion can occur.

ablation surface. By probing with an EUV laser and recording the emission which emanates from the buried layer, energy transport mechanisms can be diagnosed.

1.1 Inertial Confinement Fusion.

To understand the broader context of this thesis it is important to understand the role of energy transport in high density plasmas such as those produced in inertial confinement fusion.

Nuclear fusion occurs in the Sun when nuclei gain sufficient energy to overcome electrostatic repulsion and fuse together under the strong force releasing energy. However, without the immense gravitational forces found in the Sun, replicating the nuclear fusion process here on Earth requires the formation of stable plasmas with conditions[2] that are difficult to achieve.

Inertial confinement fusion (ICF) seeks to demonstrate the fusion of deuterium and tritium atoms[3] in the short time required for a high density plasma to disassemble. Energy released could be converted to heat to power a turbine and hence generate electricity. J. Nuckolls in 1972 predicted lasers could compress material sufficiently for nuclear fusion [2]. Since then numerous scientific and technological advancements have led to the culmination of the National Ignition Facility (NIF)[4]. The NIF uses 192 neodymium-doped phosphate glass laser beams of energy 1.8 MJ to investigate laser fusion. NIF has also performed experiments investigating high energy density plasmas (HEDP) and x-ray effects as well as fundamental science [3].

[2]Fusion plasmas require high temperatures so nuclei gain enough energy to overcome Coulomb repulsion.

[3]Deuterium and tritium are isotopes of Hydrogen. The deuterium nucleus contains a neutron and a proton, whereas tritium nucleus has 2 neutrons and 1 proton.

[4]The national ignition facility evolved from a range of predecessors including Janus, Shiva and Nova.

The impact of a high powered laser on an ICF capsule causes the outer layer to ablate. By Newton's third law, the outer layer rapidly expands and forces the inner material to implode under the ablation pressure. At peak compression[5] the mass inertia holds the plasma together for a time interval $\simeq 100$ ps producing high temperature and density conditions that ignite a small fraction of the fuel (hot spot). A burn wave subsequently ignites the 'colder' DT fuel as alpha particles are reabsorbed. For optimum re-absorption of alpha particles, the central hot spot should have a confinement parameter of $\rho R \sim 0.3$ gcm^{-2} at temperature, $T \simeq 10$ keV. The neutrons produced from the fusion reactions typically have a larger mean free path and therefore escape the inner burning plasma [3].

There are numerous avenues to ICF but schemes referred to as direct and indirect drive are the dominant paths which are currently being investigated[6]. Direct drive occurs when lasers impinge directly onto the ICF capsule producing a coronal plasma and ablating a shell containing deuterium and tritium [4]. The advantage of direct drive is that a larger gain output is predicted while using lower powered incident lasers [5]. However, non-uniformities in the laser beam (imprint) can seed large hydrodynamic instabilities and distort implosion symmetry, therefore reducing the output gain. To deliver the laser energy more uniformly onto the capsule, indirect drive was developed [2]. The NIF follows the indirect drive approach where lasers indirectly ablate the shell of a DT capsule by striking the hohlraum[7] wall, which re-radiates x-rays onto the DT capsule ablating the surface more symmetrically compared to direct drive.

To ensure ICF is an economically viable alternative energy source substantial improvements are required to increase the efficiency of both the laser system and the physical processes. Currently only $\sim 5 - 15\%$ of the laser energy reaches the

[5]The target is compressed to a 1000 times solid density
[6]Fast ignition, shock ignition and Z-pinch are other alternatives.
[7]A hohlraum is an space or cavity with high radiation energy density

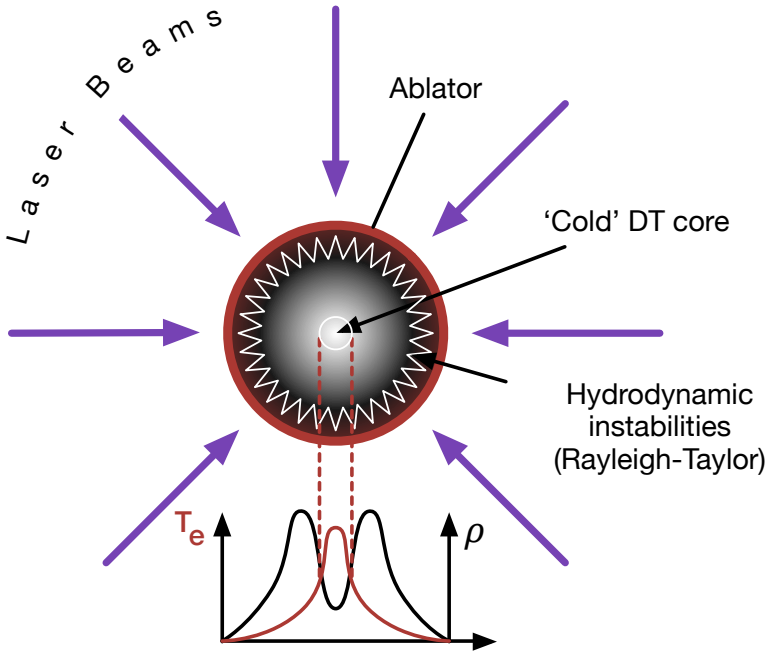

(a)

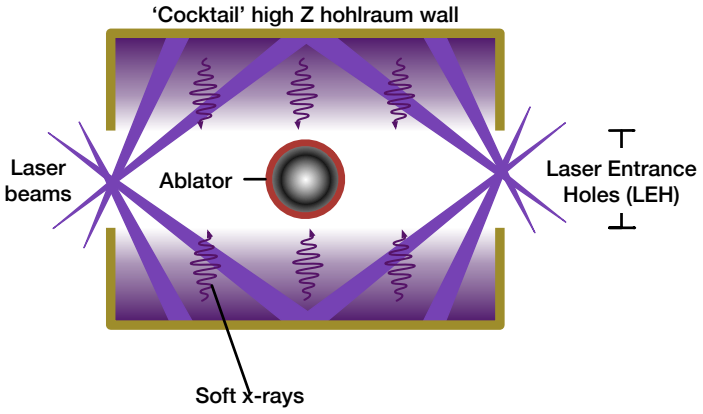

(b)

FIGURE 1.1: (a) Direct drive - lasers spherically illuminate a DT capsule from all angles compressing the target to high temperature and densities. Laser imprint can seed large hydrodynamic instabilities leading to asymmetric implosion, which reduces the energy output. (b) Indirect drive - lasers strike the inside of a hohlraum capsule producing a sea of x-rays which heat the inner DT pellet more uniformly compared to direct drive. However, larger powered lasers are required to reach ignition conditions due to energy losses.

capsule due to losses from scattered light, generation of low density plasmas, x-rays escaping from the laser entrance hole (LEH) and heating of the hohlraum wall [3]. Producing the plasma conditions required for ignition is hindered by processes such as hot electron preheat and hydrodynamic instabilities, which are influenced by aspects of energy transport.

1.2 Energy transport in laser produced plasmas.

A plasma can be categorised into two regions depending on whether the electron density is less (underdense) than or above (overdense) the critical density. Laser energy is absorbed in the underdense plasma upto the critical density by collisional absorption processes. A mixture of transport processes transfer the energy away from the critical density into the 'cold' overdense solid material. The energy is transported by mainly electrons and photons, rather than the heavier 'immobile' ions. An introduction to energy transport mechanisms in laser produced plasmas will be discussed in greater detail in chapter 2.

1.2.1 Energy Transport in Inertial Confinement Fusion (ICF) plasmas

Different energy transport mechanisms are responsible for imploding ICF capsules, for example, electron conduction is required in direct drive, whereas indirect drive relies upon x-ray radiation transport. A physical understanding of energy transport is required to optimise the hohlraum capsule design. The energy transport mechanisms resulting in x-ray ablative drive, x-ray production and radiative energy loss in hohlraum targets emphasise the importance of understanding energy transport schemes in inertial confinement fusion.

Hohlraum x-ray emission

The purpose of a hohlraum capsule is to absorb the laser energy and re-emit x-ray radiation more uniformly onto the inner DT pellet, therefore reducing the growth of hydrodynamic instabilities compared to direct drive. At the NIF, lasers rapidly ionise the inside of the gold hohlraum wall, producing a highly opaque plasma. The laser energy is absorbed predominantly by inverse bremsstrahlung in the large coronal plasma produced by the $\sim$ ns laser drive pulses. Within this highly opaque plasma x-rays are re-absorbed and re-emitted producing a relatively uniform Planckian radiation field at a particular hohlraum temperature.

A mixture of high Z materials including uranium and gold have led to the development of 'cocktail' hohlraums [6] where the elements are carefully chosen to ensure that a dip in opacity of one material overlaps with a higher opacity from another, therefore producing a higher mean opacity. This increases the albedo[8] of the hohlraum wall.

Hohlraum wall losses

The radiative flux balance on the hohlraum wall is given by,

$$S_t = S_l + S_x = S_R + S_h \tag{1.1}$$

where S_t is the total incident flux, S_l is the absorbed laser fluence, S_x is the flux of x-rays falling from adjacent walls, S_R is the re-emitted x-rays from the wall and S_h is the radiative flux lost to the hohlraum wall (see figure 1.2). Radiation transport drives a diffusive thermal wave into the hohlraum wall. The use of a high Z material such as uranium increases the mean opacity of the hohlraum,

[8]The fraction of x-ray power incident on the walls that is re-emitted is called the wall albedo.

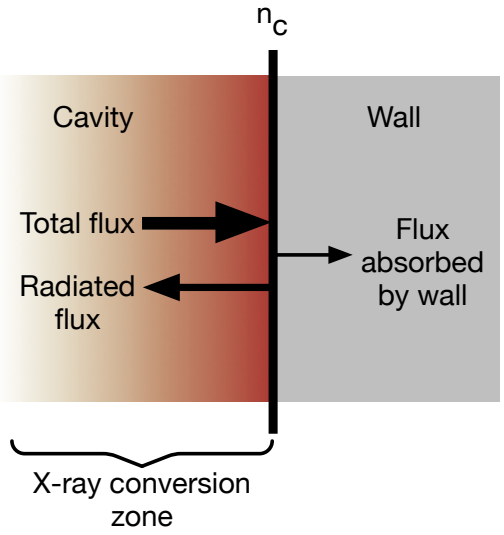

FIGURE 1.2: A diagram showing the energy flux balance of a hohlraum. The laser energy is absorbed upto the critical density by inverse bremsstrahlung. Energy is transported away from the x-ray conversion zone by electron conduction and radiative transport therefore reducing the hohlraum temperature. Cocktail hohlraums reduce radiative energy loss to the wall because the plasma produced has a higher mean opacity.

therefore inhibiting the flow of radiation into the 'cold' overdense plasma wall [7]. It is important to understand opacity and the flow of radiation to limit the energy loss through the wall.

X-ray ablative drive

X-ray ablation occurs when the x-ray radiation emitted from the hohlraum deposits its energy onto the surface of the capsule. The x-rays produce shock waves which compress and heat the target. Radiative drive depends on the opacity of the ablator material. The ablator materials are chosen so that the opacity is high at lower temperatures to ensure efficient absorption of the incident energy. However, at higher temperatures the opacity is lower so that radiation can propagate to the ablation front. To improve the efficiency of x-ray ablative drive, capsules made from low Z materials which have a lower opacity are preferred, so that radiation can propagate to greater depths into the target. Designs incorporated

plastic shells and also beryllium which has increased thermal conductivity, tensile strength, density and lower opacity [8].

Ablator shells are often doped with high Z materials to counteract fuel preheating by M- and O- band x-ray radiation generated in beam interaction spots on the hohlraum wall. Radiation transport will be discussed in further detail in chapter 2.

Hot electron pre-heat

Laser-plasma interactions such as resonance absorption and parametric instabilities can produce a surplus of high energy (keV - MeV) hot electrons (see section 2.3). These hot electrons have a high penetration depth and therefore can pre-heat the cold DT fuel. Hot electron pre-heat increases the entropy of the DT fuel before the compression wave arrives, thus preventing the capsule from imploding efficiently. The production of hot electrons is dependent on a wide range of factors including laser polarisation, intensity and incident angle. Chapter 2 further details the theory behind hot electron transport in high density laser produced plasmas. Chapters 5 and 6 investigate the laser energy-hot electron conversion efficiency and the efficiency of resonance absorption using an extreme ultraviolet (EUV) laser.

1.2.2 Energy transport in buried layer targets

A buried layer target comprises a thin layer of material which is tamped by e.g. plastic substrate layers on either side to retard plasma expansion after laser irradiation, therefore producing relatively uniform high density plasmas (see figure 2.1) [9]. As the laser impinges onto the plastic layer it rapidly ionises and ablates. The energy is then transported from the critical density to the buried layer typically

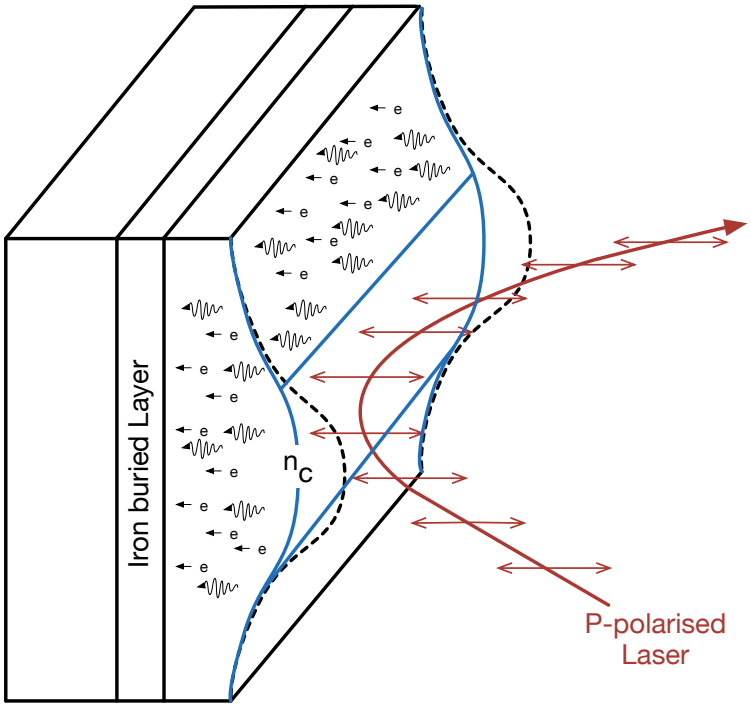

FIGURE 1.3: A diagram of a buried layer target with an incident p polarised laser showing the energy transport (hot electrons, thermal conduction and radiative transport) from below critical density, n_c to the buried layer.

by a combination of thermal conduction, hot electrons and radiation transport. Buried layer targets have paved the way to numerous discoveries related to energy transport in high density plasmas. For example, by varying the plastic target overlay thickness, the electron preheating of the buried layer was estimated [10, 11].

The irradiation of buried layer targets with short pulsed lasers offer the possibility of producing high density and temperature plasmas with limited temporal and spatial gradients. Ultrafast heating of buried layer targets using short pulsed lasers have demonstrated the ability to produce highly uniform plasmas for a short duration of time, before the onset of hydrodynamic expansion [12]. Due to the high densities and temperatures conditions produced by ultrashort laser pulses, it is possible that the buried layer can reach close to local thermodynamic equilibrium conditions. Using Kirchoff's law the opacity can be deduced from the emissivity of the plasma at LTE conditions [13]. Previous investigations have used short pulse lasers to measure opacity at extreme plasma conditions using buried layer

targets [14, 15]. To accurately determine the opacity of the buried layer the plasma conditions must be accurately diagnosed [16]. Previous experiments at AWE have used low-Z aluminium buried layer targets and K-shell spectroscopy to infer plasma conditions [17]. In collaboration with AWE and Lawrence Livermore National Laboratory, chapter 5 extends this concept by investigating the heating of mid-Z buried iron layer targets and L-shell spectroscopy to deduce plasma conditions [18].

1.3 Summary

Energy transport is important in laser produced plasmas and relevant to inertial confinement fusion where dominant energy transport mechanisms like radiation transport, hot electron heating and thermal electron conduction can affect ablative drive, hohlraum temperatures, hydrodynamic instabilities and hot electron pre-heating of the inner capsule fuel. Due to the volatile nature of heating a solid target to a plasma, a wealth of laser-plasma interactions ensue, resulting in a rapidly evolving plasma with numerous energy transport mechanisms. As the buried layer is heated by energy transport mechanisms, diagnosing the conditions of the buried layer can provide an insight into the energy transport (heating) processes. This thesis investigates energy transport mechanisms using buried iron layer targets, a high resolution grating spectrometer and an extreme ultraviolet (EUV) laser as diagnostics.

1.4 Work undertaken by author

This thesis presents measurements of energy transport in buried layer targets that are irradiated by high powered lasers. Chapters 2 and 3 introduce the core concepts

related to laser-plasma interactions, energy transport processes and spectroscopy. Chapter 4 details the instrumentation and diagnostics used to support this work.

Chapter 5 develops the understanding of energy transport in high density plasmas using L-shell emission spectra observed from the irradiation of buried iron layer targets using a high resolution grating spectrometer. The author worked with the COMET laser team at the Lawrence Livermore National Laboratory and recorded L-shell iron emission spectra using a high resolution grating spectrometer. The HYADES [19] code was operated by the author to simulate laser irradiated buried iron layer conditions. Post-processing the HYADES simulated data into the Prism-SPECT [20] collisional-radiative code the author simulated L-shell iron emission spectra (see chapter 5). A novel technique was developed by the author to determine the electron temperature and density using line ratios of adjacent ionisation states and the Saha equation. In chapter 5 the author has demonstrated that iron L-shell emission can be used to deduce the laser energy to hot electron conversion efficiency and the thermal electron conduction flux limiter.

The probing of plasmas using an extreme ultraviolet (EUV) laser in order to diagnose the interplay between certain energy transport schemes is discussed in chapter 6. The author was involved with an experiment at the LASERIX facility, which recorded the EUV transmission through buried iron layer targets that were irradiated by short pulse lasers. The author simulated the EUV laser transmission through the target using a post processor produced by L. Hobbs. The author modified the post-processor to include HYADES simulated buried iron layer target conditions and opacity data from PROPACEOS and IMP codes. The EHYBRID code was operated by the author to model the LASERIX EUV laser. The radiation absorption within the buried iron layer were calculated using TOPS, PROPACEOS, HYADES and IMP opacity codes by the author. The IMP opacity

was simulated by S. Rose, however the author modified the IMP opacity look-up table to simulate the drop in transmission 20 ps after laser irradiation.

Chapter 2

Background Theory of laser interactions

Some of the physics underlying key aspects of laser-plasma interactions and energy transport is discussed in this chapter. The chapter begins with an introduction to high powered lasers. The physics of laser-plasma interactions is briefly described in section 2.2. Laser absorption processes such as inverse bremsstrahlung and resonance absorption are introduced in section 2.3. As this thesis focusses on how energy is transported into buried layered targets, section 2.4 explains the theory behind the dominant energy transport processes of thermal conduction, hot electron transport and radiation transport. Chapters 5 and 6 further develop an investigation of energy transport and the interplay between competing heating processes using spectroscopy and extreme ultra-violet laser diagnostics.

2.1 High power pulsed lasers

Materials such as crystal, glass and ceramics can be used as the lasing medium for solid state lasers. The lasers used in chapters 5 and 6 used crystals (Nd:YAG and

Ti:sapphire respectively) as their laser oscillator gain medium. Crystal solid state lasers have thermal conductivities (~ 0.14 W/cmK) an order of magnitude larger than glass (~ 0.01 W/cmK), hence they can sustain higher pumping powers and faster repetition rates [22]. A brief description of the laser technology used for the experiments of this thesis is given in the following sub-sections.

2.1.1 Chirped pulse amplification

Laser amplifier chains have been used to increase the power of laser pulses emanating from laser oscillators up to Petawatt levels [23] by using chirped pulse amplification (CPA). The overall concept of CPA was first envisaged in the 1960s to increase the power available in radar [24]. A laser pulse is stretched, typically by a pair of gratings to allow low frequency components to travel a shorter path length compared to higher frequencies, resulting in a positively chirped pulse. The stretched pulse can be amplified with power-remaining below the damage threshold of the laser medium. After amplification, the pulse then passes through a compressor consisting again of two large gratings resulting in a short duration high power laser pulse. The LASERIX [25] and COMET [26] laser facilities both employed the CPA technique to produce focussed laser pulses $\sim 10^{16} - 10^{18}$ Wcm^{-2}.

2.1.2 Nd:YAG laser

Nd:YAG ($Y_3Al_5O_{12}$) crystals are widely used in laser technologies [27, 28]. The strongest Nd:YAG lasing line transition ($^4F_{3/2}$–$^4I_{11/2}$) produces photons with a wavelength of 1064 nm. Nd:YAG lasers can either run continuously or in a pulsed mode with mode-locked pulses of picosecond duration [22]. The COMET laser used in chapter 5 employed a 4-stage Nd:phosphate glass amplifier to increase the 1064 nm, 2 ps laser pulses to an output energy of ~ 10 J [29]. A 4 stage Nd:phosphate

amplifier which comprised 7 mm, 16 mm, 25 mm and 50 mm diameter amplifying rods [26] was employed. Each amplifier has a successively larger diameter to ensure the irradiance of the amplified beam remains below the damage threshold of the glass. After a final double pass through the 50 mm diameter rod amplifier, the laser beam diameter has increased to 8.5 cm [26].

At low laser intensities the polarisation in a material is typically linearly proportional to the electric field of the laser. However, at high laser intensities the polarisation can behave non-linearly with the laser electric field. In chapter 5 a KDP crystal was used to produce frequency doubled (532 nm) light. The conversion efficiency from to second harmonic light was $\sim 50\%$. Due to the non-linear nature of frequency doubling, the contrast of the laser pulse increases to 10^8 [17]. The COMET laser was focussed using a $f/3.72$ off-axis parabola mirror to produce irradiances of $\sim 10^{17}$ Wcm^{-2}.

2.1.3 Ti:Sapphire laser

The four-level Ti:sapphire (Ti:Al_2O_3) laser produces laser pulses with a large bandwidth of lasing frequencies of wavelengths ranging between $660 - 1180$ nm. Ti:sapphire crystals are commonly used as mode-locked lasers and can produce ultra-short laser pulses ($\sim$ fs). The LASERIX laser which was used in chapter 6 operated at a wavelength centred at 800 nm with a pulse duration (τ_p) of ~ 35 fs. The pulse energy of 21 mJ was focussed using a $f/8$ mirror to produce irradiances on target of $\sim 10^{16}$ Wcm^{-2}.

2.2 Laser plasma physics

When a focussed high intensity laser (intensity $> 10^9$ Wcm^{-2}) strikes a solid target, a plasma is produced with the initial free electron created by multi-photon processes [30]. The initial free electrons enable further ionisation as the incoming laser pulse heats them directly. As the peak irradiance for the experiments reported in this thesis are $10^{16} - 10^{18}$ Wcm^{-2}, it is important to be aware of plasma produced by any pre-pulse irradiation ($> 10^9$ Wcm^{-2}) created before the main pulse. For long pulsed laser irradiation ($>$ ns) of solid targets it is possible for the initial plasma to expand during the laser pulse. However, for shorter laser pulse durations $<$ ps the heating occurs mainly before the onset of thermodynamic expansion.

Heated initially stationary plasma expands as a rarefaction wave at the ion acoustic sound speed, c_s which is given by,

$$c_s = \sqrt{\frac{Z^* k_B T_e}{m_i}} \tag{2.1}$$

where Z^* is the average ionisation, k_B is the Boltzmann constant, T_e is the electron temperature and m_i is the mass of ion. The electron density profile in the x-direction for a self-similar isothermal expansion can be written [31],

$$n_e(x) = n_e(0) exp\left(-\frac{x}{c_s t}\right) \tag{2.2}$$

where n_0 is the electron density at the solid surface ($x = 0$). Equation 2.2 shows that a wide range of densities evolving rapidly in time t are produced when an initially solid density plasma freely expands.

Employing buried layer targets, where a thin layer of material in a target is studied can significantly reduce the density range of the material. Overlay material at the

front of the target (towards the laser) tamps the buried layer forward expansion. This is shown in figure 2.1 where the HYADES code has simulated plasma conditions (ρ and T_e) for a buried iron target and a bare iron target. The plasma conditions within the buried iron layer are much more uniform compared to the bare iron target.

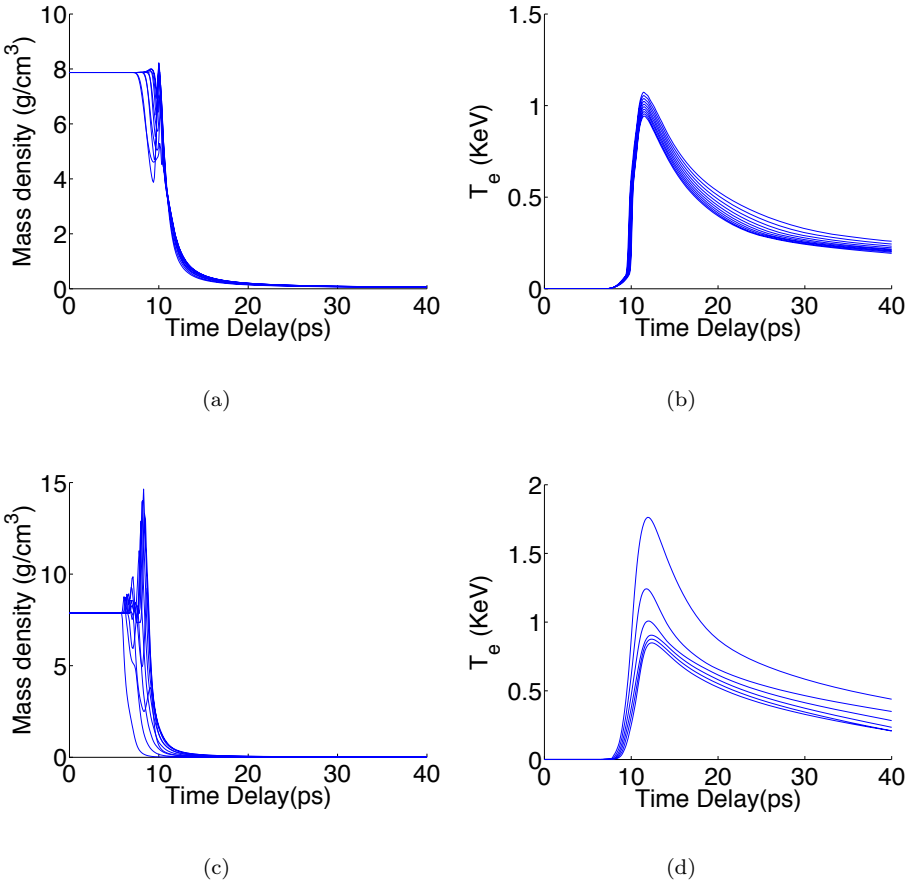

FIGURE 2.1: The HYADES 1D code was used to simulate the mass density and electron temperature for bare foil and buried iron layer targets. Each zone through the buried iron layer is represented as a blue curve. Figures (a) and (b) show the ρ and T_e conditions within the buried iron (50 nm) layer target. Figures (c) and (d) show the ρ and T_e conditions within the bare iron foil (50 nm) target. The laser irradiance in the HYADES code was set to 3×10^{17} Wcm^{-2} in a 35 fs pulse and a flux limiter of 0.06 was used.

The intensity of a laser pulse, I is related to the maximum electric field, E_0 by,

$$I = \frac{1}{2}\epsilon_0 c\langle E^2\rangle \tag{2.3}$$

where ϵ_0 is the vacuum permittivity and c is the speed of light in a vacuum. For high intensity lasers such as those used in chapters 5 and 6 with intensities $\sim 10^{16} - 10^{18}$ Wcm^{-2} the electric field (E_0) ranges between $\sim$ 8 GVm^{-1} - 8 TVm^{-1}. Such strong electric fields oscillate electrons in a quiver motion whilst the ions remain relatively stationary due to their larger mass. Low laser intensity pulses can also drive electrons in a quiver motion.

A dispersion relation describes the relationship between the radiation frequency and the wave vector, k. For a plane wave solution of the electromagnetic wave equation, the dispersion relation is given by [31],

$$\omega_L^2 = \omega_{pe}^2 + k^2 c^2 \tag{2.4}$$

where ω_L is the laser frequency and ω_{pe} is the plasma frequency. As the laser frequency approaches the plasma frequency, the plasma becomes opaque to the incident laser light as $\omega_L < \omega_{pe}$. The laser energy propagates upto the critical density, n_c of the target where the laser energy is predominantly absorbed and reflected. The critical density (m^{-3}) is given by,

$$n_c \simeq \frac{1.1 \times 10^{15}}{\lambda^2} \tag{2.5}$$

where λ is the wavelength of the laser in metres.

As the critical density is inversely proportional to the wavelength squared (equation 2.5) a shorter wavelength laser propagates to a greater electron density. The LASERIX extreme ultraviolet (EUV) laser operating at 13.9 nm utilised this penetration and was used to probe high density laser produced plasmas in chapter 4.

Figure 2.2 shows the temperature and density profile of a target irradiated by a

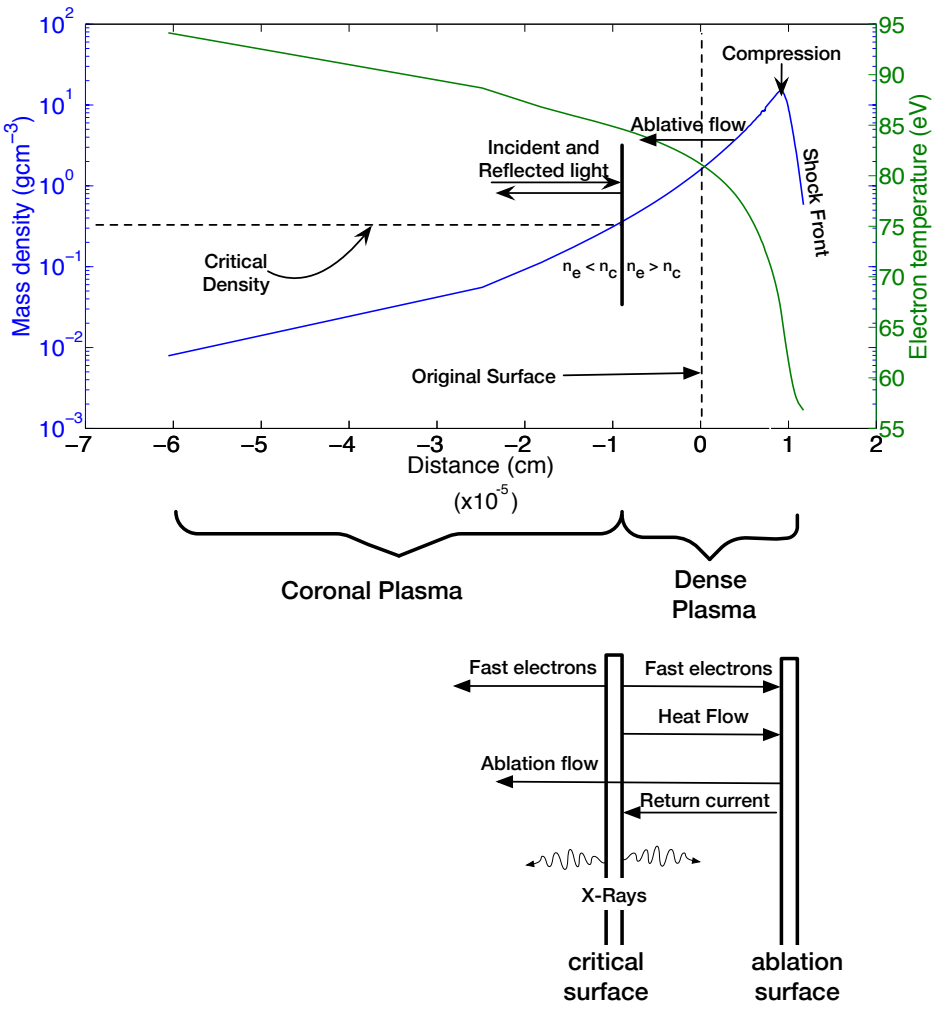

FIGURE 2.2: A HYADES 1D simulation showing the mass density and electron temperature profile as a function of distance when a frequency doubled ($\simeq 0.5\mu$m) laser irradiates (3×10^{16} Wcm^{-2}) a solid iron target, producing a high density plasma. The various energy transport and plasma processes that occur in the coronal plasma and dense plasma regions of the target are shown. The critical density, ablative flow, original surface, peak compression and shock front are also displayed.

laser as a function of distance (normal with respect to the target). The plasma density locally steepens at the critical density because photons reflect and exert twice the light pressure onto the plasma as well as depositing energy locally [31] (see figure 2.2).

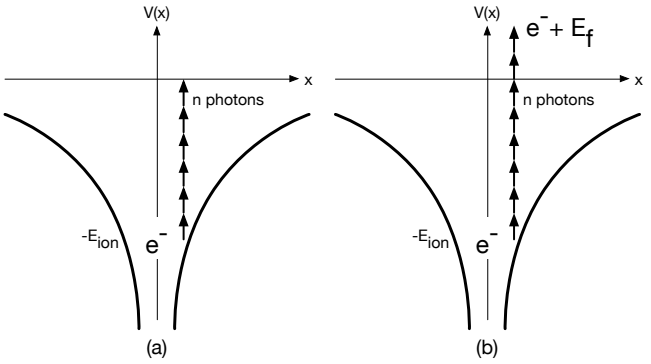

FIGURE 2.3: An electron is bound by a potential well V(x) with a ground state energy, $-E_{ion}$. (a) The electron is ejected from its bound state into the continuum level due to the absorption of multiple n photons - multi-photon ionisation. (b) If the number of photons absorbed exceeds the ionisation threshold the electron gains kinetic energy, E_f.

2.3 Laser absorption

2.3.1 Multi-photon absorption

A photon incident on a solid target with sufficient energy to overcome the ionisation potential can liberate an electron by the photoelectric effect. However, for lasers the photon energy is usually less than the ionisation energy, and ionisation can only occur by multi-photon and optical field ionisation. For a high power laser this occurs within the first few cycles of the laser electric field and creates the first free electrons with which the remainder of the pulse interacts.

Multi-photon ionisation (MPI) occurs when several low frequency photons collectively exceed the ionisation energy and propel the electron into the free continuum level (see figure 2.3). Electrons which absorb more photons than the ionisation threshold gain kinetic energy, E_f,

$$E_f = n\hbar\omega - E_{ion} \tag{2.6}$$

where n is the number of photons absorbed. The presence of an intense electric

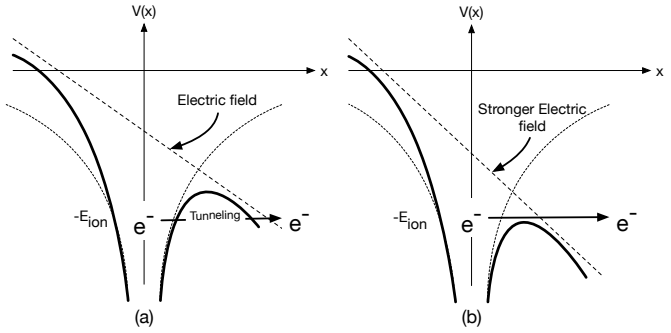

FIGURE 2.4: (a) The suppression of potential well V(x) by a strong electric field increases the probability that a wave function can tunnel through the barrier and ionise - tunneling ionisation. (b) Extremely intense electric fields can suppress the barrier allowing electrons to ionise rapidly over the barrier.

field from a high intensity laser pulse can suppress the atomic potential and reduce the energy required to ionise an electron (see figure 2.4). As a result an electron can quantum mechanically tunnel through the potential barrier and ionise; a process known as tunnelling ionisation. For laser intensities above 10^{16} Wcm^{-2} the electric field (corresponding to $\sim$ 8 GVm^{-1}) can remove the potential barrier to the electron entirely, therefore ionising the electron spontaneously by 'over the barrier' ionisation.

For linearly polarised light the ionisation is localised at the peaks and troughs of the electric field where the electric field magnitude is at its maximum. Keldysh theory [32] shows that multi-photon and tunnel ionisation are two regimes of non-linear ionisation. Keldysh investigated the laser intensity dependence on ionisation potential and calculated the transition between multi-photon and tunnel ionisation regimes which is given by the Keldysh parameter,

$$\gamma \sim \sqrt{\frac{E_{ion}}{\phi_{pond}}} \tag{2.7}$$

where the energy gained by an electron from the oscillating electric field is given by the ponderomotive potential, ϕ_{pond}. For $\gamma < 1$ barrier suppression ionisation is dominant and when $\gamma > 1$ multi-photon ionisation occurs.

2.3.2 Inverse bremsstrahlung

Bremsstrahlung emission occurs when a free electron decelerates due to the influence of a neighbouring ion, resulting in the emission of a photon with an energy equal to the kinetic energy lost by the free electron. When a free electron in the field of an ion accelerates by absorbing a photon of incident radiation, this is known as inverse bremsstrahlung. Subsequent collisions distributes the laser energy within the plasma to other free electrons.

The rate of collisional absorption is dependent on the electron-ion collision frequency in a plasma, which is given by [34],

$$\nu_{ei} = \frac{4(2\pi)^{1/2}}{3} \frac{n_e Z_f e^4}{m^2 v_{te}^3} \ln \Lambda \tag{2.8}$$

where Z_f is the number of free electrons per atom, n_e is the electron density, T_e is the electron temperature, lnΛ is the Coulomb logarithm (ln$\Lambda = b_{max}/b_{min}$). The absorption coefficient, κ due to inverse bremsstrahlung is given by [33],

$$\kappa = \sqrt{2\pi} \frac{16\pi}{3} \frac{(Z^*)^2 n_e n_i e^6 \ln(\Lambda_{ei})}{c(m_e k T_e)^{3/2} \omega_0^2 \sqrt{\epsilon}} \tag{2.9}$$

where the average ionisation (Z^*), laser angular frequency (ω_0), dielectric permittivity ($\epsilon = 1 - \frac{\omega_{pe}^2}{\omega_0^2}$) are incorporated into the equation. Compared to other processes, the total collisional absorption, A_L taking into account the absorption of laser light up to the critical density and its subsequent reflection can be calculated using,

$$A_L = exp\left(-2 \int_{-\infty}^{0} \kappa(x) dx\right). \tag{2.10}$$

The collisional nature of inverse bremsstrahlung ensures that there is an inherent laser intensity dependence. The collisional absorption process is dominant at low laser intensities $I < 10^{14}$ Wcm^{-2}. At higher laser intensities $> 10^{15}$

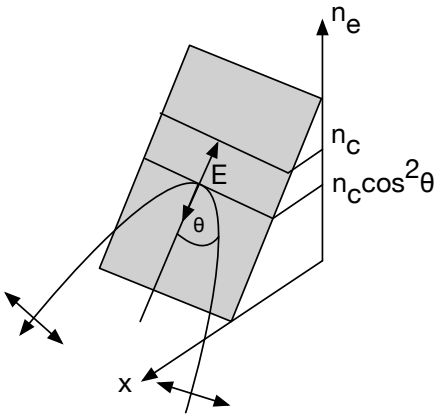

FIGURE 2.5: This figure shows a p-polarised ray incident upon a target. The laser turning point occurs at $n_c\cos^2\theta$. The p-polarised light resonantly excites electron plasma waves across the critical density leading to resonance absorption.

Wcm^{-2}, larger plasma temperatures reduce the electron-ion collision frequency [34], therefore the heating due to collisional absorption decreases. In chapter 5 inverse bremsstrahlung absorption is mainly responsible for heating a front plastic tamper layer. Energy transport mechanisms subsequently heat a buried iron layer in the target.

2.3.3 Resonance absorption

When p-polarised light is incident upon a target at oblique angles, resonance absorption occurs. For an angle (θ) the laser pulse penetrates up to a turning point electron density, $n_c\cos^2\theta$, where n_c is the critical density. The laser energy subsequently tunnels to the critical density where the electric field swells to a high value due to the refractive index approaching zero (see figure 2.5). The driving laser frequency causes electron plasmas waves to resonate at the critical density so that electrons are accelerated to KeV - MeV energies [35]. The resonant waves are damped by collisions at low intensities $< 10^{15}$ Wcm^{-2} or by particle trapping and wave breaking at high intensities $> 10^{15}$ Wcm^{-2}. The hot electrons produced penetrate and heat the over-dense plasma region.

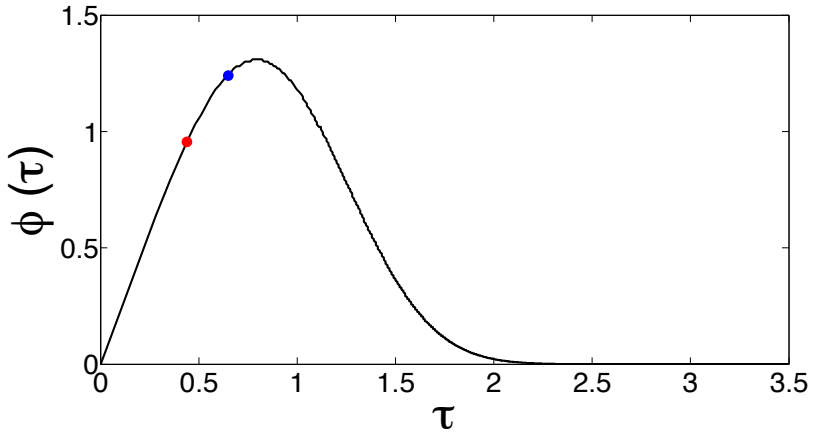

FIGURE 2.6: This figure shows a measure of the resonance absorption efficiency as a function of τ, where $\tau = (\omega L/c)^{1/3} \sin\theta$. The red dot indicates the absorption efficiency for plasmas produced without a prepulse and the blue dot indicates those which are produced with a prepulse for the conditions of chapter 6 with scale length L calculated using HYADES simulations.

A measure of the resonance absorption efficiency, $\phi(\tau)$ is given by,

$$\phi(\tau) \simeq 2.3\tau exp\left(\frac{-2\tau^3}{3}\right) \tag{2.11}$$

where $\tau = (\omega L/c)^{1/3} \sin\theta$ [31]. The absorption, f_A is given as $f_A \propto \frac{\phi(\tau)^2}{2}$. The resonance absorption efficiency is dependent on the incident angle, θ, laser frequency ω and the plasma density scale length, L. The optimum resonance absorption efficiency is approximately at $\tau \sim 0.8$. As $\tau \to 0$ the efficiency decreases because of the sinθ dependence. However, at large τ the efficiency decreases because the incident wave has to tunnel through a larger scale length plasma, L. The efficiency of resonance absorption was calculated in chapter 6 for plasmas with long $\simeq 1\mu$m and short $\simeq 0.2\mu$m scale length. A deliberte prepulse produces an expanding coronal plasma with the longer scale length. Figure 2.6 shows that the resonance absorption efficiency is comparable for plasmas which are produced with a prepulse compared to those which are irradiated without a prepulse under the conditions of the experiment described in chapter 6.

In chapter 6 a diode array was used to record the hot electron bremsstrahlung

emission spectra. Filters of varying thickness were placed over four seperate diodes to determine the bremsstrahlung emission spectra at specific spectral frequencies chosen such that the gradient of the bremsstrahlung emission can be deduced.

At moderate laser intensities ($10^{14} - 10^{18}$) the plasma temperature scales as $\propto I^{4/9}$ [36]. Laser intensities above $> 10^{15}$ Wcm^{-2} ionise plasmas to high electron temperature which subsequently behave as collisionless plasmas. This is because the collisional absorption coefficient reduces at higher electron temperatures due to the $\propto \frac{1}{T_e^{3/2}}$ dependence. Collisionless absorption processes such as resonance absorption dominate at higher laser intensities.

2.3.4 Other absorption mechanisms

High laser intensities $\sim 10^{18}$ Wcm^{-2} can produce steep density profiles which lead to collisionless absorption schemes such as Brunel absorption, anomalous skin effect and $\mathbf{j} \times \mathbf{B}$ acceleration. The laser electric field penetrates to a skin depth, $l_s = c/\omega_{pe}$. Electrons within the skin depth of the laser are highly influenced by the large electric fields and therefore oscillate with a relativistic quiver velocities.

The Brunel effect [37] also known as vacuum heating describes the absorption of laser energy at intensities above 10^{18} Wcm^{-2} where the plasma density gradient become very steep. At the plasma-vacuum interface the intense laser electric field accelerates electrons into the vacuum beyond the Debye length, λ_D. The reversal of the laser electric field accelerates the electrons back towards the solid target surface. The electric field penetration is limited to the skin depth $\sim c/\omega_p$, however the energised electrons propagate in the polarised electric field direction.

Under the normal skin effect electrons oscillate within the skin depth, l_s and distribute the laser energy through collisions with ions (inverse bremsstrahlung). However, the anomalous skin effect describes the absorption of the laser energy by

electrons which have a mean free path larger than the skin depth, $\lambda_e > l_s$. As a result the laser energy is distributed non-locally within an enlarged skin depth, l_a which is given by Weibal et al [38],

$$l_a \simeq \left(\frac{c^2 v_{te}}{\omega \omega_p^2}\right)^{(1/3)} \tag{2.12}$$

With $\mathbf{j} \times \mathbf{B}$ acceleration electrons are driven by the $\mathbf{v} \times \mathbf{B}$ Lorentz force in the direction of the laser beam. The $\mathbf{j} \times \mathbf{B}$ acceleration occurs at twice the laser frequency and operates for all polarisations except circular and is most effective at normal incidences [34].

2.4 Energy transport

Laser produced plasmas are complex due to the rapid transformation from solid to plasma creating steep density and temperature gradients. The transport of absorbed laser energy is dependent on many factors as the plasma evolves in time. Processes including thermal conduction, radiation transport and hot electron transport can move energy from where it is absorbed into the target. Chapter 5 will focus on using plasma emission spectroscopy to deduce the energy transport processes that occur in buried iron layer targets. Chapter 6 diagnoses energy transport mechanisms using a probing extreme ultra-violet laser as a diagnostic.

This section introduces energy transport methods which transfer energy from the sub-critical electron density plasma to over dense plasmas ($n_e > n_c$). Figure 5.12 shows that an iron layer remains predominantly at solid density when irradiated by lasers at intensities $\sim 10^{17}$ Wcm^{-2}. The iron layer is heated by energy transport mechanisms rather than collisional absorption effects which are localised in the underdense region.

2.4.1 Electron thermal conduction

Diffusive conduction of heat through a material occurs at a rate given by,

$$Q = -K\nabla T \tag{2.13}$$

where the heat flow, Q is proportional to the negative thermal gradient of the temperature, ∇T and the heat conductivity is given by K which depends mainly on the composition of the structure and the temperature [39]. Equation 2.13 is limited to shallow thermal gradients because for very steep temperature gradients the heat flow can become infinite, therefore unphysical.

Spitzer-Harm conductivity

The diffusion of heat, Q_{SH} is given classically by the Spitzer-Harm (SH) transport equation [40],

$$Q_{SH} = -\frac{1}{3}\lambda_e \nu_e n_e k \nabla T_e = -K\nabla T_e \tag{2.14}$$

where λ_e is the mean free path of the electrons, ν_e is the electron velocity, k is the Boltzmann constant and ∇T_e is the thermal gradient. The Spitzer-Harm treatment of thermal conductivity assumes that the electron distribution function, f is close to Maxwellian with a Maxwellian distribution f_M everywhere except for a small perturbation f_1. Assuming that the electron mean free path, λ_e is less than the temperature scale length, $L_T = \frac{T}{dT/dx}$ and the distribution has a weak angular dependence, the electron distribution function, f is given by,

$$f(\mathbf{r}, \mathbf{v}, \theta, t) = f_M(\mathbf{r}, \mathbf{v}, t) + f_1(\mathbf{r}, \mathbf{v}, t)cos\theta \tag{2.15}$$

where $f_1 << f_M$. Further assumptions made for the Spitzer-Harm model include that the plasma evolves slowly in time such that,

$$\frac{\partial f_M}{\partial t} = 0, \tag{2.16}$$

$$\frac{\partial f_1}{\partial t} = 0. \tag{2.17}$$

The classical Spitzer-Harm conductivity, K is given by,

$$K = 2 \times 10^{-4} \frac{T_e^{5/2}}{Z \ln \Lambda} \tag{2.18}$$

where T_e is the electron temperature and $\ln\Lambda = \frac{b_{min}}{b_{max}}$ is the Coulomb logarithm[1].

The Spitzer-Harm model breaks down between the critical and ablation surfaces for laser produced plasmas as the assumption that the mean free path is less than the thermal scale length is no longer valid. The large thermal gradients produced by high intensity lasers lead to a non-local energy transport regime due to the production of high energy electrons which strongly deviate from the Maxwellian velocity distribution.

Thermal conduction can be modified by considering the free streaming limit, Q_f which estimates the maximum heat flow that a plasma can carry [41] (see section 2.4.1). It can be shown that [42],

$$Q_{SH} \propto \frac{\lambda_e}{L_T} Q_f \tag{2.19}$$

where λ_e is the mean free path and L_T is the scale length. The validity of the Spitzer-Harm model depends strongly on the ratio $\frac{\lambda_e}{L_T}$. When $\frac{\lambda_e}{L_T} < 10^{-2}$ the diffusion approximation is valid, however when $\frac{\lambda_e}{L_T} > 10^{-2}$ the energy transport is reduced significantly.

[1] b_{max} is often taken as the Debye length.

The reduction of the heat flow has been investigated extensively and can be due self generated magnetic fields [43, 44]. The flux limited approximation takes into account this heat flow reduction by using a flux limit multiplier.

Fokker-Planck treatment

Bell et al [45] solved the Fokker-Planck equation to describe the energy transport in high density laser produced plasmas. The Fokker-Planck equation is given as [42],

$$\frac{\partial f}{\partial t} + \mathbf{v} \cdot \frac{\partial f}{\partial \mathbf{r}} + \frac{e}{m_e}(\mathbf{E} + \mathbf{v} \times \mathbf{B}) \cdot \frac{\partial f}{\partial \mathbf{v}} = \left(\frac{\partial f}{\partial t}\right)_{collisions} \tag{2.20}$$

where the electron distribution function, $f(\mathbf{v}, \mathbf{r}, t)$ describes the particle probability distribution in space ($\mathbf{r}$), velocity ($\mathbf{v}$) and time (t). The evolution of the distribution function in time is represented by the first term, $\frac{\partial f}{\partial t}$. The second and third terms arise due to changes in space. The term $\mathbf{v} \cdot \frac{\partial f}{\partial \mathbf{r}}$ describes advection with the effect of the Lorentz force given by $\frac{e}{m_e}(\mathbf{E} + \mathbf{v} \times \mathbf{B}) \cdot \frac{\partial f}{\partial \mathbf{v}}$. The collisional term, $\left(\frac{\partial f}{\partial t}\right)_{collisions}$ allows changes in time due to electron-electron and electron-ion collisions and is usually dominated by the cumulative effect of small angle collisions [46]. When the right term is set to zero, the equation is known as the Vlasov equation. However, high density plasmas are very collisional systems, hence inter-particle collisions play a large role in the transfer of energy.

The collisional term in equation 2.20 describes to what extent the Maxwellian distribution is perturbed due to collisional effects, which alter the magnitude and direction of the velocities of the particles. Assuming small-angle collisions are dominant, the collisional term can be shown to be given by [31],

$$\left(\frac{\partial f}{\partial t}\right)_{collisions} = -\frac{\partial}{\partial \mathbf{v}} \cdot (f\langle \Delta \mathbf{v} \rangle) + \frac{1}{2}\frac{\partial}{\partial \mathbf{v}}\frac{\partial}{\partial \mathbf{v}} : (f\langle \Delta \mathbf{v} \Delta \mathbf{v} \rangle) \tag{2.21}$$

where $\langle \Delta \mathbf{v} \rangle$ is the rate of advection and $\langle \Delta \mathbf{v} \Delta \mathbf{v} \rangle$ is the rate of diffusion. Expansion of f using Legendre polynomials can solve the Fokker-Planck equation. At steep thermal gradients Fokker-Planck treatments predict electron transport inhibition whereas the Spitzer-Harm treatment overestimated the electron transport [47].

The mean free path of electrons, λ_e with velocity, v is proportional to v^4 and the collision frequency is proportional to $\propto \nu^{-3}$ [34]. For large temperatures, electrons with high velocities have low cross sections, hence hot electrons fail to thermalise. The hot electrons create a hot tail in the Maxwellian profile producing a two temperature plasma. This phenomena is evident from the x-ray bremsstrahlung emission due to hot electrons with measured hot electron temperature obtained in (chapter 6).

The Fokker-Planck method to describe energy transport is extremely computationally expensive when simulating $\sim 10^{15}$ particle systems.

Flux limited diffusion

Thermal conduction is limited to the free streaming limit and so it is usually assumed that the energy transport Q_{FS} arises due to the movement of energy at some fraction f of the thermal velocity, where f is known as the flux limiter, typically ranging between 0.01 - 0.15. We can write for the flux limited energy transport,

$$Q_{FS} = f n_e k_B T_e v_{th} \tag{2.22}$$

where v_{th} is the thermal sound speed. The flux limiter value is chosen by comparison with experimental or Fokker-Planck simulation data. The Spitzer-Harm heat flux and the free-streaming heat flux can be harmonically combined by,

$$\frac{1}{Q} = \frac{1}{Q_{SH}} + \frac{1}{Q_{FS}} \tag{2.23}$$

to enable a smooth transition between regimes of different gradient. Flux limited diffusion models are relatively attractive due to their simplicity and ease of use in hydrodynamic fluid codes. For chapter 5 spectral line ratios of iron lines were used to determine the flux limiter value (see figure 5.9). Chapter 6 identified the flux limiter by comparing the transmission profiles produced from varying flux limiters to the experimentally deduced transmission of the extreme ultraviolet laser through the iron layer.

2.4.2 Radiative energy transport

Radiation transport is highly important in stellar evolution and many planetary atmospheres [1] and the interaction of high energy lasers by a solid target can produce highly radiative plasmas. This section will introduce how radiation emitted in a laser plasma can transport energy into the overdense 'cold' plasma.

The radiation field

Lasers which impinge on a solid target typically produce highly radiative plasma sources. This is because plasma emission is proportional to electron density n_e and ion density n_i with emissivity $\propto n_e n_i$. Since the laser produced plasma temperature rises sharply at the critical density, the high electron densities found near the critical density ($n_e \approx n_c$) efficiently convert the laser energy into soft x-rays. The hot plasma typically emits photons $\sim$ keV energy (see figure 6.15) [48].

The emission radiation from a plasma is a combination of bound-bound, bound-free and free-free emission processes depending on the atomic number of the target. The radiation field is highly dependent on the atomic composition of the plasma. X-ray photons have a larger mean free path compared to the thermal electrons,

so the heating of solid target material due to radiation occurs at a much greater depth in a target than heating due to thermal conduction.

The spectral intensity, I_v describes the radiation energy in terms of spatial coordinates (r), solid angle (Ω), frequency (ν) and time (t) as,

$$I_v(r, \Omega, t)d\nu d\Omega = h\nu c f(\nu, r, \Omega, t)d\nu d\Omega \tag{2.24}$$

where $f(\nu, r, \Omega, t)$ describes the distribution of photons within a frequency interval ν to $\nu + d\nu$. For chapter 5 the solid angle comprises the projected emission onto the diffraction grating and the CCD detector. In chapter 5 the emissivity of the iron plasma was calculated on an absolute scale by calculating the spectral intensity of the iron plasma source.

To simulate the wide range of photon frequencies in the radiation field it is important to introduce a multigroup diffusion model. The radiation spectrum is considered in photon energy 'bands' (or groups) with radiation energy transport within a group determined by an average opacity for the group. In chapter 5 and 6 multigroup diffusion models were used in the HYADES simulations. Typically 100 groups were used ranging logarithmically from 0.1 - 40 keV. A parameter scan showing a range of different multigroups and photon energies is shown in figure 6.11. The benefit of using a multigroup diffusion model is that departures from a Planckian radiation distribution can be simulated.

The interaction of radiation and matter

Propagating radiation is affected by and interacts with matter through various absorption and emission processes. A pencil-like ray of photons passing through a plasma will lose its energy exponentially and become attenuated so that its

intensity I_ν changes such that,

$$I_\nu = I_0 exp\left[-\int_0^x \kappa_\nu dx\right] \tag{2.25}$$

where κ is the mass absorption coefficient[2] and I_0 is the initial intensity. The optical depth, τ_ν is defined as the distance at which the incident intensity is attenuated to 1/e of the original value and is given by,

$$\tau_\nu = \int \kappa_\nu dx \tag{2.26}$$

where the reciprocal $(1/\tau)$ describes the mean distance a photon travels before it is absorbed or scattered. A material is considered optically thin when the optical depth is much less than 1, i.e $\tau << 1$. Optically thick plasmas have an optical depth much greater than 1, i.e $\tau >> 1$. For optically thick plasmas, the radiation is transported diffusively.

The radiation transfer equation determines how radiation is transported through material. The radiation transfer equation can be formulated using a three dimensional coordinate system and vector operators, however the following equation describes the path of radiation in the single x direction. Consider a ray starting at x and leaving a plasma element at x + dx. The intensity I_ν change is given by,

$$\frac{dI_\nu}{dx} = \epsilon_\nu - \kappa_\nu I_\nu \tag{2.27}$$

where ϵ_ν is the emissivity and κ_ν is the absorption coefficient.

To solve the radiation transfer equation, the opacity of the plasma must be accurately known. Section 3.3 gives a brief introduction to various mean opacity models. Laser produced plasmas contain an ensemble of ionisation states with

[2]also known as the extinction coefficient.

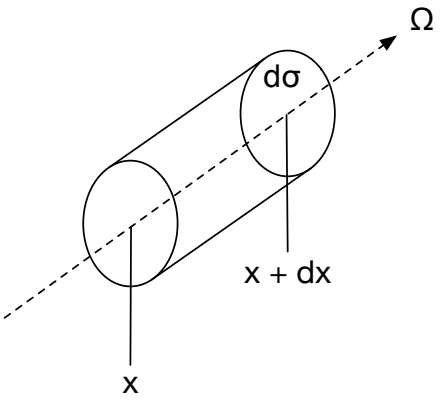

FIGURE 2.7: This figure shows a ray traversing a cylindrical plasma medium. The radiative transfer equation calculates the spectral intensity in time at each spatial point along the x direction.

complex atomic structures, therefore atomic models are required to simulate the opacity of many electron elements such as iron. This will be discussed in section 3.1.

2.4.3 Hot electron transport

Laser-plasma interactions such as resonance absorption (discussed in section 2.3) and parametric instabilities can produce hot electrons [34].

Stimulated Raman scattering (SRS), stimulated Brillouin scattering (SBS) and two plasmon decay (TPD) are all examples of parametric instabilities. Such processes occur below the critical density in the underdense plasma region where the laser electromagnetic field can directly interact with the plasma. Therefore, for chapters 5 and 6 parametric instabilities are not responsible for the direct heating of the buried iron layer.

SBS occurs when an incident electromagnetic wave interacts with the fluctuation in the ion density to produce a scattered electromagnetic wave and an ion acoustic wave. However, SRS occurs due to the interaction between the incident laser electromagnetic wave and the fluctuations in the electron plasma density to produce

an scattered electromagnetic wave and high energy electron plasma wave. TPD is a process when the incident laser electromagnetic wave decays into two plasma waves.

Parametric instabilities typically dominate at higher laser irradiance ($> 10^{15}$ Wcm^{-2}). However, because short duration laser pulses (¡ 100 fs) avoid significant ion motion, hydrodynamic instabilities and certain parametric instabilities (SBS) can be negligible.

The hot electron temperature scales as,

$$T_{hot} = \frac{m_e c^2}{2e} a_0^{2/3} \sim (I_{18}\lambda_{\mu m}^2)^{1/3} \tag{2.28}$$

with respect to laser intensity I and wavelength λ [49]. Plasmas which produce hot electrons are often described using a two-temperature Maxwellian distribution (see figure 2.8) because the high energy hot electrons perturb the Maxwellian profile and produce a hot temperature tail. The hot electrons temperature can be diagnosed from their bremsstrahlung radiation, Kα emission [50] or an electron spectrometer [51].

The absorption of hot electrons into a solid target is typically small because they weakly couple with the surrounding plasma. The electron interaction cross section with matter decreases with a $1/p^2$ momentum dependence, where p is the momentum. The average absorption coefficient for an electron distribution with an electron temperature, T (in units of 10 keV) is given by [52],

$$\sigma_{av}(T) = \int_0^\infty \sigma_0 \frac{exp(-E/T)}{E^2} dE = 6.5\frac{\sigma_0}{T} \tag{2.29}$$

where σ_0 is the absorption coefficient per unit mass. The absorption, A is given by,

$$A = 1 - exp(-\sigma_{av}(T)\rho\Delta x) \tag{2.30}$$

where ρ and Δx is the density and thickness of the layer. Figure 6.15(a) shows the absorption, A of hot electrons within the 50 nm iron layer. It is noted that the hot electron absorption is relatively small compared to the absorption of radiation (see figure 6.15).

The propagation of hot electrons leads to a higher concentration of electrons at the rear-side of the target, therefore producing an electric field between the relatively immobile positively charged ions [34]. This electric field slows down the hot electrons and produces a return current which further heats the buried layer target due to ohmic heating effects. The strength of the electric field is given by Ohm's law,

$$j_c \approx -j_H = \sigma_e \mathbf{E} \tag{2.31}$$

where the cold current, j_c balances the hot electron current j_H due to charge neutrality, σ_e is the electrical conductivity and $\mathbf{E}$ is the electric field.

In chapter 6 the hot electron temperature was detected using a four-channel diode array [53]. Filters were placed over the four diodes and each recorded the hot electron bremsstrahlung emission within a narrow spectral region. The four filters which were used in chapter 6 were 75 um Al, 150 um Al, 75 um Ti and 100 um Cu. Therefore, the hot electron temperature $\sim$ 30 KeV was deduced directly from the gradient of the hot Maxwellian electron distribution tail.

The fraction of laser energy which is converted into hot electrons varies upto 40% [54] The conversion efficiency has a wide range because it depends on many parameters such as laser spot size, spot quality, laser prepulse, laser polarisation, target characteristics and laser intensity. Key et al [54] investigated the laser

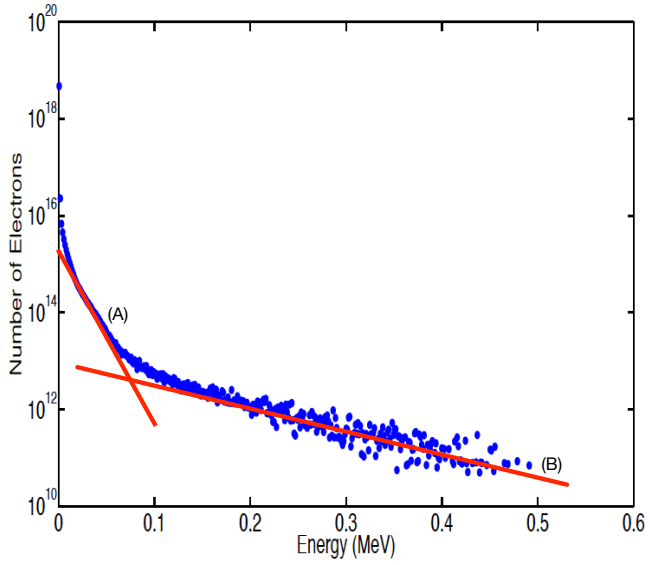

FIGURE 2.8: Electron energy spectrum shown produced from the EPOCH PIC simulation code for conditions where the laser incident intensity is 3×10^{16} Wcm^{-2}. The two-temperature Maxwellian profile shows the thermal electrons as line (A) and the hot electron tail is represented by (B). This image is taken from Culfa et al [51].

energy-hot electron conversion efficiency as a function of laser intensity (see figure 2.9).

HYADES simulations enable the incorporation of hot electron heating of the target by adding energy to the simulation cells. Chapter 5 shows how hot electron heating can be estimated using the emission spectra from iron buried layer targets. For chapter 6 the hot electron fraction was chosen as 10%, a value based on the Key et al scaling (figure 2.9) of hot electron efficiency with respect to laser intensity.

2.5 Conclusion

In summary, Nd:YAG and Ti:Sapphire laser crystals can be used to produce short pulse lasers ($\sim$ ps) to irradiate buried layer targets. Using CPA and multi-pass glass amplifiers high intensity short pulsed lasers can be used to produce uniform high density and temperature plasmas. The laser energy is absorbed mainly by

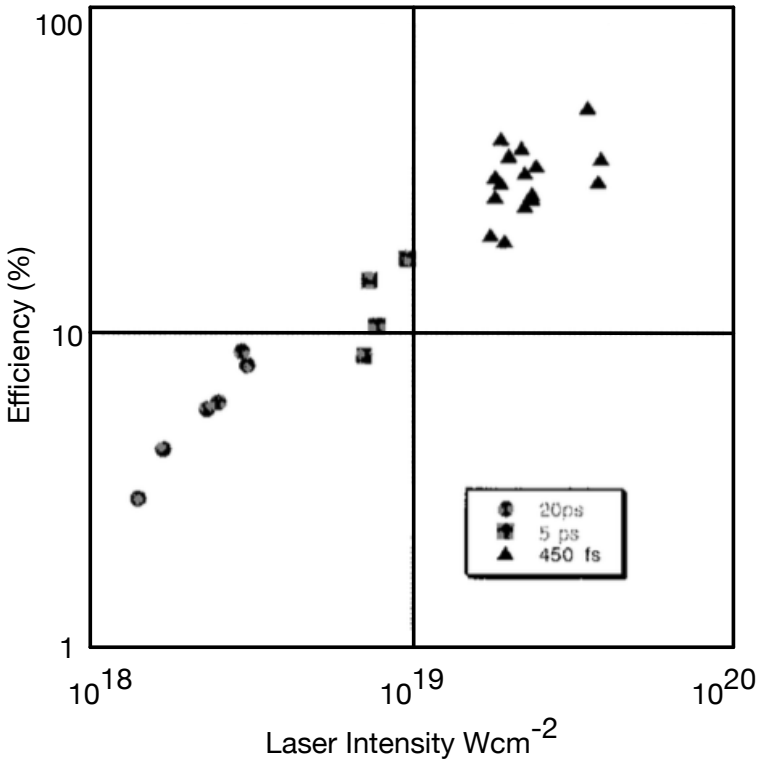

FIGURE 2.9: The conversion efficiency of laser energy into hot electrons as a function of laser intensity I. This figure is taken from Key et al [54].

inverse bremsstrahlung upto the critical density. Resonance absorption processes can produce hot electrons which subsequently propagate into the overdense plasma region. The dominant energy transport methods that ensue between the critical density and the ablation surface are radiation transport, hot electron heating and thermal electron conduction.

Chapter 3

Background theory of plasma spectroscopy

To investigate the energy transport mechanisms described in the previous chapter, plasma spectroscopy and an extreme ultraviolet (EUV) laser were used in chapters 5 and 6 to diagnose the buried iron layer conditions. This chapter introduces important aspects of plasma spectroscopy such as ionisation models, ionisation potential depression, types of radiation emission, line broadening effects and opacity.

3.1 Plasma ionisation

Figure 3.1 shows the increase in ionisation energy for iron as a function of atomic charge, Z. The impact of a laser pulse onto an iron target produces an ensemble of ionisation species because the higher ionisation stage can exist before the complete ionisation of the previous stage. The average degree of ionisation Z^* is given by,

$$Z^* = n_e/\Sigma_i n_i \tag{3.1}$$

where n_e is the electron density and n_i is the ion density. The average ionisation is central to many plasma processes including energy transport, where the electron thermal conductivity is proportional to $(Z^*)^{-2}$ and the bremsstrahlung radiation emission rate is proportional to $(Z^*)^2$ [33]. An example of the distribution of ionisation species as a function of time is shown in figure 5.12.

An ionising plasma occurs when the rate of ionisation is greater than the recombination rate. However, when recombination is greater than the ionisation rate a recombining plasma is produced. The balance between ionisation and recombination determines the average ionisation, Z^*. Consequently, the ionisation balance of a plasma is dependent on the plasma temperature, density and the ionisation energies of the atom [33].

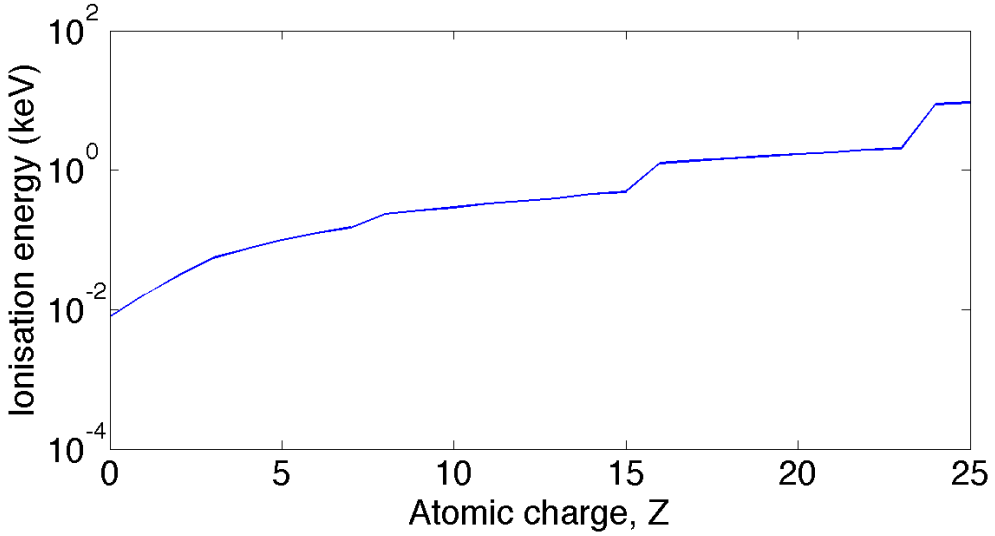

FIGURE 3.1: The ionisation energy as a function of atomic charge, Z for Iron taken from the NIST database.

3.1.1 Local thermodynamic equilibrium (LTE)

In complete thermal equilibrium, ions, electrons and photons are all in equilibrium with radiative and collisional processes balanced such that the electrons behave as a Maxwellian distribution and the radiation field is Planckian. With optically

thin plasmas photons can escape the plasma and the radiation field departs from a Planckian distribution. However, if collisional processes dominate over radiative processes a plasma can be at a local thermodynamic equilibrium (LTE) where the electrons, ions and ionisation balance are in equilibrium, but the radiation field is not in equilibrium. This will occur at high densities when collisional proceses dominate over radiation processes in determining the populations of quantum states. The time it takes to reach local thermodynamic equilibrium conditions is typically $\sim$ ps in the high density plasmas considered in chapters 4 and 5 [55].

3.1.2 Saha ionisation model

The Saha LTE model applies to ionized non-degenerate plasmas in thermal equilibrium [33]. The Boltzmann equation describes the ratio of upper and lower levels within the same ionisation state by,

$$\frac{N_{z+1}}{N_Z} = \frac{g_{z+1}}{g_1} exp\left(\frac{\Delta E}{kT_e}\right) \tag{3.2}$$

where $z+1$ represents the upper level and z is the lower level. ΔE is the energy difference between upper and lower levels and g represents the degeneracy of each level. The Saha-Boltzmann equation extends this concept and gives the ratio of population densities for successive ionisation states as [56],

$$\frac{N_{z+1}(g)}{N_z} = 2\left(\frac{g_{z+1}(p)}{g_z(q)n_e}\right)\left(\frac{m_e k_B T_e}{2\pi\hbar^2}\right)^{3/2} exp\left(\frac{-E_{z,q}}{k_B T_e}\right) \tag{3.3}$$

where, g is the degeneracy, m_e is the electron mass, T_e is the electron temperature, n_e is the plasma electron density and $E_{z,q} = E_z(\infty) - E_z(q)$ is the ionisation energy of the level q. Chapter 4 uses the Saha-Boltzmann equation to predict the electron temperature and density by using spectral line-ratios of adjacent ionisation states.

3.1.3 Continuum lowering

Depression of the ionisation potential well which is also known as continuum lowering can reduce the energy required to ionise bound electrons. The Stewart-Pyatt (SP) and the Ecker-Kroll (EK) models are used in chapter 4 to describe the effect of continuum lowering.

The Stewart-Pyatt model interpolates between the Debye-Huckel theory[1] and the ion-sphere model [57]. The Ecker-Kroll model determined the mean distance between the total number of particles. The continuum lowering according to the Stewart-Pyatt model, ΔE_{SP} is given by,

$$\Delta E_{SP} = \frac{k_B T}{2(z^*+1)} \left[\left(\frac{3(z^*+1)ze^2}{4\pi\epsilon_0 \lambda_D k_B T} + 1 \right)^{2/3} - 1 \right] \tag{3.4}$$

where λ_D is the Debye length including both electrons and ions. The continuum lowering according to the Ecker-Kroll model is given by,

$$\Delta E_{EK} = \frac{ze^2}{4\pi\epsilon_0 r_{EK}}. \tag{3.5}$$

where $r_{EK}^3 = \frac{3}{4\pi(n_e+n_i)}$. The validity of SP and EK models are being questioned after an experiment using x-ray free electron laser (XFEL) diagnosed continuum lowering effects using spectral analysis of K-shell fluorescence and the binding energy. This experiment suggested that SP disagrees significantly and predictions are best described using the EK model [57]. However an experiment carried out using the Orion laser facility suggested that SP models were more accurate in simulating ionisation potential depression [15]. The EK models was initially developed for strongly coupled plasmas and was later extended to weakly coupled models using the Stewart-Pyatt model [58].

[1]Debye-Huckel theory describes ionisation potential depression at low plasma densities and high temperatures, however breaks down at high densities.

3.1.4 Collisional-radiative ionisation model

In a collisional-radiative (CR) ionisation model the population distribution is determined by the balance between radiative and collisional processes. Collisional processes depend on the local plasma conditions whereas radiative processes can require knowledge of the radiation field emanating from the whole plasma. The spectra we observe is a combination of bound-bound, bound-free and free-free transitions which all depend on the distribution of electrons in their respective atomic levels.

Population kinetics can determine the ionisation and atomic level population for a given electron temperature and density. In a steady state the rate of population and depopulation are equal [59]. At high electron densities ($n_e \sim 10^{24}$ cm^{-3}), LTE conditions can be assumed because collisional processes dominate and the population distribution is governed by the Saha equation [56]. The population kinetics for low density coronal plasmas ($n_e \sim 10^{10}$ cm^{-3}) can be found using rate equations to simulate the transitions from a ground state to an excited level. Collisional-radiative plasmas can be used for intermediary plasma densities ($n_e \sim 10^{19}$ cm^{-3}) where populations are calculated using rate equations for collisional and radiative processes. These rate equations typically include rate coefficients for electron impact ionisation, three-body recombination, electron impact excitation, electrom impact de-excitation, radiative recombination and dielectronic recombination processes [59].

Einstein's description of an atom interacting with a radiation field is described in terms of the rate equation, which describes how the electron population density for level N_j changes in time due to radiation processes alone i.e

$$\frac{dN_j}{dt} = N_i B_{ij} \rho(\omega_{ij}) - N_j B_{ji} \rho(\omega_{ij}) - N_j A_{ji} \tag{3.6}$$

where B_{ij}, B_{ji} and A_{ij} are known as Einstein A and B coefficients. The population of a given level is dependent on absorption ($N_i B_{ij} \rho(\omega_{ij})$), stimulated emission ($N_j B_{ji} \rho(\omega_{ij})$) and spontaneous emission ($N_j A_{ji}$) processes. It is important to note that these Einstein relations,

$$\frac{A_{ji}}{B_{ji}} = \frac{\hbar \omega_{ji}^3}{\pi^2 c^3} \tag{3.7}$$

$$g_i B_{ij} = g_j B_{ji} \tag{3.8}$$

although derived under thermal equilibrium conditions can be applied to non-thermal plasmas. They are also independent of the blackbody radiation field.

3.1.5 Hydrogenic average atom model

The average atom model [60–63] describes a fictitious atom where the average number of electrons are distributed among shells, therefore describing the average occupation of each shell in the plasma [62]. The model assumes a Thomas-Fermi electrostatic potential in conjunction with the ion sphere model, from which the average number of electrons are distributed amongst shells according to Fermi-Dirac statistics [59].

The ionised material package (IMP) opacity model uses the average atom model to simulate the atomic data of iron at a range of different temperatures and densities (see figure 4.16). Due to the simplifications of the average atom model the opacity effect which arises from resonance transitions and forbidden $\Delta n = 0$ lines are not taken into account. Chapter 5 highlights the importance of including these transitions in the atomic model as they can significantly contribute to the mean opacity.

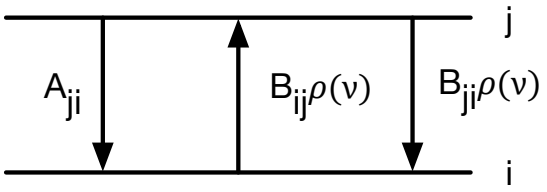

FIGURE 3.2: Figure showing three radiative processes between energy level i and j. The probability of spontaneous, stimulated and absorption transitions are given by the Einstein A and B coefficients, A_{ji}, B_{ji} and B_{ij} respectively. The absorption and stimulated radiative processes are dependent on the radiation energy density whereas spontaneous emission is independent.

3.2 Spectroscopy

The formation of spectra depends on emission and absorption atomic processes. Spectroscopy has been extensively used to diagnose plasmas, both astrophysical and in the laboratory [18, 64, 65]. Radiation emission from atoms, ions or molecules within a plasma can deliver local information such as temperature, density and ionisation. Plasmas produced by laser irradiation typically reach hundreds of eV and therefore emit short (> 0.1 nm) wavelength x-ray spectra.

3.2.1 Radiative processes

Bound-bound emission

Radiative processes cause electrons to transition between an excited upper level and a lower level and therefore introduce emission and absorption lines into the spectra. This may occur by spontaneous emission or stimulated emission. Spontaneous emission, $\epsilon(j \rightarrow i)$ is dependent on the electron population density in the upper level (N_j) and the atomic transition probability, $A(j \rightarrow i)$. The spontaneous electron transition from upper excited level, (N_j) to a lower level (N_i), releases a photon with a characteristic energy, $E(j) - E(i) = h\nu_{ji}$. Stimulated emission occurs when an incident photon interacts with an atom in the upper level stimulating

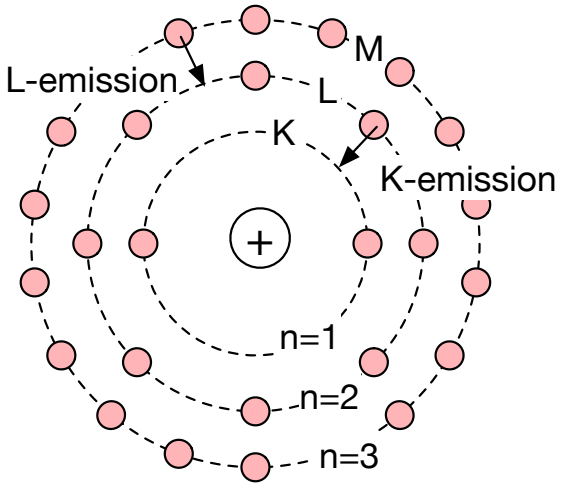

FIGURE 3.3: This figure shows the K, L and M shells and associate transitions labels. The maximum number of electrons per shell is given by the degeneracy of each shell ($2n^2$) rule, where n is the principal quantum number.

the decay into a lower level, thus releasing a photon into the same mode with the identical frequency, direction and polarisation as the incident photon. Absorption of a photon with energy E_{ij} can excite an electron to the upper excited level N_j.

The strength of a particular line transition is dependent on the atomic structure and the surrounding plasma conditions. Oscillator strengths, f' measure the intrinsic strength of an atomic transition and are given by [66],

$$f'_{ij} = \frac{i}{8\pi^2 c r_e} \frac{g(i)}{g(j)} (\lambda_{ij})^2 A_{ji} \tag{3.9}$$

where g is the degeneracy of each level and r_e is the classical electron radius ($\frac{e^2}{4\pi\epsilon_0 m_e c^2}$). The Thomas-Reche-Kuhn sum rule states,

$$\sum_j f'_{ij} = N \tag{3.10}$$

where summation of the f'-value for all possible transitions from the upper level must be equal to the total number of electrons, N involved in the transitions. The transitions probabilities used in chapter 4 were taken from the NIST database

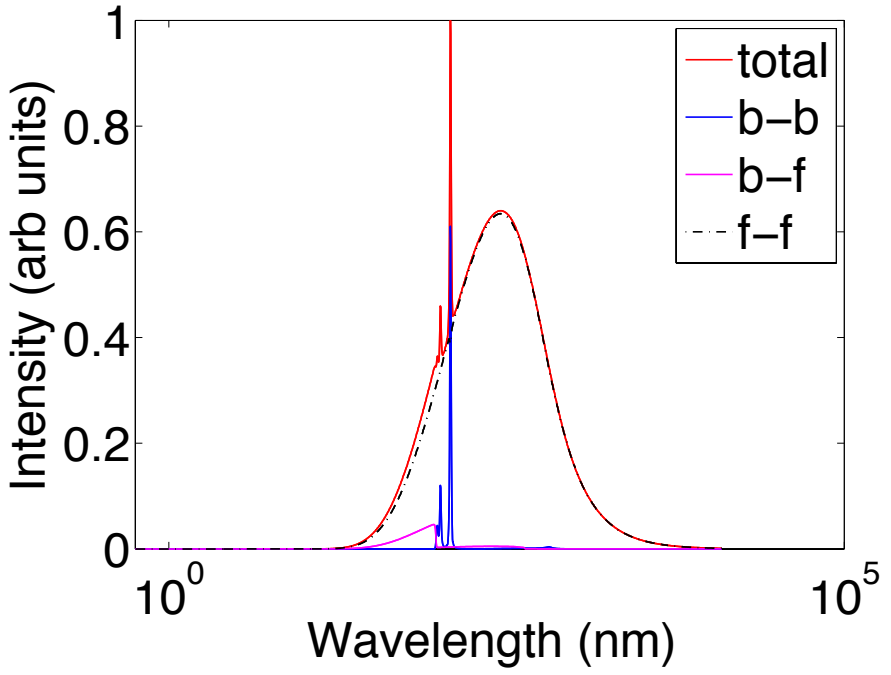

FIGURE 3.4: PrismSPECT simulated spectra for hydrogen at electron temperature 10 eV, ion density $1 \times 10^{19}\text{cm}^{-3}$ and thickness 1 mm. The bound-bound, bound-free and free-free emission is shown with the total emission overlaid.

[67]. The NIST database is produced through comparison between theory and experimental data to accurately determine the transition probability.

At thermal equilibrium conditions the principle of detailed balance states that the rate of radiative processes from an upper excited level (N_j) to a lower level (N_i) is equal to its inverse process. For this dynamic equilibrium Einstein postulated that,

$$N_i B_{ij} \rho(\nu) = N_j B_{ji} \rho(\nu) + N_j A_{ji} \rho(\nu) \tag{3.11}$$

where stimulated ($N_j B_{ji} \rho(\nu)$), spontaneous ($N_j A_{ji}$) and absorption ($N_i B_{ij} \rho(\nu)$) rates are balanced. The Einstein A and B coefficients represent transition probabilities. Using these relations and rate equations it is possible to simulate the emission spectra from a plasma (see chapter 4). Figure 3.4 for example, used the collisional-radiative PrismSPECT code to simulate spectra for hydrogen showing bound-bound, bound-free and free-free emission.

For multi-electron atoms such as iron, emission can arise from multiple energy levels. This thesis focusses on emission spectral lines which originate from the M-shell iron level. L-shell emission occurs due to electron transitions from the principle quantum number, $n = 3$ to $n = 2$. The occupancy of electron states depends on the quantisation of variables such as energy and momentum with their associated quantum numbers: principal quantum number (n), orbital quantum number (l) and magnetic quantum number (m_l). The L-shell level can be specified with the following quantum numbers,

$$L - shell : n = 2, l = 0, 1, m_l = 0, \pm 1, m_s = \pm\frac{1}{2} \tag{3.12}$$

L-shell spectra can be complex because electrons can follow multiple decay paths therefore producing numerous spectral lines. In chapter 4 the COMET laser was used to ionise buried iron layer targets to electronic configurations which were Li-like to Ne-like with ground states,

$$\begin{aligned} [l = 0, m_l = 0] &\rightarrow 1s^2 2s^1(Li), 1s^2 2s^2(Be), \\ [l = 1, m_l = 0, \pm 1] &\rightarrow (1s^2 2s^2) + 2p^1(B), +2p^2(C), \\ &\rightarrow +2p^3(N), +2p^4(O), +2p^5(F), +2p^6(Ne). \end{aligned} \tag{3.13}$$

Free-bound emission

Radiative recombination also known as free-bound emission occurs when a free electron with an initial energy, E_{ke} is captured into a bound state (q). As a result, a photon with energy, $h\nu$, is emitted,

$$h\nu = E_{ke} + (E_R - E(q)) \tag{3.14}$$

where, E_R is the ionisation energy and $E(q)$ is the energy of the bound state. As the electron can have an infinite continuum of initial energies, E_{ke} the bound-free emission spectra is also continuous except for discontinuities at the absorption edge. Here the incident photon with an energy slightly above the binding energy of the electron shell (K,L,M, etc.) will more likely be absorbed. Radiation recombination and its inverse process photo-ionisation are shown as,

$$A^{(z+1)+}(g) + e^{-1} \rightleftharpoons A^{z+}(q) + h\nu \tag{3.15}$$

where z denotes the charge of the atoms and g represents the ground state. The rate of recombination can be determined using the principle of detailed balance for plasmas at thermodynamic equilibrium. The spectral free-bound emission coefficient is [66],

$$\begin{aligned}\epsilon_v^{fb}(\nu) = \frac{64\sqrt{\pi}(\alpha a_0)^3 E_R}{3\sqrt{3}} \times n_Z n_e Z^4 \left(\frac{E_R}{k_B T_e}\right)^{3/2} \times exp\left(-\frac{h\nu}{k_B T_e}\right) \\ \times \sum_{n_q \geq n_{qmin}} \frac{1}{n_q^3} exp\left(\frac{Z^2 E_R}{n_q^2 k_B T_e}\right) G_{n_q}^{bf}(\nu)\end{aligned} \tag{3.16}$$

where the multiplicative correction Gaunt factor, $G_{n_q}^{bf}(\nu)$ introduces quantum mechanical effects [59].

Free-free emission

Free-free emission also known as bremsstrahlung emission also contributes to the total continuum emission of a plasma. Under the classical description bremsstrahlung emission occurs when electrons are accelerated in an electric or magnetic field.

Quantum mechanically this is described as a free-free transition between continuum states [1]. The free-free emission coefficient is given by [59],

$$\epsilon^{ff}(\nu) = \frac{32\sqrt{\pi}(\alpha a_0)^3 E_R}{3\sqrt{3}} \times n_Z n_e Z^2 \left(\frac{E_R}{k_B T_e}\right)^{1/2} \times exp\left(-\frac{h\nu}{k_B T_e}\right) G^{ff}(\nu) \tag{3.17}$$

where G^{ff} is the free-free Gaunt factor. At short wavelengths the the free-free emission coefficient is dominated by the $exp(-h\nu/k_B T_e)$ term. The plasma temperature can be determined from the slope of the continuum. Using this technique the thermal plasma temperature is calculated to be ~ 500 eV in chapter 4.

Due the presence of hot electrons a bi-Maxwellian distribution best describes laser produced plasmas. The bi-Maxwellian distribution has a thermal component which describes the bulk of the plasma electrons and follows a Maxwellian distribution. However, the small fraction of hot electrons found in the 'hot tail' of the electron distribution, have a secondary Maxwellian profile at a higher temperature. The diode array used in chapter 5 recorded the bremsstrahlung (free-free) x-ray emission from the hot electrons.

3.2.2 Collisional processes

Laser produced plasmas are typically highly collisional regimes. At extreme densities and temperatures, similar to those found in chapter 4 collisions between electron-electron and electron-ions become highly frequent. Collisional excitation occurs when an electron undergoes inelastic collisions and subsequently is excited to higher energy state. The inverse process is known as collisional de-excitation. When the collisional processes are more dominant than the radiative processes it is possible to assume the plasma is in local thermodynamic equilibrium (LTE).

3.2.3 Line broadening

The spectral line shape and width is dependent on the atomic transition and the plasma environment. The plasma conditions strongly affect the plasma line shape due to natural, Doppler, collisional and Stark broadening effects. The line shape function, $\mathcal{L}$ uses for example Gaussian, Lorentzian or Voigt profiles to describe the shape of a spectral line. Typically the line shape function,$\mathcal{L}$ is normalised such that,

$$\int_{line} \mathcal{L}(\omega) d\omega = 1 \tag{3.18}$$

where ω is the angular frequency.

Natural broadening

The Heisenberg uncertainty principle states that for particles with life time Δt (e.g. excited electrons) the energy level is smeared by ΔE due to an uncertainty in the measured energy, where

$$\Delta E \Delta t \geq \frac{\hbar}{2}. \tag{3.19}$$

As a result line transitions are recorded with a minimum linewidth given by ΔE. The transition probability, A_{ji} is inversely proportional to the mean life time of the upper level, N_j (assuming the lower energy level has a much longer lifetime). For the principal iron Li-like (Fe XXIV) line transition identified at 11.171$\mathring{A}$ the transition probability is 2.18×10^{13} s^{-1} [67], thus corresponding to an energy uncertainty of $\simeq 1.5 \times 10^{-3}$ eV. However, a more accurate description includes the lifetime of both upper and lower levels. Therefore the energy uncertainty is given by,

$$\Delta E_{total} = \Delta E_{upper} + \Delta E_{lower} = \hbar \left(\sum_i A_{ui} + \sum_j A_{lj} \right) \tag{3.20}$$

The line shape function which best describes the natural broadening effects is given by a Lorentzian profile, $I(\omega)$,

$$I(\omega) = \frac{\gamma/2\pi}{[(\omega - \omega_0)^2 + \gamma^2/4]} \tag{3.21}$$

where $\gamma = \sum A_{ij} = \frac{\Delta E_{total}}{\hbar}$. The natural broadening contribution to the total line width of a spectral line is typically small. Therefore the resolution limit for atomic spectroscopy is often dependent on other broadening mechanisms such as Doppler broadening.

Doppler broadening

The spectral line shape is affected by the bulk plasma motion and thermal Doppler broadening effects. Thermal Doppler broadening occurs in plasmas due to the thermal motion of radiation emitting plasma ions. For plasmas with a Maxwellian velocity distribution a Gaussian line shape function can be used to describe thermal Doppler broadening effects. The thermal Doppler broadened width is given by,

$$\frac{\Delta\lambda}{\lambda} = \frac{1}{c}\sqrt{\frac{2k_BT}{M}} \tag{3.22}$$

where the velocity of the ion is given by $\sqrt{\frac{2k_BT}{M}}$ and M is the atomic mass of iron. For peak emission conditions in the iron layer ($\sim$ 700 eV) the Li-like 11.171 Å line is Doppler broadened by 1.82 mÅ. The Voigt line profile function which includes Gaussian and Lorentzian characteristics is typically used to model Doppler broadened spectra [66].

In chapter 4 the bulk plasma expansion occurs predominantly normal to the target. The central frequency of the emitted radiation is often blue or red shifted in laser produced plasmas due to the plasma expansion towards or away from the

observer. As a result bulk Doppler broadening is minimised in the direction of the spectrometer viewing angle (5° from the target surface). The wavelength Doppler shift due to the plasma expansion can be calculated using [68],

$$\lambda = \lambda_0(1 + \frac{v_i}{c}\cos(\theta)) \tag{3.23}$$

where λ is the shifted wavelength, λ_0 is the wavelength in the rest frame, v_i is the velocity of the emitting ion, θ is the viewing angle measured from target normal (85°) and c is the speed of light. Using equation 2.1 the emitting velocity can be estimated at $\sim 2 \times 10^7$ cm^{-1} for the conditions of the experiment of chapter 5. For the FeXXIV Li-like iron transition at 11.171 Å the wavelength is blue shifted by -0.65 mÅ. This Doppler shift due to bulk plasma motion is negligible compared to the spectral resolution ($\simeq$ 0.02 Å).

Collisional and Stark broadening

The irradiance of high powered laser on a solid target can lead to highly collisional plasmas. Collisional broadening occurs due to interactions between electrons and ions neighbouring ions which perturb the energy levels. As the collision frequency is dependent on the plasma pressure this type of broadening is also known as pressure broadening. To a first approximation, collisionally broadened spectral lines have a Lorentzian line profile with spectral width determined by the time between electron collisions with the ions.

Broadening in ions with different m sub-levels such as He-like and H-like ions is called Stark broadening as the m sub-levels shift in energy according to the local electric field in the plasma. In chapter 4 Stark broadening effects were taken into account when simulating synthetic spectra using the PrismSPECT code. Figure

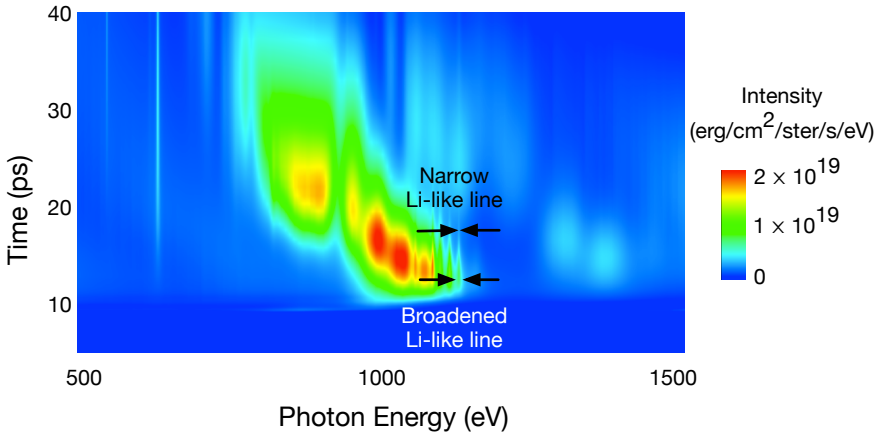

FIGURE 3.5: PrismSPECT collisional-radiative code simulation of time-dependent streaked spectra from the buried iron layer target. The HYADES simulation data was post-processed into PrismSPECT and the L-shell time dependent emission was simulated showing broadening effects. Spectral lines are broadened initially due to the high electron density, however at later times ~ 20 ps the electron density is lower due to plasma expansion, thus spectral lines are more narrow.

3.5 shows PrismSPECT simulated streaked spectra for the laser irradiated buried iron layer target (see chapter 5).

3.3 Opacity

The opacity of a material determines the attenuation of transmitted radiation in a material [69]. The opacity (σ) of a material is often measured in units of $\mathrm{cm^2 g^{-1}}$ so that the transmitted intensity I varies with distance x as,

$$I(x) = I(0)exp(-\int \sigma \rho dx) \tag{3.24}$$

where ρ is the material density. Opacity (σ) is dependent on several parameters such as temperature, density, frequency and elemental composition.

The propagation of radiation is determined by the total absorption coefficient (κ_ν), such that $\kappa_\nu = \sigma\rho$. We can write

$$\kappa_\nu = \kappa_\nu^{ff} + \kappa_\nu^{bf} + \kappa_\nu^{bb} \tag{3.25}$$

which combines free-free (κ_ν^{ff}), bound-free (κ_ν^{bf}) and bound-bound (κ_ν^{bb}) absorption coefficients. Frequency averaged opacities are often used in calculations of energy transport due to radiation used. The Rosseland mean opacity (σ_R) which governs radiation flow in plasmas, harmonically combines the opacity for all frequencies and is given by,

$$\frac{1}{\sigma_R} = \frac{\int_0^\infty \frac{1}{\sigma_\nu}\frac{dB_\nu}{dT}d\nu}{\int_0^\infty \frac{dB_\nu}{dT}d\nu} \tag{3.26}$$

where σ_ν is the opacity at frequency, ν. B_ν is the Planck radiation distribution and T is the temperature. As the opacity is harmonically combined the smallest opacities found in frequency 'windows' will contribute most to the Rosseland mean opacity. This is because the Rosseland mean opacity predicts when the radiation flow is the greatest, i.e when $\frac{dB_\nu}{dT}$ is a maxima [1]. The Rosseland mean opacity is typically used to describe radiation flow in stellar interiors and ICF plasmas.

The Planck mean opacity, σ_P which is given by,

$$\sigma_P = \frac{\int_0^\infty \sigma_\nu B_\nu d\nu}{\int_0^\infty B_\nu d\nu} \tag{3.27}$$

To simulate the transport of radiation energy over a wide range of photon frequencies a multigroup diffusion model is often required. The radiation spectrum is split into several groups (bins) and within each group the radiation energy transport is calculated using an average opacity for the group. The investigation in chapters 5 and 6 both used a multigroup diffusion model in the HYADES code. This measure of frequency averaged opacity is applied to radiation absorption in optically thin plasmas. The Rosseland mean opacity incorporates scattering effects whilst the

Planck mean opacity does not. The opacity due to scattering effects (Thomspon scattering) becomes significant only when the density of free electrons is very high.

Opacity is important in inertial confinement fusion where for example, cocktail hohlraums are doped with high Z materials which increase the mean opacity of the hohlraum wall, therefore reduce the radiative losses to the wall. Opacity is important in solar and stellar modelling. The depth of the solar convection boundary is partly determined by the total mean opacity [70]. Impurities in the hydrogen and helium solar plasma are important. For example iron accounts for approximately a quarter of the solar opacity at the base of the solar convection zone [70]. Using recent photosphere spectral analysis the elemental abundance of iron and other impurity elements has been predicted to be lower by 30 - 50 % compared to earlier assumed values [71, 72]. Helioseismology uses acoustic oscillations to determine the internal structure of the sun [73]. The standard solar models with the revised elemental abundance disagrees with helioseismic observations. It is possible that the opacity of solar materials such as iron must be higher to account for this discrepancy [73].

Producing laboratory plasmas with conditions similar to those found in stellar interiors is difficult. There has been a large reliance on opacity models to simulate opacities under extreme plasma conditions. Recently, Bailey et al [73] used the Sandia Z-pinch facility to produce high density and temperature plasmas ($1.9-2.3$ million Kelvin and $0.7-4.0\times10^{22}$ cm^{-3}) which were similar to conditions found in the solar convection boundary. The experiment measured opacities $50-300\%$ higher than opacity models (OP, SCRAM, OPAS, ATOMIC and SCO-RCG). The investigation in chapter 5 also predicts a factor of 2 increase in iron opacity for plasmas at 20 eV and 0.3 gcm^{-3} (see figure 6.19).

3.4 Conclusion

Local thermodynamic equilibrium can be reached when the collisional processes are dominant compared to the radiative processes. Previous investigations have shown that heating buried layer targets with short pulse lasers similar to those used in chapter 5 can produce high density and temperature plasmas close to LTE conditions [14–17]. The Saha LTE model described in this chapter will be used in chapter 5 to deduce the temperature and density conditions within the iron layer. L-shell emission spectroscopy can be highly complex due to the numerous possible decay paths from the M-shell. Using the collisional-radiative ionisation model described in this chapter the PrismSPECT code will be used in chapter 5 to produce synthetic L-shell spectra of iron.

Chapter 4

Diagnostics and instruments

To measure energy transport in buried layer targets various diagnostics have been used to characterise the high density plasma conditions. X-ray imaging and x-ray spectroscopy have previously been extensively used to study high density plasmas [17, 18, 74–77]. The key instruments used for this thesis include a soft x-ray high resolution grating spectrometer (HRGS) and a probing extreme ultraviolet (EUV) laser. This chapter introduces key aspects of spectroscopic instrumentation such as dispersing elements, filters and detectors. A brief introduction to EUV lasers and their applications is also presented.

4.1 Spectrometers

4.1.1 Dispersive element

To undertake qualitative x-ray spectroscopy, some spectral resolution is required so that for example, spectral lines can be resolved. A spectrometer typically requires an entrance slit, a dispersive element and a detector. Refracting prisms, diffraction gratings and crystals are examples of dispersive elements which spread

the emitted radiation in space as a function of wavelength. Diffraction gratings and crystals can have a higher resolving power and dispersion compared to prisms and are chosen for measuring short wavelength (< 200 nm) emission spectra as the radiation absorption in a refracting prism is high [66]. Diffracting crystals require a crystal lattice plane spacing d_l such that $2d_l$ is greater than the wavelength of the radiation. For soft x-ray and extreme ultra-violet (EUV) radiation at wavelengths > 1 nm, diffraction gratings are usually employed.

Diffraction gratings can be divided into two categories depending on how they are manufactured: ruled or holographic. Ruled gratings mechanically burnish grooves into malleable material with a stylus usually made from diamond [66]. When the interference fringe pattern produced by the overlap of two lasers is exposed upon a photosensitive material holographic grating grooves can be created. The groove profiles for holographic gratings are sinusoidal, but ruled gratings typically have a saw tooth profile.

The general diffraction grating equation is given by,

$$m\lambda = d\,(sin\alpha + sin\beta) \tag{4.1}$$

where m is the diffraction order and d is the groove spacing, α is the incident angle and β is the diffraction angle. The high resolution grating spectrometer (HRGS) used in chapter 5 employed a 2400 lines/mm variable spaced line grating manufactured by Hitachi. The grating is placed at a small grazing incident angle in order to increase the reflectivity [66] of iron L-shell emission radiation. Figure 4.1 shows the layout of the HRGS in relation to the target chamber.

Figure 4.2 shows schematic for a concave grating with equally spaced rulings and some sample wavelength focussed onto a Rowland circle. Placing the concave grating with radius of curvature equal to the Rowland circle diameter on the Rowland

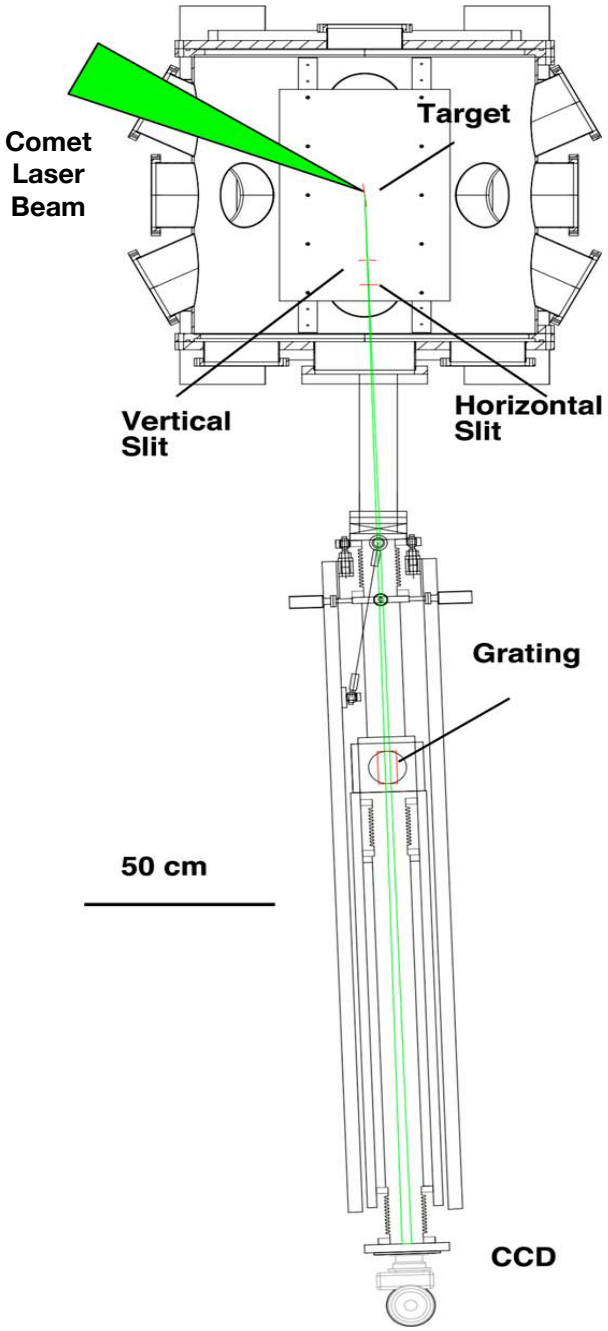

FIGURE 4.1: A detailed schematic of the high resolution grating spectrometer built by Lawrence Livermore National Laboratory. This spectrometer was used to record the L-shell spectral emission of iron buried layers irradiated by the COMET laser. The Hitachi variable line spaced (VLS) grating with 2400 lines/mm and a radius of 44.3 m was used to produce a flat field image onto the liquid nitrogen cooled CCD detector. The slits were removed to increase the exposure onto the grating. This image has been taken from Dunn et al [68]

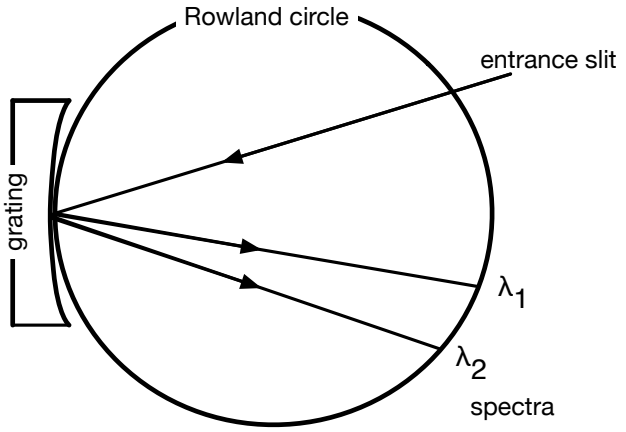

FIGURE 4.2: A Rowland circle spectrograph. The concave equally spaced diffraction grating will disperse all wavelengths onto the Rowland circle and will be free from defocus and primary coma.

circle produces spectra free from defocus and primary coma at all wavelengths [78]. Initially photographic plates were bent along the circular arc of the Rowland circle. A curved detection surface is a problem for flat detectors such as charge coupled devices (CCD's) or streak cameras which cannot conform to the curvature of the Rowland circle. Cornu [79, 80] realised that variations in the groove spacing can modify the curvature of the diffracted wavefront. A uniform variation in groove spacing can change the tangential focus curve of the spectrum such that a flat field focussed image is produced. Such variable line spaced (VLS) gratings have the ability to diffract and focus an image upon a flat field detector.

Diffraction gratings need to also efficiently reflect emission lines onto the detector plane. At very short wavelengths the reflectivity of metal surfaces reduces significantly at normal incidences. However, at glancing angles the reflectivity of EUV and x-rays can be high, so for the EUV wavelength investigated in chapter 5 the spectrometer operated with a grazing-incidence angle of 3.4° into the grating surface.

For EUV and soft x-ray radiation (SXR) the refractive index of the radiation in a metal or semiconductor is smaller than unity because quasi-free conduction band

electrons act in a similar way to free electrons in a plasma. Angles of incidence above the critical angle (θ_c =$\sin^{-1}(n_2/n_1)$) are total internally reflected. When intersecting a surface with higher refractive index n_1 from a lower refractive index n_2 the critical angle for reflection of radiation from a surface, θ_c can be written as,

$$\theta_c = \sqrt{2\delta} \tag{4.2}$$

where

$$\delta = \frac{n_a r_e \lambda^2 f_1^0(\lambda)}{2\pi}. \tag{4.3}$$

Here n_a is the atomic density, r_e is the electron radius, λ is the wavelength and $f_1^0 = \sum_s g_s \left(\frac{\omega^2}{\omega^2+\gamma^2}\right)$ is the real part of the dimensionless scattering form factor. As the atomic density varies slowly in elements the critical angle is mainly proportional to the wavelength and the square-root of the material's atomic number, $\theta_c \propto \lambda\sqrt{Z}$, where the first order f_1^0 is approximated by Z [81]. Due to the large critical angle associated with high Z materials, x-ray optics are often coated with gold, platinum or iridium. A gold Hitachi diffraction grating was used in chapter 5 and was placed at a small grazing angle 3.4° [18].

4.1.2 Calibration of the high resolution grating spectrometer.

The oxygen K-shell spectral lines emitted from thin mylar foils were used to calibrate the dispersion of the HRGS. Figure 4.3 shows a mylar spectrum with several dominant features comprising hydrogen-like and helium-like oxygen lines. Irradiating an iron buried layer targets with the COMET laser also produces two prominent Li-like Fe lines. These oxygen and iron emission lines are well documented in the NIST database [82] and their wavelengths are accurately known

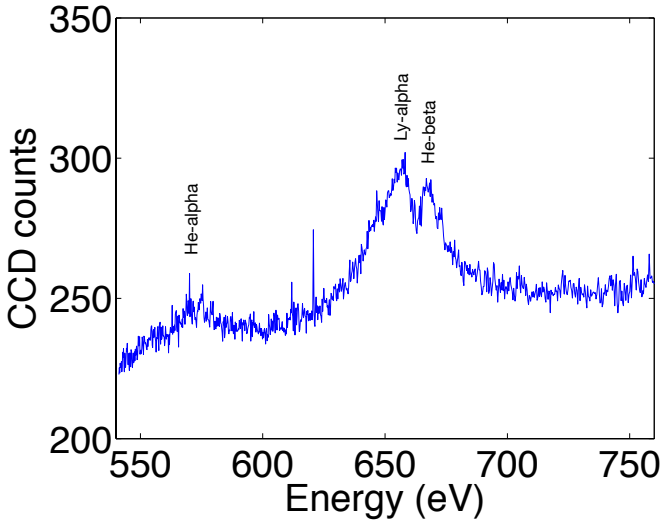

FIGURE 4.3: Calibrated mylar (1.5μm) spectrum produced using the COMET laser ($\sim 10^{17}$ Wcm^{-2}) and recorded with the high resolution grating spectrometer at a shallow viewing angle of 5°.

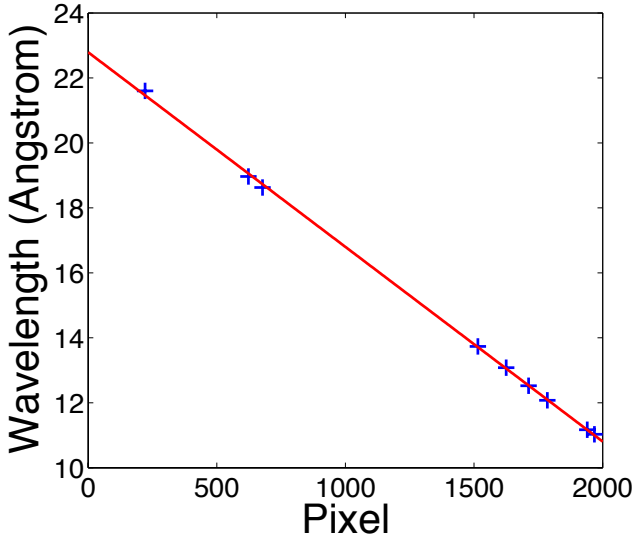

FIGURE 4.4: The linear dispersion relation between wavelength and pixel location with the best fit line shown (red) for the HRGS. The equation of best fit is used to calibrate the wavelength scale.

[83, 84]. Using these key oxygen spectral features a linear dispersion relation between wavelength and pixel location of a CCD detector is found (see figure 4.4).

Grating efficiency measures the power diffracted into a particular direction compared to the power incident on the diffraction grating. A higher grating efficiency

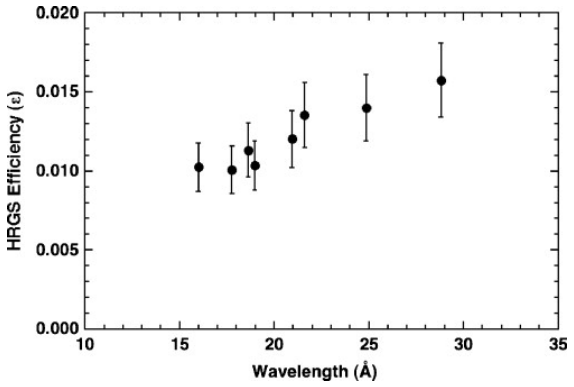

FIGURE 4.5: The high resolution grating spectrometer efficiency is defined as the grating efficiency × quantum detection efficiency. The grating reflectivity is expected to be close to the above values. This image is taken from Magee et al [85]

ensures that weaker line transitions can be detected. The grating efficiency depends on the groove profile and the incident angle and is often shown as an efficiency curve (see figure 4.5). The HRGS can be calibrated by recording the response to a well characterised x-ray source. This was provided by using the SuperEBIT device which produces x-rays from trapped highly charged ions [85]. Neutral CO_2, Kr, Ne and SF_6 were injected and collisionally ionised by the electron beam. Intense magnetic fields $\sim$ 3 T subsequently trap the charged ions [85].

When a high powered laser irradiates a target, the material expands into the vacuum. Exposing the diffraction grating to ablated material over a long period can result in the formation of thin impurity layers on the grating which can reduce the grating reflectivity [85]. The efficiency of the CCD detector can also be reduced by ablation and deposition of target material [86]. This is not expected to be important for the HRGS because the CCD is placed a long distance away from the source. The small aperture ($\simeq$ 10 cm) between the target chamber and the HRGS (see figure 4.1), the shallow spectrometer viewing angle (pointed away from target normal) and the HRGS turbo vacuum pump reduced potential debris that may fall onto the CCD chip and VLS grating.

4.2 Extreme ultra-violet lasers

Short wavelength extreme ultraviolet (EUV) lasers are particularly useful compared to optical lasers for probing warm dense matter because the critical density is much higher at shorter wavelengths ($n_c \propto 1/\lambda^2$). Inverse bremsstrahlung for optical light also becomes significantly high for electron densities greater than 10^{20} Wcm^{-2}. Other difficulties associated with use of optical probes include adverse refraction effects, which can affect spatial resolution and data interpretation [74].

Previously, interferometry using soft x-ray lasers probed the structure of expanding plasmas [87]. Transmission measurements using x-ray lasers have also provided information on opacity [88] and ablation rates. In Chapter 5 an extreme ultra-violet (EUV) x-ray laser has been used as a back-lighter to diagnose energy transport in buried iron layer targets.

4.2.1 General features of extreme ultra-violet lasers

Optical lasers typically use solid cavities made from Nd:YAG or Ti:sapphire as the gain medium. However, in order to produce intense x-ray lasing the gain medium must sustain high temperature ($\sim$ 100 eV) and density ($\sim 10^{20}$ cm^{-3}) conditions where large populations of upper level excited states can exist. These conditions required that the lasing medium is a plasma. The ratio between the Einstein stimulated and spontaneous emission rates scales with wavelength as,

$$\frac{B_{ji}}{A_{ji}} = \frac{\lambda^3}{8\pi\hbar} \tag{4.4}$$

where A_{ji} and B_{ji} are the Einstein spontaneous and stimulated coefficients respectively. Shorter wavelength lasing demands more rapid and intense pumping

schemes [89] as the lifetime of the excited upper levels typically lasts $\sim$ ps [81], short pulsed lasers are used to deliver the energy. A short laser pulse $\simeq$ 3 ps was used to produce lasing at 13.9 nm at the LASERIX facility, Paris for the work of this thesis.

Laser produced plasmas acting as the gain medium for soft x-ray lasers were first demonstrated by Matthews et al [90]. X-ray lasers initially were produced using a single pulse which ionised the material and also pumped the gain medium. However, as the ionisation rate is slower ($\sim$ 100 ps) than the population inversion lifetime ($\sim$ 10 ps) [91] the laser energy is wasted in heating the plasma rather than creating population inversion. Using a prepulse can ionise the lasent to the required Ni-like or Ne-like configuration and after a time delay a second short intense laser pulse cause a spike in collisional-excitation which subsequently produces a transient population inversion.

Optical lasers typically use a bright flash lamp to create population inversion. However, due to the absence of a bright x-ray source which can photo-pump, the high density and temperature conditions in the plasma facilitate collisions between free-electrons and ions with large collisional-excitation rates [91]. Collisionally pumped x-ray lasers has been demonstrated in this way [90, 92–94].

At high temperatures, low Z materials are easily stripped of their electrons, hence the number of bound-bound transitions required for x-ray lasing is negligible. High-Z materials such as silver and samarium are preferred as the lasent material because they ionise to Ne-like and Ni-like ion configurations, which are stable over a broad range of temperatures and densities found in laser-produced plasmas [91, 95]. As a result the total energy output of the x-ray laser is higher because of the larger relative abundance of lasing ions in the plasma. Figure 4.6 shows the population inversion schemes for Ne-like ions and Ni-like ions.

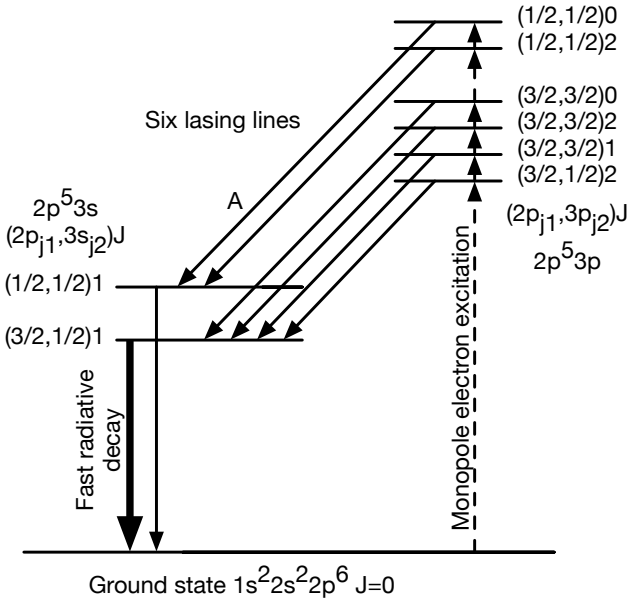

(a)

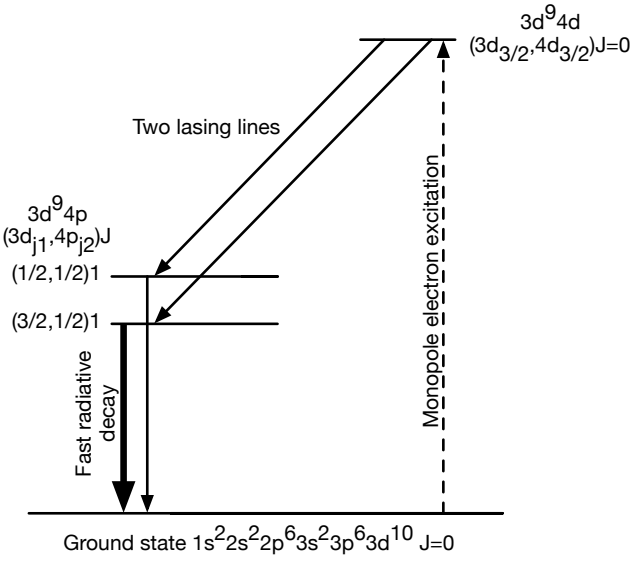

(b)

FIGURE 4.6: Grotrian diagram for (a) Ne-like and (b) Ni-like ion configurations.

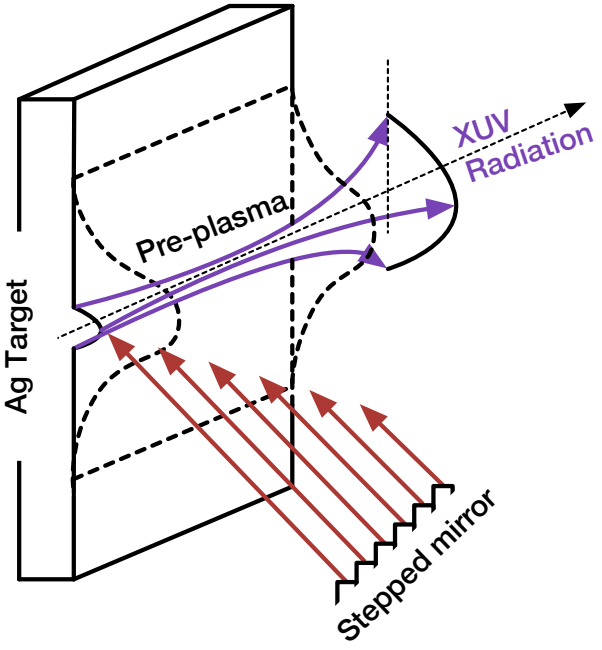

FIGURE 4.7: Line focus x-ray laser

Lasing occurs between excited sub-shells $2p^5 3p \rightarrow 2p^5 3s$ (neon-like) or $3d^9 4d \rightarrow 3d^9 4p$ (nickel-like) [96]. The abundance of multi-stable ions such as Ne-like and Ni-like ions is relatively high over a wide range of parameters compared to ions with no closed outer shells. This is beneficial for x-ray laser systems because a gain medium with a larger population of lasing ions will produce a higher intensity x-ray laser [81].

The ionisation, density profile and absorption coefficient of the lasent material are factors which can be optimised to efficiently produce an x-ray laser. A number of improvements can be made such as the use of a prepulse, which not only ionises the material but also creates density gradients shallow enough so that x-rays amplify across the entire gain region without significant refraction [95]. Implementation of a prepulse has reduced the pump energy to as low as 1 J [97–99]. Recalling chapter 2 we find that high-Z materials have the added advantage that they absorb the incident laser energy more efficiently via inverse bremsstrahlung compared to low-Z materials. The delay between the prepulse and mainpulse determines the final

density distribution and the ionisation. By using a two colour pumping scheme, a frequency doubled mainpulse can increase the critical density fourfold, therefore creating a larger gain region.

Optical lasers are amplified by passing the laser pulse through the gain medium several times. However due to rapid cooling, the short lived plasma gain medium only allows amplification through a single pass. The propagation time for an EUV beam in the plasma is ~ 33 ps/cm whereas the population inversion time is ~ 10 ps [99]. A travelling wave can further enhance x-ray emission by synchronising the population inversion and propagation timescales. This is achieved by tilting the incident laser wavefront using a stepped mirror. Diffraction gratings optics have also been used to create a further shear in the wavefront [99].

4.2.2 Properties of the EUV LASERIX laser

For back-lighter experiments, the probing laser beam must be brighter than the plasma self emission. Collisionally pumped EUV lasers can achieve high peak brilliance $\sim 10^{24}$ photons s^{-1} mm^{-2} $mrad^{-2}$ compared to other table top configurations[1] at saturated conditions [91]. The EUV laser pulse at the LASERIX facility, Paris is produced in two steps. First, a long $\simeq 9$ ns prepulse laser is line focussed onto a silver target at normal incidence, producing an expanding preplasma which ionises the silver to the Ni-like ionisation level. After a delay of ~ 5 ns a frequency doubled short pulsed $\simeq 3$ ps laser irradiates the preformed plasma at a grazing incident angle of 20°. The tilted wavefront of the pump laser creates a travelling which initiates amplification. Silver was chosen as the lasent material because the lasing $4d-4p$ line at 89 eV is ideally placed within the sharp reflection peak for Mo:Si multi-layered mirrors (see figure 4.9).

[1] Solid HHG, gas HHG etc.

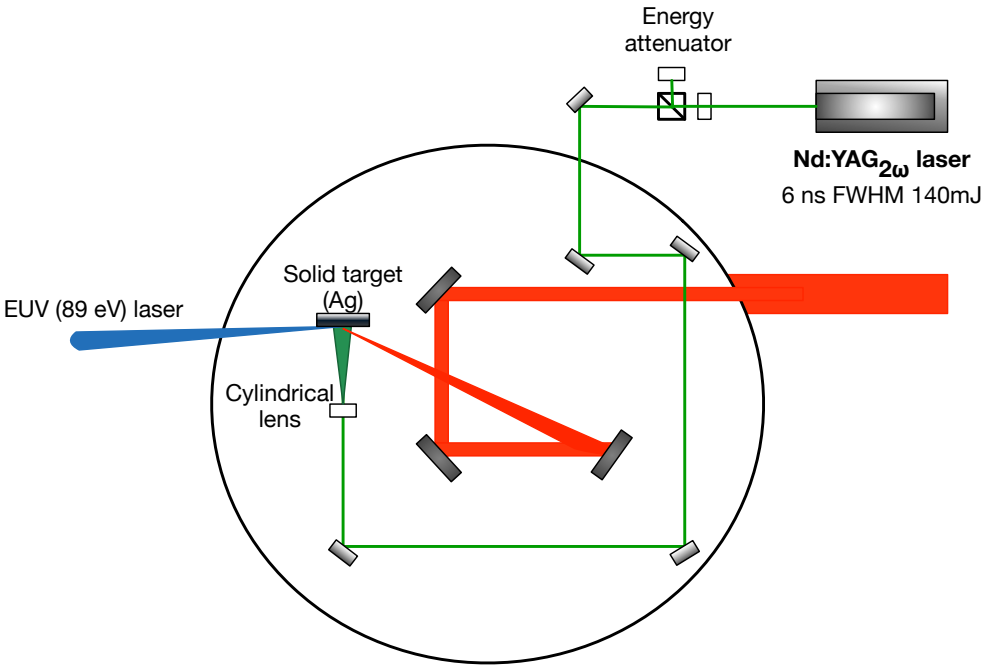

FIGURE 4.8: Experimental setup showing the two pulse laser (GRIP) scheme to generate the extreme ultraviolet laser probing pulse.

4.2.3 EUV optics

Multilayer mirrors

A multi-layered mirror is made by coating a substrate with alternating layers of differing refractive index. The contrasting high and low refractive index of the two materials maximises the reflection of radiation at the boundaries between the layers [81]. Single layered optics typically have poor reflectivity except at glancing incidence angles. However, weak reflections from multiple layers can constructively interfere and permit large reflectivity of EUV wavelengths at normal incidences. Multi-layer x-ray optics are usually optimised for a specific wavelength [66]. The experimental investigation in chapter 6 used a Mo-Si multi-layered mirror to efficiently reflect (reflection $\sim$ 75%) the 89 eV EUV photons (see figure 4.9). The poor reflectivity outside the narrow bandwidth peak (see figure 4.9) ensures that the CCD does not detect the x-ray self-emission from the probed plasma. The CXRO database was used to calculate the reflectivity of the Mo-Si multilayer

mirror by using the Fresnel equations and the analytic formula given by Kohn et al [100] (see figure 4.9).

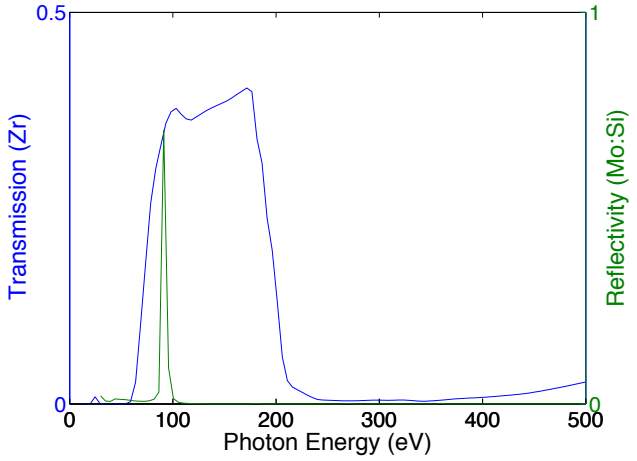

FIGURE 4.9: The reflectivity of a Molybdenum-Silicon multi-layered mirror with an angle of incidence of 90° is shown (green) for a range of photon energies. The multi-layered mirror has a sharp peak reflectivity is $\simeq 0.7$ for photon energies $\simeq 89eV$. The transmission as a function of photon energy (blue) is shown for 0.3μm of zirconium [101]. The low filter transmission within the 250 - 400 photon energy range and the poor reflectivity of the multi-layered mirror at these energies can effectively filter out the iron self emission that falls onto the CCD detector.

4.3 Detectors

4.3.1 Charge coupled device (CCD) detectors

The development of the charge coupled device (CCD) in 1969 has paved the way to numerous applications [102]. A CCD camera detects photons when they excite electrons from the valence to the conduction band in a silicon wafer. The photo-excited free electrons are localised into potential wells (pixels) using external electrodes. The number of electrons are sequentially recorded by moving them through a charge amplifier. Scientific CCD sensors often operate at different gain levels in the charge amplifier, but they produce a digital count proportional to the

number of electrons. The number of counts is thus proportional to the number of photons that entered the pixel. Spectral emission of L-shell plasmas (see chapter 5) and the transmission of the EUV laser both were recorded using CCD cameras (see chapter 6).

The quantum efficiency, Q_E of a CCD detector is the number of free electrons produced per incident photon. The Q_E was taken into consideration when calculating the emissivity of the iron plasma at the source using equation 5.3. The energy required to produce an electron-hole pair in silicon is 3.6 eV [103].

Blooming of the CCD signal occurs when electrons overfill their designated potential wells and overflow into neighbouring wells therefore producing saturated pixels. This blooming effect can reduce image resolution. To counter this effect filters are used to reduce the exposure onto the CCD. For chapter 6 a zirconium filter of thickness 0.3 μm was placed infront of the CCD chip. The transmission of radiation through the Zr filter is shown in figure 4.9.

For chapter 5 no filters or slits were used because the L-shell emission was considerably weaker due largely to the shallow angle that the CCD was placed with respect to the source (see figure 5.1).

Thermal heat can also liberate an electron from the CCD valence band to the conduction band. This phenomena causes a dark current (present without radiation) and is heavily dependent on the temperature. As a result a liquid nitrogen cooled CCD camera operating at -110 °C was used in chapter 5 to minimise the dark count. Additional effects such as exposure to cosmic rays can also effect the CCD background radiation signal. The background count was measured by placing the camera behind the shutter to prevent any light leaking onto the sensor and a background image was recorded. This background image was then subtracted from CCD images recording the spectra.

4.4 Codes

Since the beginning of ICF research, numerical simulations have played an important part in the study of high energy density plasmas (HEDP) [2]. HYADES [19], PrismSPECT [20], EHYBRID [21], Prism opacity and equation of state (PROPACEOS) [20], IMP [62] and TOPS [104] codes have been used to simulate a wide range of problems related to HEDP for this thesis. The high complexity, non-linearity and inter-dependancy of the many processes occurring in HEDP make an analytic approach difficult. Simulations with small time steps can predict the evolution of variables and therefore build a picture of the complex laser produced plasma.

The 1D hydrodynamic HYADES code simulated plasma conditions such as temperature, density and ionisation. The collisional-radiative code, PrismSPECT was used to simulate the L-shell emission spectra from buried iron layers. The hydrodynamic-atomic code EHYBRID simulated the delay in x-ray generation from the pumping laser. The following sections give an overview of each code.

4.4.1 Hydrodynamic fluid code HYADES

High density laser produced plasmas can be simulated by particle in cell (PIC) and fluid codes. Solving for the plasma temperature and density using mass, momentum and energy conservation equations, the fluid dynamic approach can accurately model the macroscopic evolution of laser produced plasmas.

HYADES is a one-dimensional Lagrangian radiation hydrodynamic fluid code. A Lagrangian coordinate system maintains constant mass in each cell. The code computes particle properties within each cell following their motion in time. Eulerian codes calculate fluid properties as particles pass through a fixed mesh grid. At

early times the laser produced density profile rapidly changes, therefore evolving Lagrangian grids are preferred. In HYADES the position and velocity variables are defined at mesh points and the density and pressure variables are defined at zone centres [19]. The HYADES simulations shown in chapter 4 and 5 used a planar mesh geometry for the buried layer target.

The HYADES code incorporates a three fluid description for electron, ions and the radiation field with each having its own temperature. Each fluid is assumed to be in local equilibrium and their velocities are calculated using Maxwell-Boltzmann statistics. The radiation field can be simulated using a Planckian distribution. However, a more accurate method where multi-group diffusion is employed enables departures from the Plankian distribution to be simulated. HYADES uses a flux limited diffusion approximation to describe the thermal energy transport for electrons and ions.

An equation of state for a material describes the thermodynamic properties of a material by interlinking the density, pressure, temperature and internal energy [30]. HYADES incorporates the equation of state and opacity from the Sesame database [105]. HYADES can run with different ionisation models including Saha, Thomas-Fermi, full ionisation, average atom LTE and NLTE. This thesis used LTE and NLTE average atom ionisation models. In NLTE, rate equations are used to evaluate the ionisation in each cell.

In chapter 5 HYADES was used to simulate the buried iron layer temperature and density conditions. The mesh grid was split into three regions, each describing one of the layers in the target. The simulated temperature and density conditions were post-processed into the collisional-radiative code PrismSPECT to simulate the L-shell iron emission spectra. Chapter 6 used the HYADES mass densities and electron temperature with IMP opacities to simulate EUV transmission through the target.

The HYADES code is designed to simulate laser-plasma interactions at moderate laser intensities $\sim 10^{14}$ Wcm^{-2} where hot electron heating is not significant. At higher laser irradiances ($> 10^{14}$ Wcm^{-2}) hot electron heating can influence many laser-plasma interactions and therefore make codes such as HYADES unstable. To accurately simulate hot electrons PIC codes such as EPOCH can be used, however, due to the nature of PIC codes these simulations can not accurately describe the macroscopic behaviour of laser produced plasma. Although the HYADES code cannot directly simulate hot electrons the energy distributed per unit mass throughout the target due to hot electrons can be estimated using Key et al scaling, which predicts the laser-hot electron conversion efficiency (see figure 2.9).

As flux inhibition is caused by a range of different factors[2] using flux limiters in numerical simulations can be a crude method to simulate the unphysical large heat fluxes at steep thermal fronts. The correct flux limiter value can be inferred by comparison with experimental data or by comparison between Fokker-Planck simulations. In chapter 6 a range of flux limiter values are used to simulate the temporal change in transmission within the buried iron layer. Subsequent comparison with the experimentally recorded iron transmission can provide an estimate of the flux limiter value (see figure 6.7). Although the iron transmission is dependent on energy transport processes such radiation transport, hot electron heating and thermal conduction. It is found that hot electron heating is negligible (see figure 6.7). To simulate the radiation transport multi-group diffusion is used in the HYADES code. Varying the number of multi groups in the code did not greatly affect the iron transmission (see figure 6.11). Therefore, the transmission can be used to infer the thermal flux limiter value.

[2]self generated magnetic fields, ion acoustic turbulence etc.

4.4.2 Collisional-radiative codes

To simulate and reproduce experimentally recorded spectra, collisional-radiative (CR) codes are used to simulate the quantum state populations for a range of plasma conditions. The emissivity is subsequently calculated using the simulated population distribution and taking into account plasma opacity and line broadening effects.

Collisional radiative (CR) codes have also been used in radiation-hydrodynamics models [33] to compute plasma parameters such as internal energy, partition function and equation of state. In this thesis a collisional-radiative code, PrismSPECT was used to model synthetic spectral data with input densities and temperatures simulated by HYADES code. By comparing experimentally recorded spectra and simulated spectra the plasma conditions can be inferred [18].

CR modelling of K-shell spectroscopy usually involves one or two bound electrons. In order to simulate L-shell spectroscopy a more complex atomic model is required due to the larger number of possible transitions (see equation 3.13). However, taking into account every possible atomic transition is computationally expensive. To overcome this, the atomic structure of atoms is often simplified using average-atom, unresolved transition arrays (UTA), super-configurations and detailed configuration accounting (DCA) techniques.

For low Z elements with a few bound electrons, the line spectra is relatively simple. However, high Z materials such as iron have many possible bound-bound transitions which can lead to spectra with many closely packed spectral lines. It is possible that the number of bound-bound transitions is so great that the line width of each spectral line is greater than the spacing between each line [59]. As a result the line spectra becomes an unresolved transition array (UTA) [106]. The shape of the UTA can be modelled using band structures which averages the total

intensity and collectively describes a number of lines, therefore simplifying the atomic modelling. Detailed configuration accounting (DCA) includes atomic data upto LS coupling, but does not include term splitting.

A DCA atomic model was used in PrismSPECT to simulate the L-shell emission spectra as shown in figure 5.5. Average atom models calculate shell populations and usually assume equilibrium population within a shell. The number of electrons calculated in the shells in an 'average' atom determines the degree of ionisation.

PrismSPECT

PrismSPECT is a collisional-radiative code made by Prism computational sciences Inc. In chapter 5 PrismSPECT was used as a post-processing code where the plasma hydrodynamics were incorporated from HYADES. The ATBASE atomic code provides PrismSPECT with atomic data including photo-ionisation cross sections, oscillator strengths, collisional ionisation and excitation cross sections, and atomic energy levels for a range of different materials. The atomic model can simulate more than one material by specifying the fraction of different elements. This feature was used to estimate the level of iron oxide present in the iron layer. Previous collisional radiative codes such as FLYCHK used only screened hydrogenic n-levels. To simulate L-shell spectra, PrismSPECT uses a more accurate detailed account configurations method. The simulated spectra shown in figure 5.5 used $\sim$ 30000 line transitions. Time-dependent rate equations were calculated using the time varied temperature and density conditions from HYADES. The ionisation dynamics also included continuum lowering effects. The PrismSPECT code computes atomic populations under LTE using Saha-Boltzmann equations and for non-LTE plasma populations time-dependent and steady state equations can be used. To generate the bound-free, bound-bound and free-free synthetic

spectra, PrismPLOT computes the emissivity and opacity of the plasma as a function of frequency. The PrismPLOT spectral modelling takes into account various line broadening effects, such as Stark broadening. PrismSPECT incorporates hot electron populations by assuming a value for the hot electron temperature. For chapter 5 Begs scaling law provided an estimate of the hot electron temperature whereas in chapter 6 the temperature detected by the diode array was used in the PrismSPECT calculations.

EHYBRID

EHYBRID is a Lagrangian hydrodynamic code which aims to model detailed atomic interactions and hydrodynamics in x-ray lasers. EHYBRID uses a planar Lagrangian mesh and the fluid is modelled in the direction parallel to the driving laser. To determine the time dependent ionisation state and the abundance of Ni-like or Ne-like ions a collisional-radiative model is also used. Collisional excitation, de-excitation, radiative decay and many other atomic processes are included in the rate equation. A detailed atomic model is used, for example the Ni-like ionisation stage is modelled with 272 excited levels. EHYBRID implements a Chart-D equation of state (EOS) model.

The data simulated from EHYBRID can be postprocessed using RAYTRACE to calculate the amplified spontaneous emission along the ray paths including refraction effects, therefore calculating the total output x-ray laser intensity. The refractive index is continuous and the gradient is constant within a given RAYTRACE element. Each ray has an assumed parabolic path and the path is interpolated between each element. Saturation of a ray is included by a switch to linear amplification at a set gain length product value.

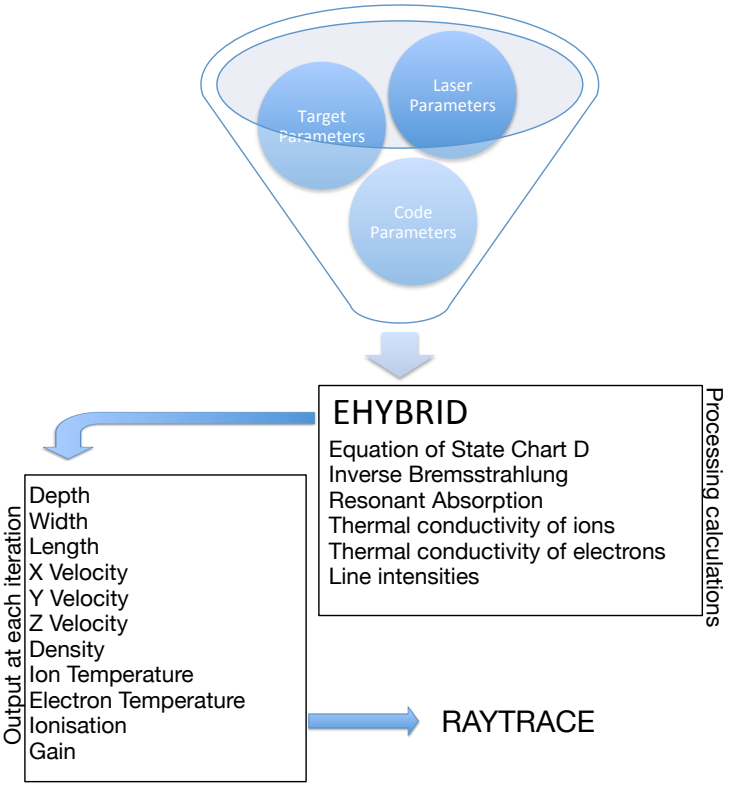

FIGURE 4.10: Flow diagram showing how the EHYBRID code operates.

The EHYBRID hydrodynamic code was used to simulate the delay in x-ray generation for the silver EUV laser at the LASERIX facility. The gain-length product was calculated using EHYBRID and was then post-processed into the RAYTRACE code which calculated the output x-ray laser intensity. The delay in x-ray generation is simulated from the time of the main pulse.

When the flux limiter is set to 0.01 the output intensity is $\sim 10^7$ Wcm^{-2} and the x-ray pulse delayed by 100 ps from the peak of the pumping laser pulse. Increasing the flux limiter to 0.06 reduces the x-ray generation delay to 40 ps and increases the output intensity to $\sim \times 10^{10}$Wcm^{-2}. Although increasing the flux limiter from 0.06 to 0.1 does not increase the x-ray laser output intensity or the delay, the x-ray laser pulse duration reduces to 10 ps. A flux limiter of 0.15 simulates a x-ray generation delay of 35 ps, x-ray laser intensity $\sim \times 10^{11}$Wcm^{-2} and a pulse duration of 3 ps. Therefore, when the flux limited thermal conductivity is increased the x-ray laser

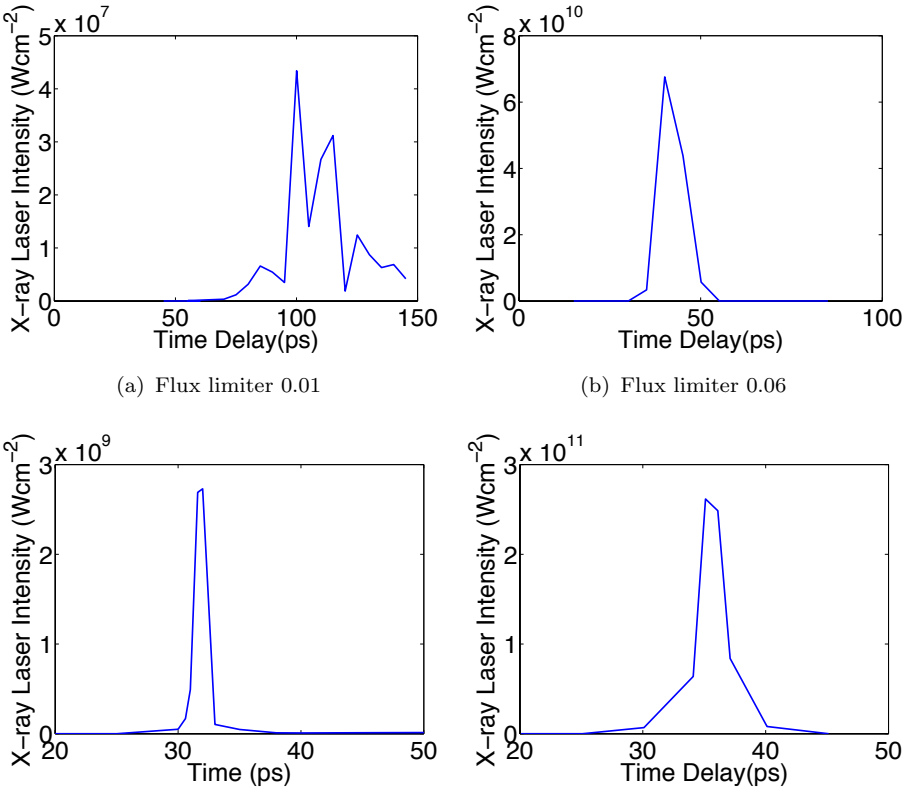

(a) Flux limiter 0.01

(b) Flux limiter 0.06

(c) Flux limiter 0.1

(d) Flux limiter 0.15

FIGURE 4.11: The EHYBRID simulations were post-processed using RAY-TRACE code to calculate the output x-ray laser intensity as a function of time. Simulations shows the output x-ray laser intensity for a range of flux limiter values (a) 0.01, (b) 0.06, (c) 0.1 and (d) 0.15.

pulse has a shorter delay, shorter pulse duration and increased intensity output.

Due to the nature of 1D codes, EHYBRID cannot simulate the affect of lateral energy transport, and a large short temporal spike in electron temperatures $\sim 10^4$ eV is simulated (see figure 4.12). Higher flux limiter values do not increase the peak electron temperatures but do predict faster cooling rates within the heated silver target.

The gain length product is simulated for three characteristic silver x-ray lines: 131 Å, 139 Å and 144 Å. EHYBRID predicts that under the simulated conditions the 139 Å x-ray line is dominant.

The simulated x-ray laser pulse for the condition of the EUV laser used in chapter

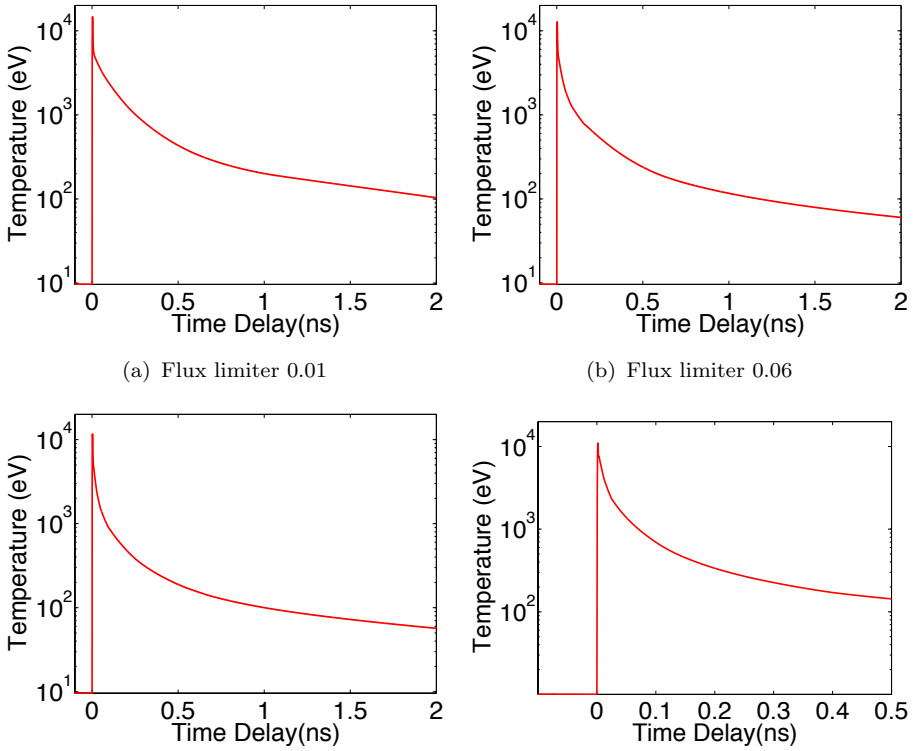

(a) Flux limiter 0.01

(b) Flux limiter 0.06

(c) Flux limiter 0.1

(d) Flux limiter 0.15

FIGURE 4.12: Simulated electron temperatures as a function of time with flux limiter values set to (a) 0.01, (b)0.06, (c) 0.1 and (d) 0.15

6 predicts a FWHM duration 3 ps comparable to the incident infra-red laser pump pulse duration.

4.4.3 Opacity codes

The PROPACEOS, IMP and TOPS codes have been used in this thesis to simulate opacities over a wide a range of plasma temperature and densities. The following section introduces these opacity codes which were used in chapter 6 to simulate the radiation absorption and transmission through buried iron layer targets. The TOPS code was used in chapter 5 to simulate the transmission of the rearside plastic layer (figure 5.8).

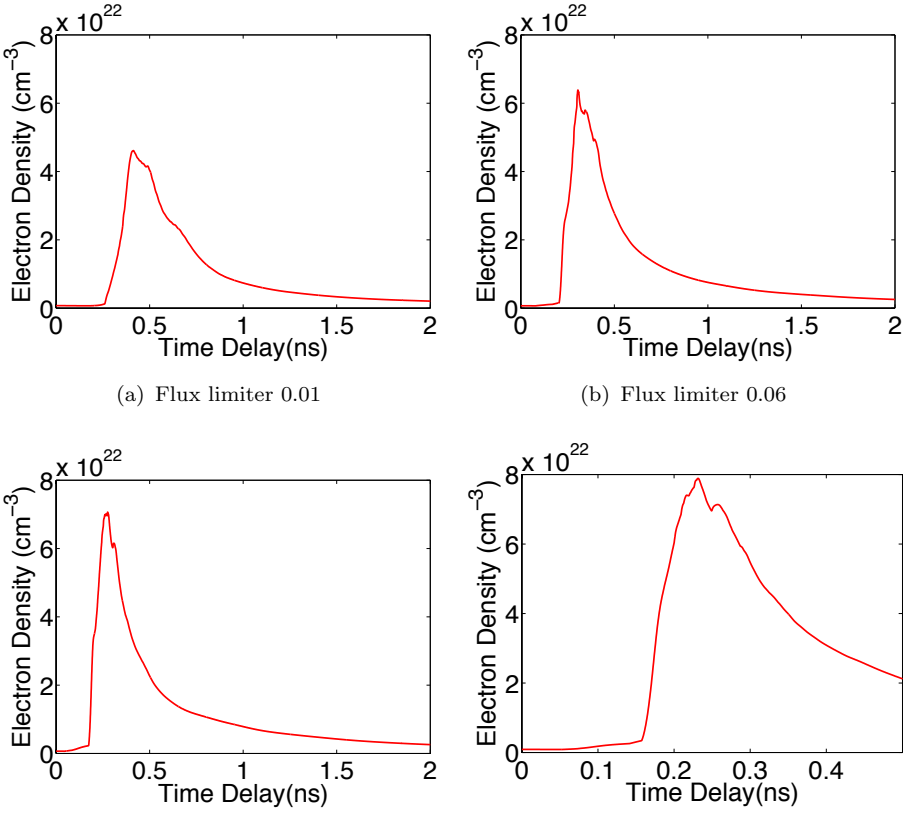

(a) Flux limiter 0.01

(b) Flux limiter 0.06

(c) Flux limiter 0.1

(d) Flux limiter 0.15

FIGURE 4.13: Simulated electron density as a function of time with flux limiter values set to (a) 0.01, (b)0.06, (c) 0.1 and (d) 0.15

PROPACEOS

The PROPACEOS (Prism Opacity and Equation of State) was produced by Prism Computational Sciences, Inc and is part of a cohort of codes[3] which are tailored to simulating laser-plasma interactions. The code can generate equation of state (EOS) and multi-frequency opacity data for a grid of temperature and density plasma conditions for either a single element of a mixture. Boltzmann statistics and the Saha equation are used to compute EOS and opacity for LTE plasmas, whereas steady state solutions to rate equations are used for NLTE plasmas. PROPACEOS can calculate Planck absorption, Planck emission and Rosseland mean group opacities (i.e frequency binned). For non-LTE plasmas the Planck absorption opacity no longer equates to the Planck emission opacity due to the

[3]PrismSPECT, HELIOS, Spect3D, VisRad, Atomic Data, PROPACEOS and PrismPLOT.

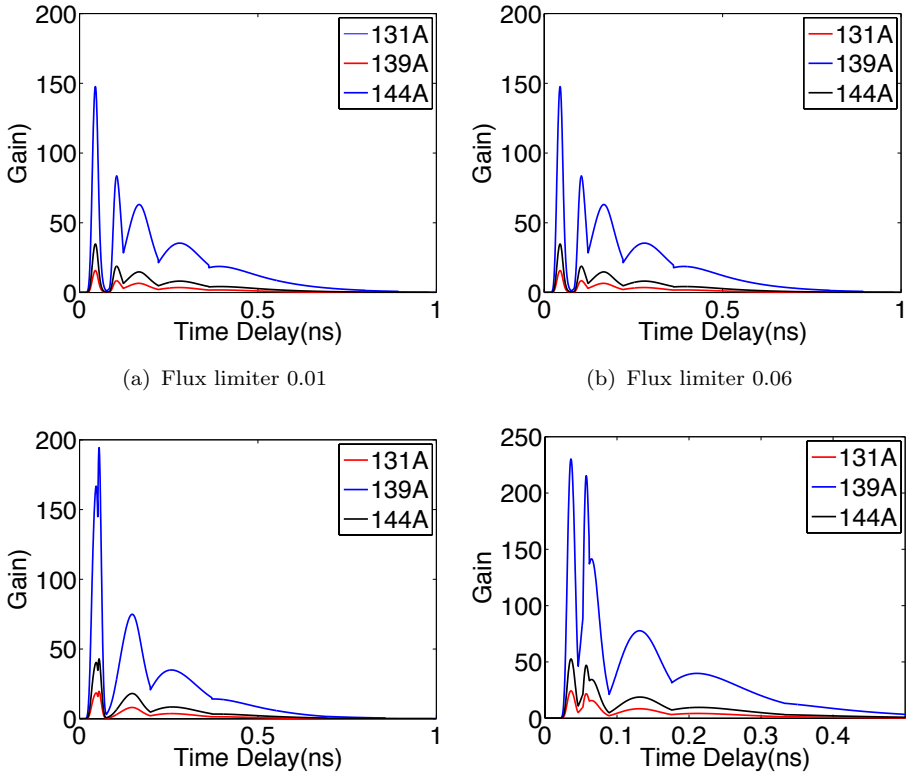

(a) Flux limiter 0.01

(b) Flux limiter 0.06

(c) Flux limiter 0.1

(d) Flux limiter 0.15

FIGURE 4.14: Gain length product as a function of time for x-ray lines 131Å, 139Åand 144Å.

Kirchoff's relation. Figure 4.15 shows the opacity of iron for 89 eV EUV photons at a range of temperature and density values.

The PROPACEOS code was used in chapter 6 to simulate the radiation absorption and the transmission of the iron layer at a range of photon energies, temperatures and densities.

TOPS

The Los Alamos opacity database encompasses the original astrophysical opacity library [107] and the improved light element detailed configuration opacity (LEDCOP) codes [108]. The TOPS opacity code which was produced by the Los Alamos group allows access to these opacities online [104]. The code can be used to find group mean opacities (Rosseland or Planck) for a range of temperature, density

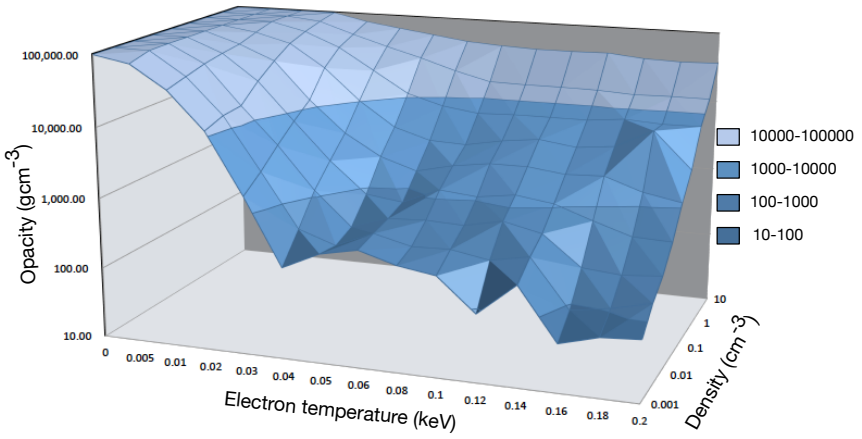

FIGURE 4.15: PROPACEOS opacity look-up table for iron at 89 eV photon radiation.

and frequencies. The astrophysical opacity library focusses on stellar calculations and contains tables for elements upto iron [5]. LEDCOP uses a Hartree-Fock code to simulate detailed LS terms and average configuration terms to calculate opacities for elements $Z < 31$. LTE conditions are assumed and only radiative processes are included. The equation of state (EOS) is based upon the Saha equation. The line profiles for bound-bound transitions are simulated by using Voigt, Gaussian (Doppler) and Lorentzian functions .

IMP

The ionised material package (IMP) code calculates radiative opacity for open L and M shell high-power laser produced plasmas in local thermodynamic equilibrium (LTE). Detailed configuration accounting was used in an open shell for line and photoelectric absorption. Term-splitting effects are also included by using an unresolved transition array (UTA). The opacity due to satellite lines is taken into account by using a statistical methods. The Thomas-Fermi model is used to model the ionic potentials. A Gaussian profile for the distribution of transitions

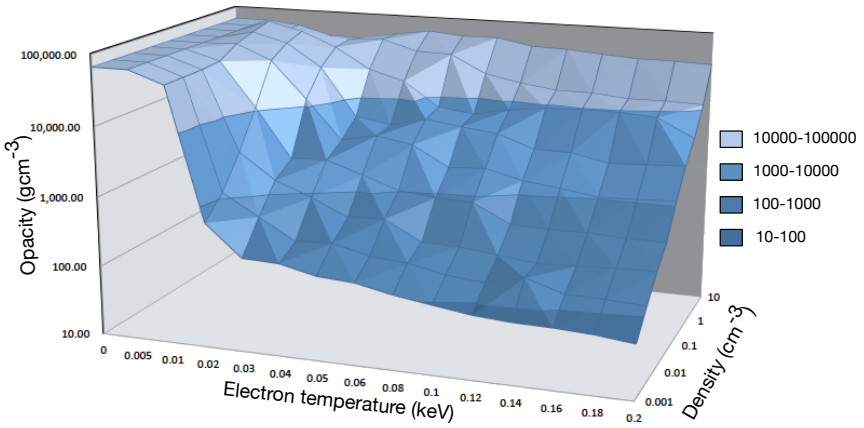

FIGURE 4.16: IMP opacity look-up table for iron at 89 eV photon radiation.

is assumed by the IMP code. Figure 4.16 shows the opacity look-up table for iron at 89 eV photon energy for a wide range of density and temperature values.

Due to the averaging nature of many opacity codes resonance and forbidden transitions $\Delta n = 0$ are often poorly modelled. Chapter 6 highlights the importance of including such transitions as they can significantly increase the opacity particularly within the 70 - 90 eV photon range.

4.5 Conclusion

This chapter has described diagnostics, instruments and simulation (HYADES, PrismSPECT, EHYBRID, PROPACEOS, IMP and TOPS) codes which were used in this thesis to investigate energy transport in high density laser produced plasmas.

A description of the high resolution grating spectrometer (HRGS) which recorded L-shell iron emission in chapter 5 is presented in this chapter. The HRGS was calibrated using oxygen emission lines from laser irradiated mylar targets. General features of the extreme ultraviolet (EUV) laser that was used in chapter 6 is also described in this chapter. The collisional-radiative EHYBRID code was used to

simulate the LASERIX EUV laser generation delay ($\simeq$ 35 ps) and the FWHM pulse duration ($\simeq$ 3 ps). An overview of opacity codes (IMP, PROPACEOS and TOPS) which were used in chapter 6 are also presented here.

Chapter 5

Investigating energy transport using emission spectroscopy from buried iron layered targets.

Uniform high density plasmas of different materials with properties relevant to the interior of stars and to inertial fusion can be created by laser irradiation of targets containing a buried layer of the material. Buried layer targets also enable the diagnosis of hot and thermal electron, x-ray and ion heating of targets. In this chapter, an experiment where L-emission spectroscopy from an iron layer (thickness 77 nm) encased in an otherwise plastic target (of thickness 240 nm − 1.36 μm on the laser side) is irradiated by 0.53 μm wavelength, 2 ps duration laser pulses at irradiances of $10^{17}-10^{18}$ Wcm^{-2} is described. The spectrometer is placed at a shallow viewing angle of 5° to ensure that the source size is small, therefore reducing the effect of source broadening. The relative iron L-emission from Li-like Fe XXIV to Ne-like Fe XVII is used to diagnose the plasma conditions of temperature and density in the iron layer. As the upper quantum states of the L-emission lines are in local thermodynamic equilibrium (LTE), line intensity ratios

depend on both electron temperature and density, which enables the simultaneous measurement of both electron temperature and density by considering several line intensity ratios. Energy transport mechanisms including hot electron heating and thermal conduction have been deduced from the electron temperature and density measurements.

5.1 Introduction

Experiments using high power lasers focussed onto solid targets enable an understanding of some of the properties of the high density plasmas found in stars and in inertial fusion. Targets with a buried layer of a signature material have been used to measure plasma conditions of the buried material at densities above solid using shock wave compression [11, 17]. High energy density plasmas created using buried layer targets can act as sensitive indicators of energy transport into the targets [10, 75] with particular relevance to fast igniter fusion where hot electrons from laser irradiation locally heat partially compressed deuterium-tritium fuel causing fusion ignition [109]. It is important to be able to diagnose plasma conditions in buried layer targets.

Time-resolved measurements of buried layer emission with picosecond resolution before penetration of a refraction wave explodes the target enable the diagnosis of the plasma conditions and properties. However, often time-integrated spectral measurements are sufficient as radiation emission is dominated by the peak temperature, peak density conditions achieved before plasma expansion [110]. Experiments measuring emission from buried layer laser-plasma targets have been used to determine plasma opacities at high density and temperature as the emissivity of the plasma is directly related to the opacity for high density plasmas in local thermodynamic equilibrium (LTE) [13, 16]. The plasma conditions in the

buried layer of the target are also often deduced spectroscopically using line intensity ratios and the slope of continuum emission to measure temperatures and spectral line widths to measure densities [111].

The relative ease of measuring and identifying K-emission from low to medium atomic number elements has resulted in the widespread use of K-alpha radiation for elements from aluminium to iron for the diagnosis of the conditions in the buried layer targets [36, 112]. Thermal emission from hot plasma results in H- to Li-like resonance lines and dielectronic satellites, while at lower temperatures the emitted radiation comprises photons close to the solid K-alpha photon energy. L-shell emission from laser-plasmas results in significantly more complex spectra involving many excited quantum states. Calculating the populations of the quantum states involves the evaluation of energies and radiative transition probabilities for many states and transitions plus significant collisional-radiative population evaluations. Consequently, even comprehensive spectral calculations often fail to fully describe observed spectra because of missing spectral line transitions [73].

The heating of buried layer targets can arise from thermal electron transport, hot electrons and radiation. These heating mechanisms can combine non-linearly making independent simulations without experimental benchmarking unreliable. Principal uncertainties resolve around the value of flux-limited thermal conduction [113] and target heating by hot electrons.

In this chapter, it is demonstrated that it is possible to improve the accuracy of the determination of the plasma conditions in buried layer targets by considering several bright L-emission lines provided the lines are individually identified (not broadened into a quasi-continuum) and the plasma ionisation is in LTE. By using the time-integrated intensity ratios of lines in different adjacent ionisations in LTE, we have measured densities and temperatures in a signature layer of a laser-irradiated target as the target material heats and explodes.

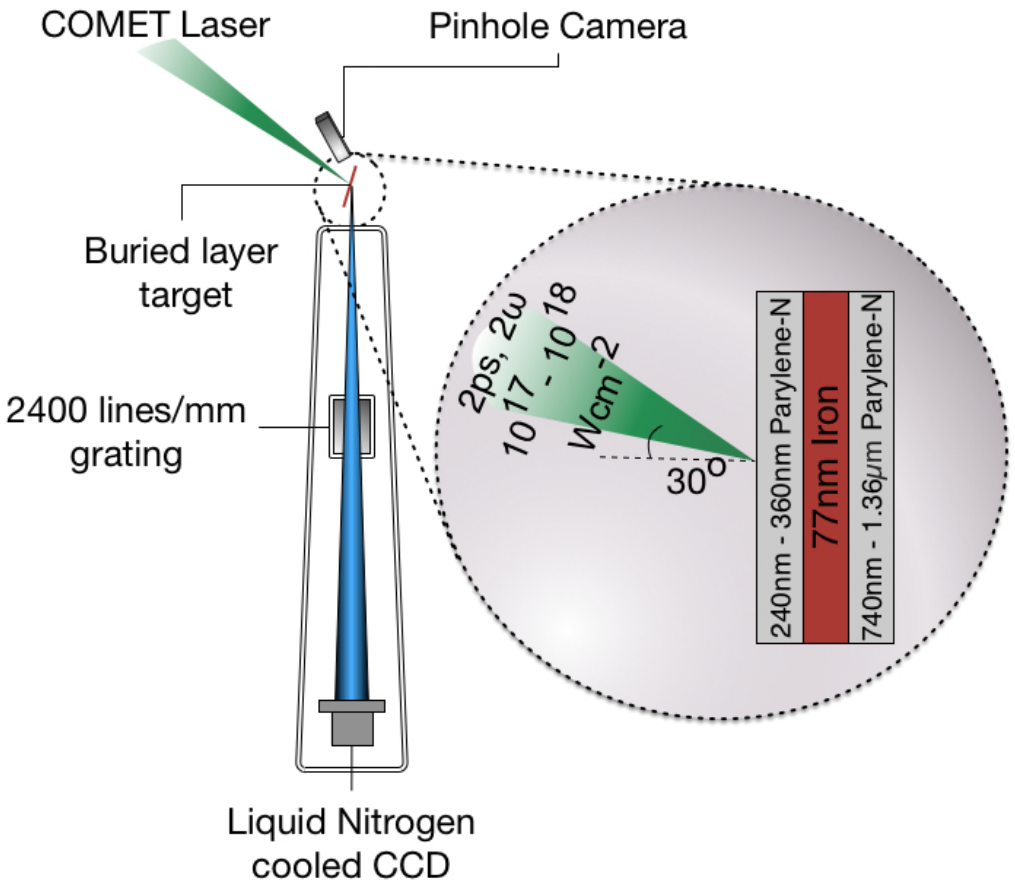

FIGURE 5.1: Schematic of the experiment showing the orientation of a high resolution grating spectrometer viewing the backside of a buried layer target at 5° to the target plane.

We find good agreement between experiment and simulation in the absolute intensities of the iron L-emission provided we allow for the heating of a plastic substrate in the targets by hot electrons. The comparison of experimental and simulated spectra is shown to enable a measure of target hot electron heating and the value of the flux limiter for thermal conduction.

5.2 Experiment

The L-shell time-integrated spectra have been recorded using a high resolution grating spectrometer at the COMET laser facility, Lawrence Livermore National Laboratory. The COMET laser is a Ti:Sapphire short pulse (1 - 4 ps) laser with a 4 stage Nd:Phosphate amplifier. A 4J frequency doubled ($\lambda = 527$ nm) laser with a pulse duration of 2 ps was used to irradiate a range of iron buried layered targets at intensities of the order $\sim 10^{17}$ Wcm^{-2} at an angle of 30 ° from target normal (figure 5.1). The focal spot diameter of $\simeq 20\mu$m was measured using an x-ray pinhole camera. The laser beam was s-polarised and frequency doubled using a KDP crystal. Frequency doubling ensures a high ($\sim 10^8$) contrast laser irradiation on the target [17]. Targets were composed of a 77 nm iron layer sandwiched between a 240 nm - 1.36 μm Parylene-N layers. The iron layer is tamped on both sides by the plastic to increase the uniformity and density of the iron layer after irradiation. Parylene-N was chosen as the tamping material as upon heating it is transparent in the 700 - 1200 eV photon energy range (see figure 5.8). The spectrometer was aligned at 5 ° to the target rear surface and hence potentially recorded the emitted iron spectra through upto 8.5 μm of cold solid Parylene-N which transmits 0.01 - 0.31 of 700 - 1200 eV energy photons.

Time integrated emission was recorded (e.g. see figure 5.2) from the rearside of the targets using a 2400 lines/mm variable spaced high resolution grating spectrometer (HRGS) with a liquid nitrogen cooled (temperature -110°C) Princeton PI-SX 1300 CCD camera with 1340 $\times$ 1300 pixels (pixel size 20 $\times$ 20 μm^2). The spectrometer slits were removed in order to increase the emission recorded onto the CCD, but spectral resolution remained high ($\simeq 500$) due to the small source size $\simeq 20\mu$m in the dispersing direction (measured with a pin hole camera). Positioning the spectrometer at the shallow viewing angle of 5° to the back of the target surface minimised Doppler shift effects on the spectral linewidths. Using equation

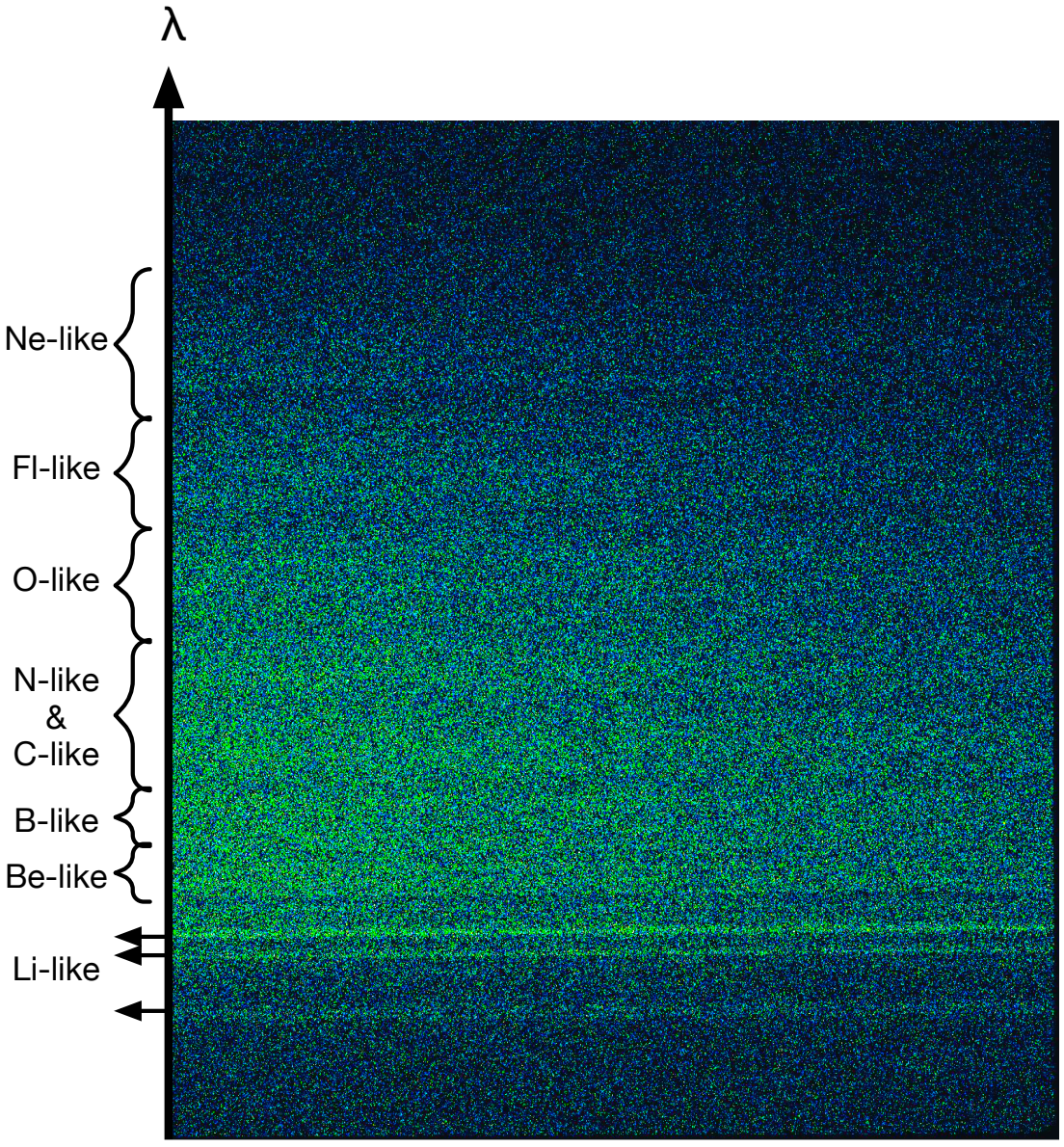

FIGURE 5.2: This figure shows the emission spectra as recorded using the high resolution grating spectrometer (HRGS) and the Princeton PI-SX 1300 CCD camera when a laser of irradiance $\sim 3 \times 10^{17}$ Wcm^{-2} is incident upon a buried iron layer target at 30° from target normal. The buried iron layer (77 nm) was tamped with a frontside plastic layer of 240 nm and rearside 740 nm parylene-N layer. Emission lines are grouped in ionisation stages as labelled.

3.23 the spectral lines are estimated to be blue shifted by -0.65 mÅ(see chapter 3.2.3). The spectrometer grating of radius of curvature 44.3 m was inclined at a grazing angle of 3.4° to the incoming radiation.

The buried iron layered targets were irradiated by the COMET laser with intensity ranging between $10^{17} - 10^{18}$ Wcm^{-2}. When high intensities irradiated the target, Li-like iron emission was stronger, while lower laser intensities produced spectra which was dominated by emission lines from lower ionisation states (see figure 5.3). The irradiance of the COMET laser was dependent mainly on the focal width of the laser pulse rather than the energy of the pulse, which remained relatively constant $\simeq$ 4 J. Therefore, high intensity laser pulses irradiate a smaller volume of the buried iron target resulting in a lower absolute emissivity. However, low intensity pulses irradiate a larger volume of iron, hence the iron emissivity is higher (see figure 5.3).

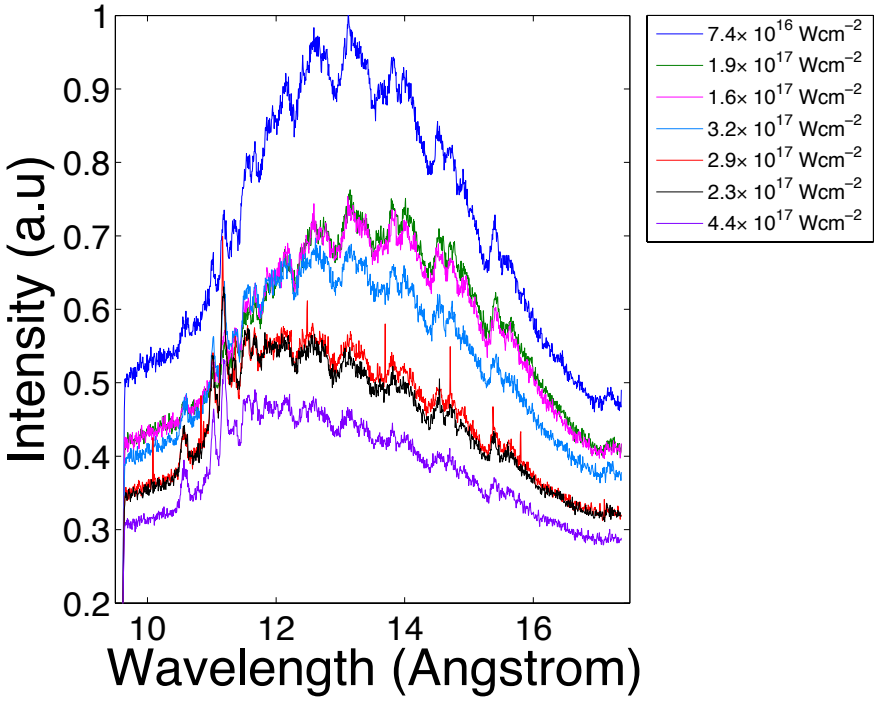

FIGURE 5.3: Emission spectra from a buried iron layered target comprising 77 nm iron and tamped with 240 nm (frontside) and 740 nm (backside) of parylene-N for laser irradiances $10^{16} - 10^{17}$Wcm^{-2}

The time-integrated emissivity $\epsilon(\lambda)$ of radiation emitted from the targets in J/m^2/sr/Å is given by [66],

$$\epsilon(\lambda) = \frac{\phi}{\Delta A_s \Delta\Omega} \tag{5.1}$$

where ϕ is a measure of the recorded time-integrated intensity. ΔA_s is the area of emitting surface and $\Delta\Omega$ is the solid angle collected by the spectrometer.

Using the Jacobian transformation [114] the emissivity $\epsilon(E_\nu)$ per unit photon energy, per unit area, per unit solid angle is given by,

$$\epsilon(E_\nu) = -\frac{d\epsilon(\lambda)}{d\lambda}\left(\frac{hc}{E_\nu^2}\right), \tag{5.2}$$

after the calibrated wavelength dispersion is converted to an energy scale. The time integrated spectral emissivity $\epsilon(E_\nu)$ from the target was measured in absolute units (ergs/cm^2/ster/eV) to an accuracy of $\pm$ 20% taking into account the spectrometer filtering (147 nm of Al) transmission (T_{Al}), the quantum efficiency of the CCD detector (Q_E) [115], the spectrometer grating reflectivity (R) [85] and the source size (A_s). Using equations 5.1 and 5.2 the target emissivity $\epsilon(E_\nu)$ can be written,

$$\epsilon(E_\nu) = \frac{\left(\frac{NE_\nu}{\Delta\lambda}\right)\left(\frac{12.39}{E_\nu^2}\right)3.6R_{AD}}{A_s\left(\frac{l_g sin(\theta)}{D_{sg}}\right)\left(\frac{l_d}{D_{sd}}\right)T_{Al}Q_E R T_{CH}} \tag{5.3}$$

where N is the time and spatially integrated number of counts recorded by the CCD detector within a spectral range $\Delta\lambda$ and E_ν is the photon energy in ergs. The source size (A_s (cm^{-2})) was measured using the x-ray pinhole camera (see figure 5.1). The solid angle ($\Delta\Omega$ (ster)) is a combination of the emission projected onto the grating and the integration length on the CCD detector in the non-dispersing direction. The solid angle is given by the term $\Delta\Omega = \frac{l_g sin(\theta)}{\Delta D_{sg}}\frac{l_d}{\Delta D_{sd}}$, where l_g is the length of the diffraction grating (5 cm), θ is the diffraction grating grazing

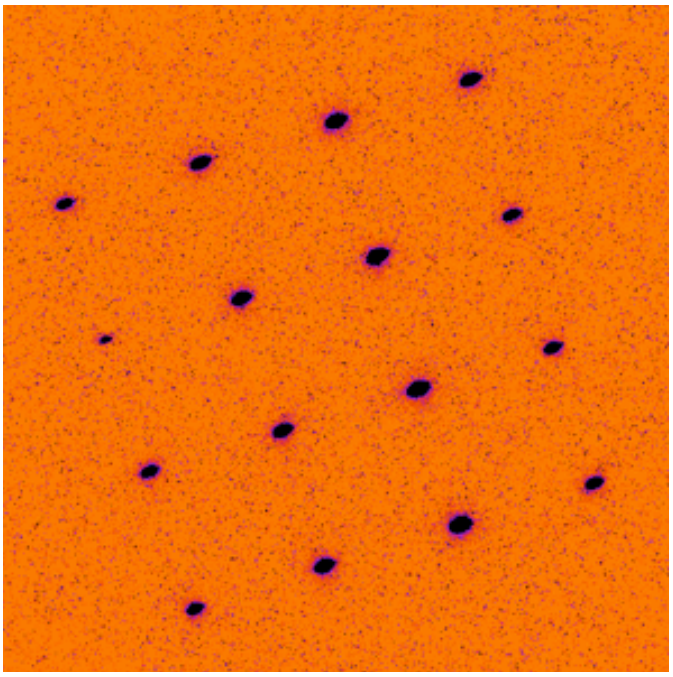

FIGURE 5.4: Emission from the heated buried iron layer target recorded using a pinhole. The pinhole camera was placed in front of the target 35° from the target normal and at an azimuthal of 51° (see figure 5.1).

incidence angle (3.4°), D_{sg} is the distance from the source to the grating, l_d is the distance of integrated pixels and D_{sd} is the distance between the source and the detector. The average energy required to produce a single electron-hole pair for a silicon CCD detector is 3.6 eV [103]. The number of electrons required to produced a count is given by the analogue to digital converter (ADC) value, R_{AD}. During the experiment the Princeton PI-SX CCD camera operated at a high gain ADC value of $R_{AD} = 1$. The error in the measurements of the target emissivity $\epsilon(E_\nu)$ is dominated by the source size error (20%) and the uncertainty in the number of CCD counts (10%) giving an absolute error of 20% in measured emissivity and a relative error for spectral line ratios of 10%. The total emissivity error calculated in quadrature is found to be 22%.

The L-shell emission of iron was recorded over the spectral range 700 - 1200 eV (figure 5.5). The spectrometer dispersion was calibrated using mylar target emission of oxygen Ly-α ($1s^2S_{\frac{1}{2}} - 2p^2P_{\frac{3}{2}}$) and He-$\alpha$ ($1s^1S_0 - 1s2p^1P_1$) lines. Key

features of the iron emission include Li-like Fe XXIV ionization lines at 1112.81 eV and 1127.04 eV and successive ionizations states observed in grouped bands from Be-like (Fe XXIII) to Ne-like (Fe XVII) states (figure 5.5).

5.3 Results and analysis

The recorded spectra were simulated using a time-dependent collisional radiative code, PrismSPECT [20]. Sample simulated spectrum are superimposed on figure 5.5. The HYADES one dimensional hydrodynamic Lagrangian fluid code [19] was used to simulate the spatial and temporal variation of electron temperature and density in the iron layer of the target and these results post-processed with PrismSPECT to generate simulated spectra $\epsilon(E_\nu)$ on an absolute scale which can be compared to absolute measured emissivity (see section 5.2).

The HYADES code modelled laser light absorption by inverse bremsstrahlung and resonance absorption with hot electron heating of the iron layer taken into account by having a specified percentage (0 - 10%) of the laser energy absorbed per unit mass in the target due to hot electrons. The recorded relative line intensities are sensitive to the hot electron heating in the plastic substrate (see figure 5.10). Although there is no unique combination that gives the measure line ratio, incorporating some hot electron heating ($\geq 1\%$) can reproduce the experimental iron line intensity ratios.

The effect of the variation of the thermal electron energy flux limiter on the simulated spectra is shown in figure 5.9. A flux limiter, f of the free streaming limit flux Q_{FS} is combined harmonically with Spitzer-Harm flux Q_{SH} in the HYADES code, such that the total heat flux Q is given by,

$$Q^{-1} = (Q_{FS})^{-1} + (Q_{SH})^{-1}. \tag{5.4}$$

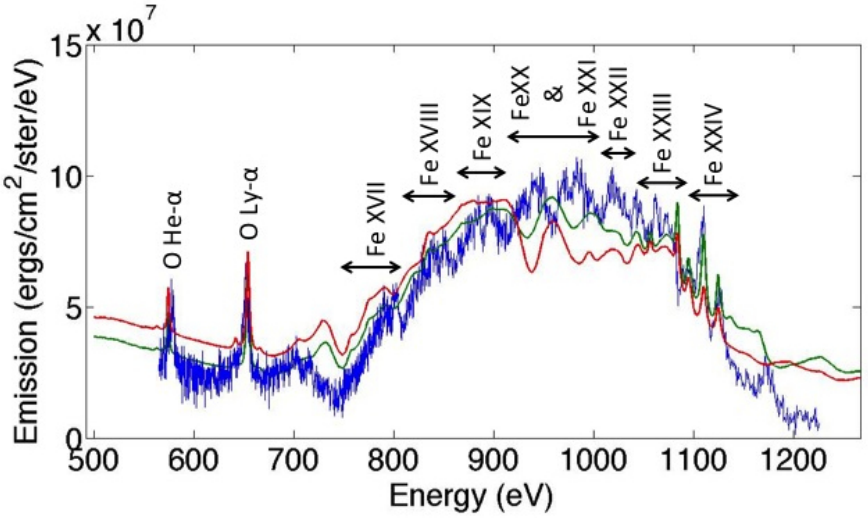

FIGURE 5.5: Spectra showing L-shell emission from two superimposed shots within the 600 - 1200 eV spectral range recorded from a buried layer target at incident irradiance of 3×10^{17} Wcm^{-2}. Simulations of the spectra are shown assuming LTE(green) and NLTE(red) spectral evaluations using the PismSPECT code post processing HYADES fluid code results.

Figure 5.8 shows that hot electron heating changes the 700 - 1200 eV photon energy transmission in the plastic substrate enabling the hot electron heating to be evaluated, while variation in the flux limiter strongly affects the iron emission lines present, enabling the flux limiter controlling heat flow to the iron layer to be evaluated. From figure 5.10, it is apparent that a flux limiter value of 0.04 $\pm$ 0.003 is appropriate for a broad range ($> 1\%$) of hot electron heating. Some hot electron heating ($\geq 1\%$), however, is required for the simulations to reproduce the experimental iron line intensity ratios.

For figure 5.8 the plastic opacity is taken from the TOPS opacity code [104] with the transmission evaluated using the HYADES predicted temperatures. The iron layer L-emission is optically thin with optical depth ranging between 0.02 - 0.31 at 700 eV and $\rho \simeq 2.4$ - 8.6 gcm^{-3} respectively, calculated from HYADES predicted electron densities and temperatures and TOPS opacities.

The presence of oxygen emission lines (eg figure 5.5) indicates that the buried

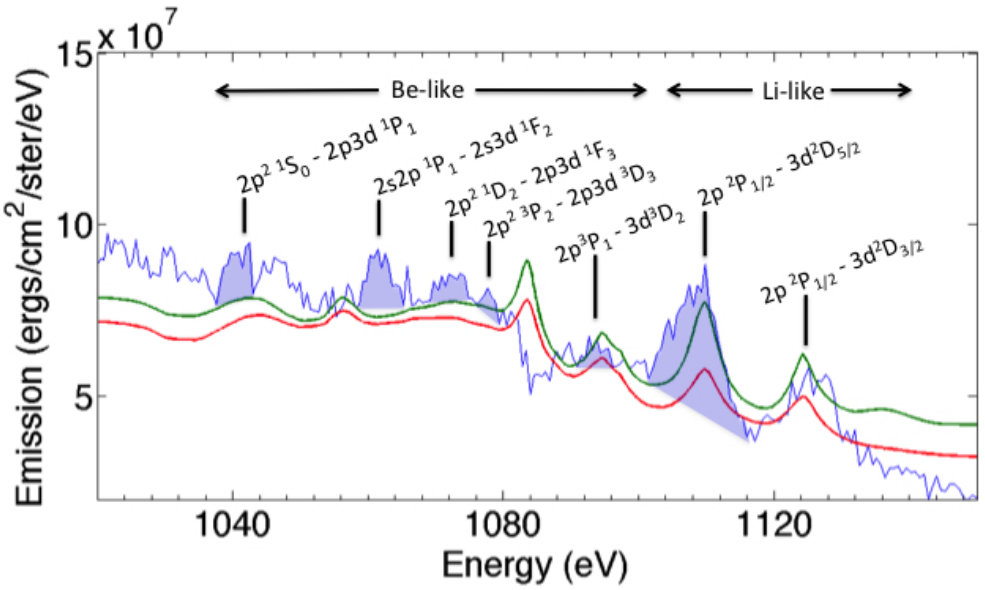

FIGURE 5.6: Iron spectra with identified lines of interest ranging from 1020 - 1140 eV. Spectral lines shaded here are used in equation 5.8.

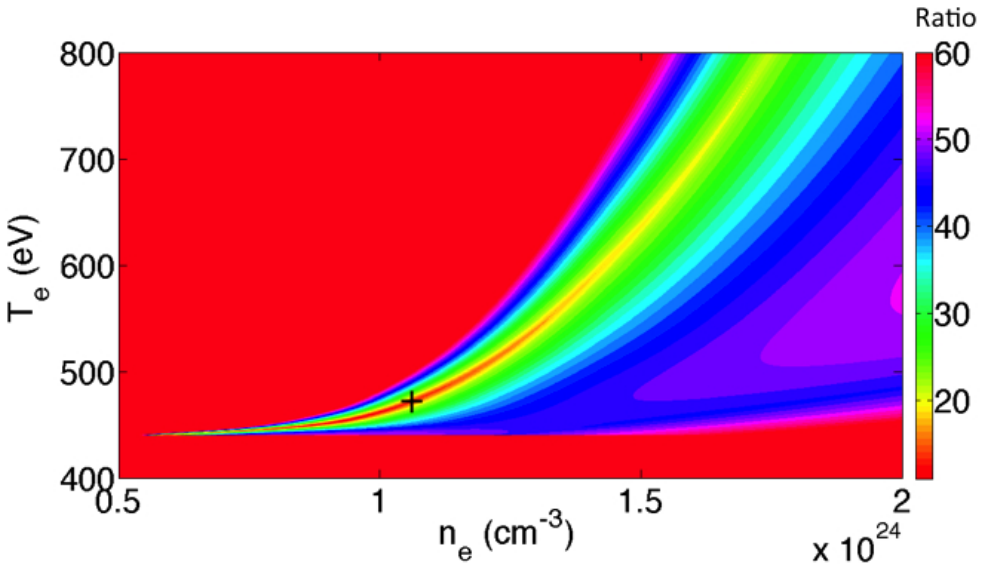

FIGURE 5.7: Contour plot showing the function $\Re$ presenting the difference between LTE evaluated line intensities and experimental measurement. The cross indicates when $\Re$ is at a minimum. This is the optimum plasma condition from which lithium & beryllium line emission arises.

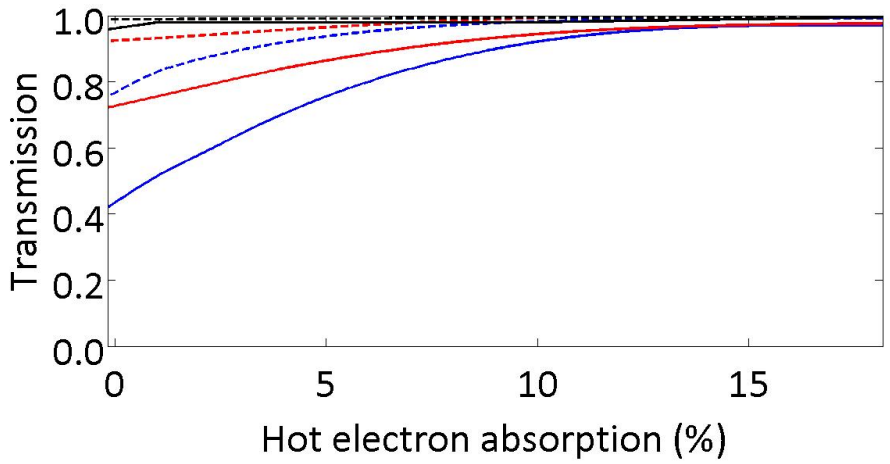

FIGURE 5.8: Calculated transmission of the rearside plastic layer of initial thickness 1.36μm at a 5^o grazing angle as a function of the hot electron energy absorbed for iron L-shell spectral emission in the range 700 - 1200 eV at the time of peak iron emission (3ps). The solid lines show the transmission for photons with energy 700 eV, whilst the dashed lines show transmission for 1200 eV photons. Results are shown for different HYADES values with flux limiter (0.02 (blue), 0.04 (red) and 0.06 (black)).

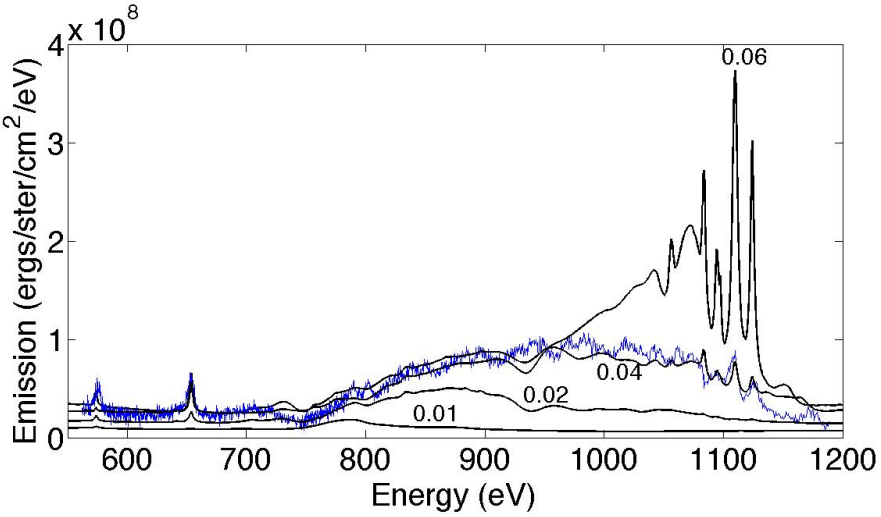

FIGURE 5.9: Simulated spectra with 3% hot electron heating assumed with different values of the flux limiter as labelled superimposed on an experimental spectrum.

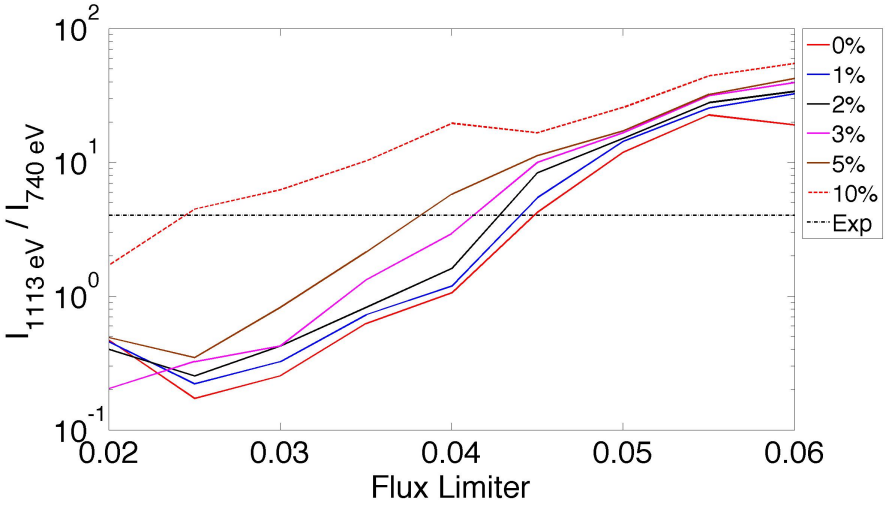

FIGURE 5.10: The simulated intensity ratio of the Li-like Fe line at 1113 eV ($2p^2P_{1/2} - 3d^2D_{5/2}$) and the Ne-like Fe line at 740 eV ($2p^6\ ^1S_0 - 2p^5(^2P_{1/2})3s_{1/2}$) as a function of the thermal conduction flux limiter for different values of assumed hot electron heating. The experimentally measured line ratio is shown as a horizontal broken line.

iron layer is oxidised. In our modelling with PrismSPECT this was taken into account by incorporating a 10% fraction of oxygen. Using PrismSPECT, this percentage of oxygen produced oxygen emission lines of intensity in the observed ratio to the intensity of the iron lines. Figure 5.11 shows the Ly-α and He-α impurity emission lines. From line ratios of Ly-α and He-α impurity oxygen lines, an electron temperature $\simeq$ 360 eV in the iron layer was deduced using the Saha-Boltzmann equation (with Stewart-Pyatt continuum lowering). At the time of peak iron emissivity, HYADES predicts that the iron layer has an approximate temperature of $T_e \simeq 400$ eV.

5.3.1 Detailed evaluation of electron temperature

Electron temperatures, T_e and densities, n_e in the iron layer of the targets were measured using the emission ratio of different Be-like spectral lines to the strong Li-like line ($2p^2P_{1/2} - 3d^2D_{5/2}$) at 1112.81 eV. As the density in the iron layer is

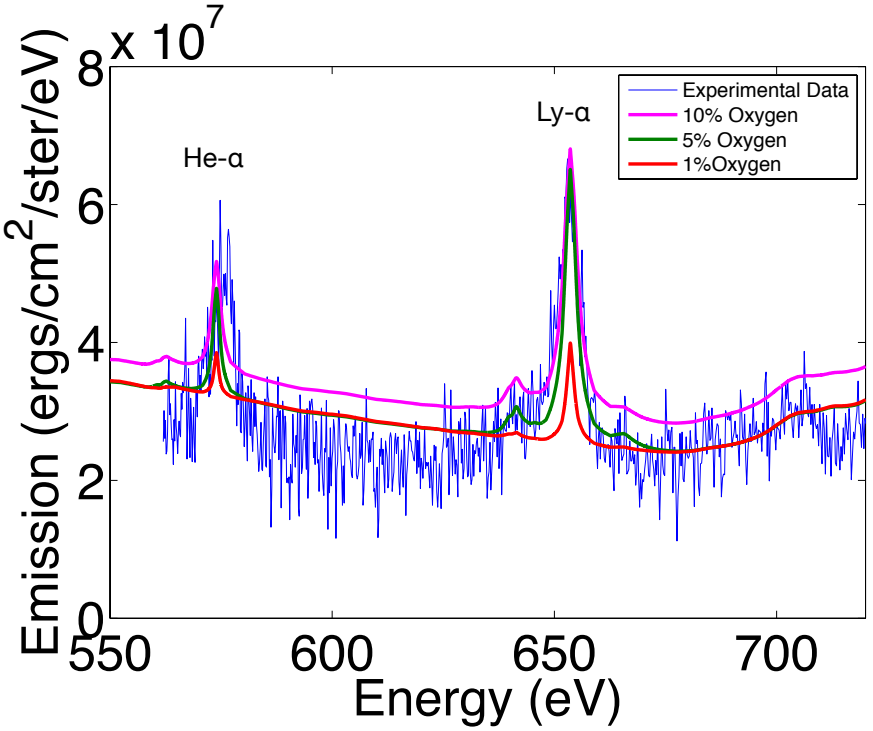

FIGURE 5.11: Figure shows the oxygen Ly-α and He-α impurity emission lines with PrismSPECT simulations overlaid for a range (1-10%) of assumed oxygen impurity percentages. The laser (3×10^{17} Wcm^{-2}) irradiated a buried iron layer (77 nm) encased in parylene-N frontside (240 nm) and backside (740 nm) thick plastic layers.

high ($n_e \sim 10^{24}$ cm^{-3}) at the time of peak emission and the times for LTE to be achieved are less than 1 ps, LTE can be assumed [116]. Simulations with the PrismSPECT code also show little difference between LTE and NLTE evaluations in the intensity ratio of the six lines employed for the T_e and n_e evaluation (see figure 5.5).

The relative intensity of spectral lines in adjacent ionisation stage is calculated using the Saha-Boltzmann equation to determine the quantum state populations associated with the upper levels of the emitted lines. The relative intensity of such

lines is thus given by

$$R_{th} = \frac{I_{\lambda'}}{I_{\lambda}} = \left(\frac{f'g'\lambda^3}{fg\lambda'^3}\right)\left(4\pi^{3/2}a_0 n_e\right)^{-1}\left(\frac{k_B T_e}{E_H}\right)^{3/2} \times exp\left(-\frac{E'_{gp'} + E_{p\infty} - \Delta E}{k_B T_e}\right) \quad (5.5)$$

where the higher ionization state is primed, f and g represent the oscillator strength and degeneracy of atomic levels, a_0 is the Bohr radius and E_H is the ionization energy of the hydrogen atom. The term which is exponentiated represents the energy difference between the upper levels of adjacent ionization states. This can be represented as the energy difference between the ground state and upper quantum state (p') of the higher ionization stage, $E'_{gp'}$ and the energy difference between the ionization energy and the upper level (p) of the lower ionization stage, $E_{p\infty}$. The ionization potential depression (IPD) of the lower ionization stage, ΔE has been calculated using the Stewart-Pyatt (SP) and the Ecker-Kroll (EK) model [117], using

$$\Delta E_{SP} = \frac{k_B T}{2(z^*+1)}\left[\left(\frac{3(z^*+1)ze^2}{4\pi\epsilon_0\lambda_D k_B T} + 1\right)^{2/3} - 1\right] \quad (5.6)$$

$$\Delta E_{EK} = \frac{ze^2}{4\pi\epsilon_0 r_{EK}}. \quad (5.7)$$

where λ_D is the Debye length, $z*$ is the degree of ionization, z is the charge state and $r_{EK}^3 = \frac{3}{4\pi(n_e+n_i)}$. The SP model deduced IPD values $\simeq$ 120 eV, whereas the Ecker-Kroll model produced IPD $\simeq$ 700 eV for the peak ($\sim$ 700 eV and 10^{24} cm^{-3}) temperature and density in the iron layer. Figure 5.14 shows the effect of assuming the Stewart-Pyatt or Ecker-Kroll models on the deduced temperature.

By considering a wide array of temperatures and densities (see figure 5.7), numerous theoretical line ratios $\frac{I_{\lambda'}}{I_{\lambda}}$ can be found for different plasma condition and evaluated using equation 5.5. The difference in the calculated line ratio and that observed experimentally are evaluated for several spectral line ratios using the

value $\Re$ given by,

$$\Re = \sum_{5\,lines} \left[\left(\frac{I_{\lambda'}}{I_{\lambda}} \right)_{theoretical} - \left(\frac{I_{\lambda'}}{I_{\lambda}} \right)_{experimental} \right]^2 . \tag{5.8}$$

A minima in $\Re$ is found when $\left(\frac{I_{\lambda'}}{I_{\lambda}}\right)_{theoretical}$ approaches $\left(\frac{I_{\lambda'}}{I_{\lambda}}\right)_{experimental}$ at the plasma conditions of density and temperature corresponding to where the spectral lines are emitted. The summation over multiple line ratios (see figure 5.6) increases the accuracy of this technique. Taking line ratios for Li-like Fe to Be-like Fe, the deduced temperature agrees with HYADES simulations of the peak temperature produced in the iron layer (figure 5.12) Post processing HYADES data with PrismSPECT shows the ionization fraction created in the iron layer as a function of time (see figure 5.12). Li-like emission arises at the leading edge of the laser pulse when the temperature reaches $\sim$ 700 eV and a density of $\sim 10^{24}$ cm^{-3}. As the plasma cools further, successively lower ionization states increase in population and emissivity giving rise to the band structure seen in the time integrated spectra.

5.3.2 Detailed comparison to simulations

Figure 5.13 shows the abundance of Li-like iron when hot electron heating and radiation transport is turned on or off calculated by the HYADES code. When both heating mechanisms are turned on (see figure 5.12) the rapid heating of the iron layer produces a large population of Fe XXIV (Li-like) ions. The energy transport mechanisms subsequently distribute the energy throughout the target and the iron layer eventually adiabatically cools. When both hot electron heating and radiation transport is turned off in the HYADES simulations (see figure 5.13) the initial iron zone rapidly heats up to an unrealistic electron temperature of $\sim$ 2 keV. As thermal conduction is a relatively slower process compared to hot

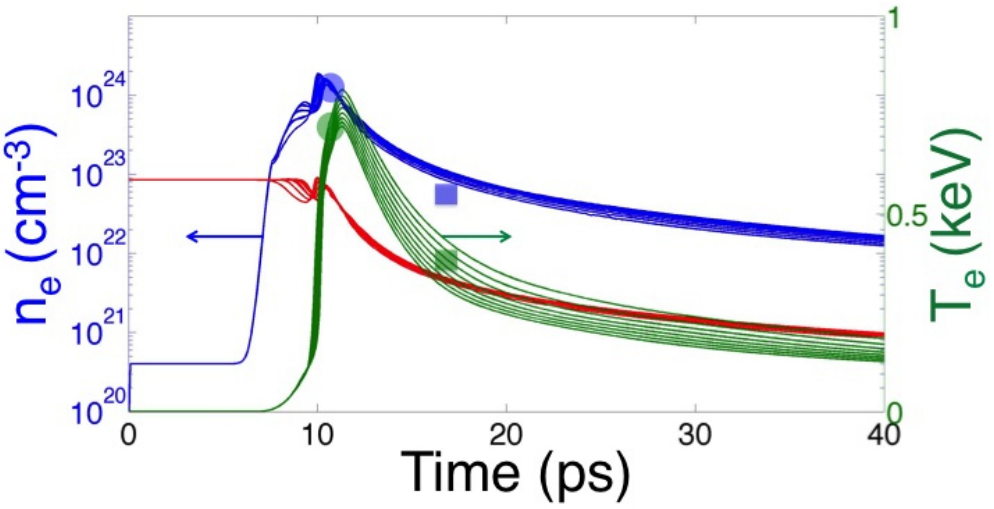

(a)

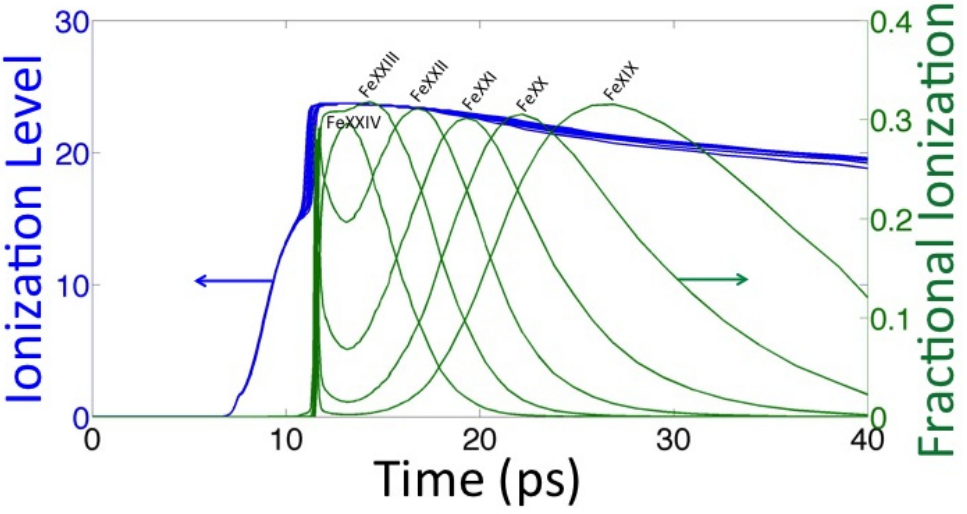

(b)

FIGURE 5.12: (a) Electron density (blue), ion density (red), electron temperature (green) and (b) ionization level within the iron layer as a function of time. HYADES simulations are shown for a second harmonic 2 ps laser pulse with irradiance 3×10^{17} Wcm^{-2} incident at time 10 ps on a buried layer target compromising 240nm CH overlay with a 77 nm Fe buried layer and another 740 nm CH layer, with the laser incident on the 740nm CH side. The deduced density and temperature using the ratio of Li-like to a Be-like line are shown as circles. A similar analysis using the intensity ratio of boron-like to a carbon-like line is superimposed as squares. The fractional ionization was calculated with HYADES and post processed using PrismSPECT. The experimental data points in 5.12(a) are placed at the time of maximum abundance (as shown in 5.12(b)) of both Li- and Be-like or B- and C-like iron.

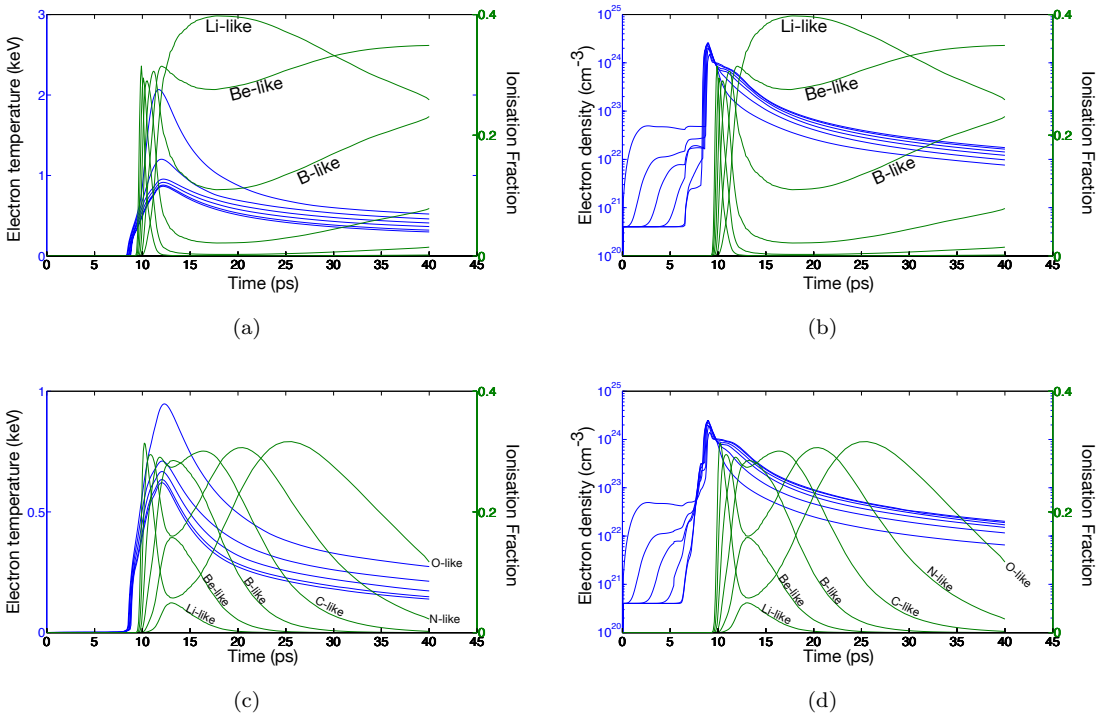

FIGURE 5.13: HYADES 1D hydrodynamic code was used to simulate the T_e and n_e of the buried iron layer when lasers irradiated (3×10^{17} Wcm^{-2}, 2 ps pulse duration, frequency doubled $\simeq 0.5\mu m$ light) buried layer targets comprised 240 nm (frontside) plastic layer, buried 77 nm iron layer and backside 740 nm plastic layer. The PrismSPECT collisional-radiative code was used to postprocess HYADES data to produce the ionisation fraction as a function of time. The abundance of Fe-like, Be-like etc ions were investigated as a function of time when certain energy transport mechanisms were turned on or off. Figures (a) and (b) show the T_e and n_e as a function of time when radiation transport and hot electron heating is turned off in the HYADES code. Figures (c) and (d) show the T_e and n_e as a function of time when hot electron heating is turned off but radiation transport is turned on. The laser is incident upon the buried iron layer target at 10 ps.

electron heating and radiation transport, the rate of energy transfer through the iron layer is significantly lower. Therefore a large abundance of Li-like ions exist over a longer timescale $\sim$ 15 ps. Figures 5.13(c) and 5.13(d) show the fractional ionisation with the T_e and N_e profiles overlaid when hot electron heating is turned off and radiation transport is turned on. In the absence of hot electron heating the population abundance of Li-like ions is low ≈ 0.08. This suggests that the level of hot electron heating can be measured from the intensity of the Li-like iron lines.

The time to reach peak conditions is ≈ 1 ps when both radiation transport and hot electron heating is turned on. However, when one or both heating mechanisms are turned off the time to reach peak conditions increases to ≈ 3 ps (see figure 5.13 and 5.12).

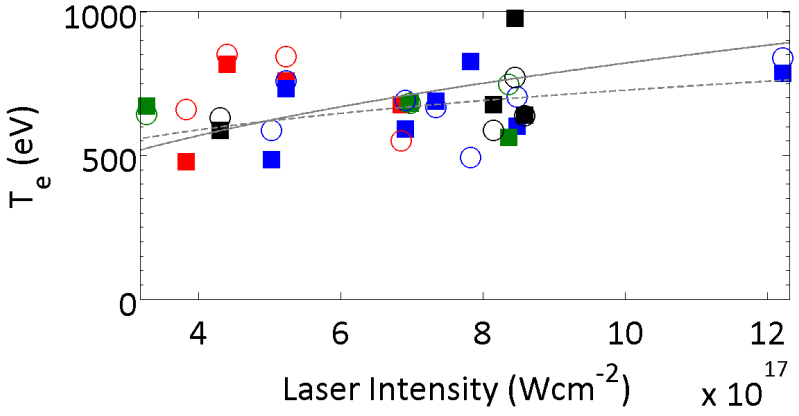

(a)

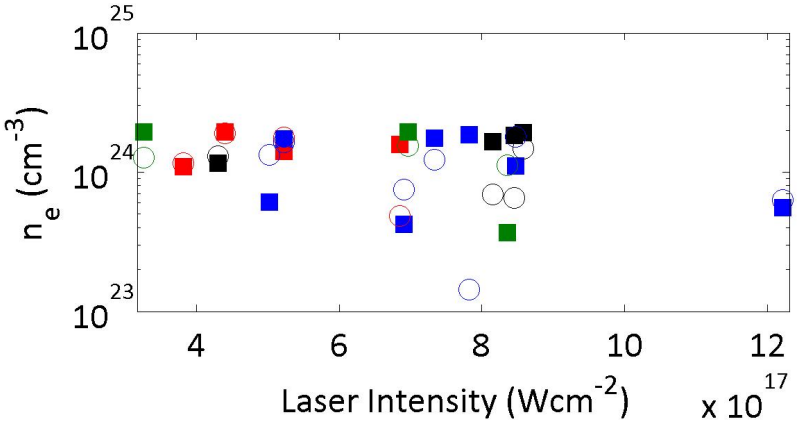

(b)

FIGURE 5.14: (a) Electron temperature as a function of laser irradiance deduced from equation 5.8 using 6 spectral lines for a range of different Parylene-N overlay thicknesses. Squares represent the ratio, $\Re$ calculated using the Stewart-Pyatt model and circles represent ratios determined using the Ecker-Kroll model. The solid curve shows a fit of the plasma temperature scaling with the Stewart-Pyatt model. The dashed curve shows the same but for the Ecker-Kroll model. (b) A graph showing the relative uniformity of electron density as a function of laser irradiance. (Overlay thickness: 240 nm - red, 360 nm - blue, 740 nm - green and 1.36 μm - black).

The technique of deducing the plasma conditions of density and temperature from several emitted spectral lines was further implemented to analyse spectra recorded

from a range of different buried layer targets with varied CH overlay thickness. The COMET laser intensity was also varied in the $10^{17} - 10^{18}$ Wcm^{-2} range. The measured electron density within the iron layer was approximately constant at $\sim 10^{24}$ cm^{-3} independent of the overlay thickness for these conditions indicating that emission occurs before significant plasma expansion (see figure 5.14(b)). The electron density of solid iron ionised to Li-like ionisation at 2×10^{24} cm^{-3} is only slightly above the spectroscopically measured densities (figure 5.14(b)), indicating that the expansion of the buried iron layer is small when the Be-like and Li-like emission occurs. Figure 5.14(a) shows a plasma temperature scaling of $T_e \propto \mathrm{I}^{0.2-0.4}$ for both Ecker-Kroll and Stewart-Pyatt ionization potential depression models with the Stewart-Pyatt model predicting slightly higher temperatures and densities. Fournier et al [36], for example, deduced a plasma temperature scaling of $T_e \propto (I_{abs})^{4/9}$.

5.4 Conclusion

Using the COMET laser at Lawrence Livermore National Laboratory iron spectra have been recorded with a high resolution grating spectrometer from targets with a thin layer of iron buried in plastic. Analysis using the 1D hydrodynamic fluid code, HYADES and collisional radiative code, PrismSPECT have shown L-shell iron emission of successively lower ionization states as the plasma expands and cools. Comparison between NLTE and LTE models have shown the iron plasma is close to local thermodynamic equilibrium. A novel technique using Saha-Boltzmann relations has predicted peak electron density and temperature conditions for the buried iron layered targets of different overlay thickness. By comparing simulated and experimental spectra, the effect of hot electrons on target heating and the value of the flux limiter has been deduced. The plasma conditions deduced from

Saha-Boltzmann relations are found to be insensitive to variations in laser intensity in the $10^{16} - 10^{17}$ Wcm^{-2} range and target overlay thickness in the 240 nm - 1.36 μm range.

Chapter 6

Diagnosing energy transport in buried layered targets using an extreme ultraviolet (EUV) laser

This chapter demonstrates the use of extreme ultra-violet (EUV) laboratory lasers in probing energy transport in laser irradiated solid targets. EUV transmission through targets containing a thin layer of iron (50 nm) encased in plastic (CH) after irradiation by a short pulse (35fs) laser focussed to irradiances 3×10^{16} Wcm^{-2} is measured. Heating of the iron layer gives rise to a rapid decrease in EUV opacity and an increase in the transmission of the 13.9 nm laser radiation as the iron ionizes to Fe^{5+} and above where the ion ionisation energy is greater than the EUV probe photon energy (89 eV). A one dimensional hydrodynamic fluid code HYADES has been used to simulate the temporal variation in EUV transmission (wavelength 13.9 nm) using IMP opacity values for the iron layer, and the simulated transmissions are compared to measured transmission values. When a deliberate pre-pulse is used to preform an expanding plastic plasma, it

is found that radiation is important in the heating of the iron layer, while for pre-pulse free irradiation, radiation transport is not significant.

6.1 Introduction

When a high power laser pulse of duration > 100 fs irradiates a solid target, most of the laser energy is directly absorbed in expanding plasma at densities typically $10^{-2} - 10^{-3}$ gcm^{-3} as the laser light only penetrates up to the critical electron density (see figure 2.2). With ultra-short duration (< 100 fs) laser pulses, deliberate or inadvertent pre-pulses (ie laser pedestal) create a similar expanding plasma with which most of the laser energy interacts. In laser-produced plasmas, the absorbed energy generally needs to be transported to the solid surface through expanding plasma of rapidly increasing density in order to contribute to heating and ablation of the remaining solid target. The energy can move via hot electrons produced in the interaction process, thermal electron conduction, and by the absorption of radiation emission from the hot sub-critical density plasma. As the laser absorption, thermal conduction, radiation emission and absorption all depend on electron temperature, energy transport mechanisms interact together creating a non-linear problem with many uncertain parameters, such as the rate of flux-limited thermal conduction [31, 118–120] and the radiative opacity of material [3, 5, 121].

Thermal energy conduction in near-uniform plasmas where the mean free path between collisions is much smaller than changes in the plasma density or temperature are modelled well using Spitzer-Harm conductivity [40]. However, between the critical density surface and ablation surface in a laser-produced plasma, gradients are steep and the Spitzer conductivity significantly over-estimates heat conduction. An upper limit on the heat transport flux Q is often estimated by assuming that the flow rate Q_f of thermal energy $n_e k T_e$ occurs at rate $f n_e k T_e v_{th}$,

where n_e is the electron density, kT_e is the electron temperature, v_{th} is the average thermal velocity and f is known as the flux limiter (see section 2.4.1). In many simulations, f is a free parameter with values of typically $0.03 - 0.15$ and is used to obtain agreement of experimentally measured quantities such as ablation rates with simulations. Fokker-Planck codes calculating electron distribution functions in steep gradients have shown that flux limiter f values of approximately 0.1 are often appropriate [122]. The total flux of heat transport (Q) is usually obtained in simulations using equation 2.23.

Solid targets with a buried layer of a signature material have been used to measure plasma conditions of the buried material [9, 123, 124]. Similarly, the heating of the buried layer enables measurement of the energy transport into the target [10]. Emission spectroscopy (see chapter 4) or impurity absorption spectroscopy can deduce the temperatures and densities of the buried layer [18, 110]. Probing a target with a thin layer of iron in an otherwise plastic target with an extreme ultra violet (EUV) laser backlighter enables a sensitive measurement of the heat flow to the iron [75]. Un-ionised iron is highly opaque to EUV light, but ionised iron becomes transparent when significant populations of Fe^{5+} irons are present where the ionisation energy (99 eV) is greater than the EUV photon energy (89 eV in our case, see figure 6.1).

This chapter presents EUV transmission measurements where the target was irradiated with a controlled pre-pulse causing production of a large coronal plasma soft x-ray emission and a controlled density profile for interaction of a short pulse (35 fs) at irradiances 3×10^{16} Wcm^{-2}. With a pre-pulse, comparisons of our EUV transmission results with simulation show that radiation heating dominates the target energy transport and hot electron heating has little effect, while similar experiments without a pre-pulse show that hot electron heating is important (see figure 6.13) [75].

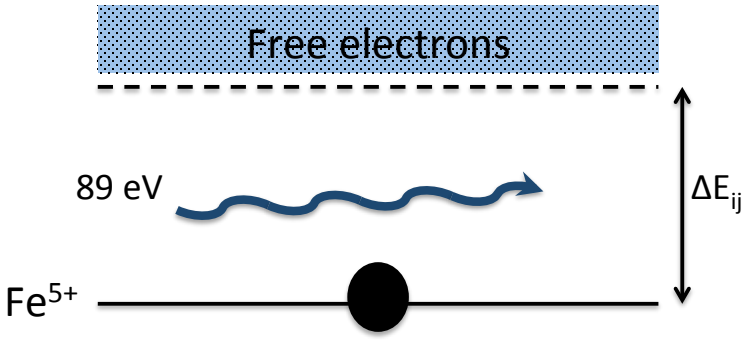

FIGURE 6.1: When the heated iron layer reaches Fe^{5+} the bound-free energy gap ($\Delta E_{ij} = 99$ eV) becomes larger than the incident EUV photon energy (89 eV). This switch in transparency can be utilised to diagnose the heated buried iron layer.

6.2 Experiment

The targets were irradiated by a high contrast ($\sim 10^9$) p-polarized laser of pulse duration 35 fs at 3×10^{16} Wcm^{-2} and a 35 fs pre-pulse of 3×10^{15} Wcm^{-2} 20 ps before the main pulse. The laser of wavelength 0.8 μm was focussed to a focal spot diameter of $\simeq 40$ μm at a range of angles of incidence $18° - 33°$. The targets comprised 39 nm frontside and 207 nm rearside parylene-N layers encasing a buried 50nm thick iron layer.

The LASERIX extreme ultraviolet (EUV) laser [25] was produced using the transient collisional pumping scheme [97] (see chapter 4). Initially a $\simeq 6$ ns frequency doubled pre-pulse (4×10^9 Wcm^{-2}) is line-focussed onto a silver target producing an expanding coronal plasma. After a $\simeq 5$ ns delay a shorter $\simeq 3$ ps laser irradiates (4×10^{12} Wcm^{-2}) the preplasma at a 20° grazing-incidence angle. The EHYBRID and RAYTRACE codes were used to simulate the x-ray generation delay between the pumping laser and the peak output x-ray laser intensity, which was found to be ≈ 30 ps. The EHYBRID and RAYTRACE simulations (see figure 6.2) predict a ≈ 3 ps pulse duration for the EUV laser, which is similar to the temporal duration of the pumping laser.

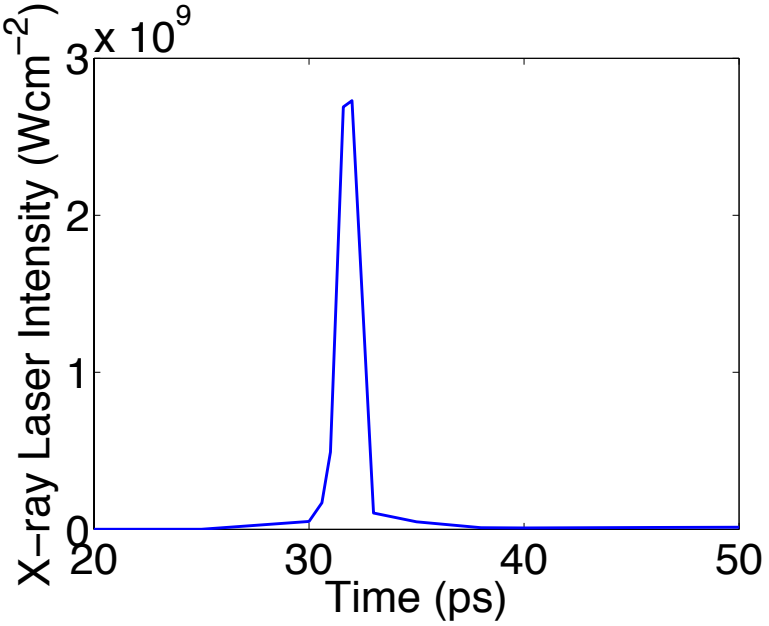

FIGURE 6.2: A RAYTRACE code was used to post-process the simulated EHYBRID gain length product to calculate the output x-ray intensity $\simeq 10^9$ Wcm^{-2}. The x-ray laser pulse has a duration of $\simeq 3$ ps and a generation delay of $\simeq 30$ ps after the main pulse.

The EUV laser was timed to probe the irradiated target at various times before and after the 35 fs main pulse was incident. An EUV imaging system (see figure 6.3) recorded the spatial variation of the transmitted 13.9 nm laser radiation, enabling the extra transmission occurring due to the iron heating in the 35 fs laser focal region to be measured (see figure 6.4).

Figure 6.4 shows a speckle pattern which appears in the far field image of the EUV laser. The speckle features are randomly distributed and vary in size and shape. Each speckle arises from the amplification of on initial spontaneously emitted photon [125]. We have undertaken EUV laser transmission measurements using an individual speckle as the speckle size at the probed target was larger than the irradiated focal area. Some shots were eliminated from our analysis as the laser focal area at the target did not correspond to an EUV laser speckle.

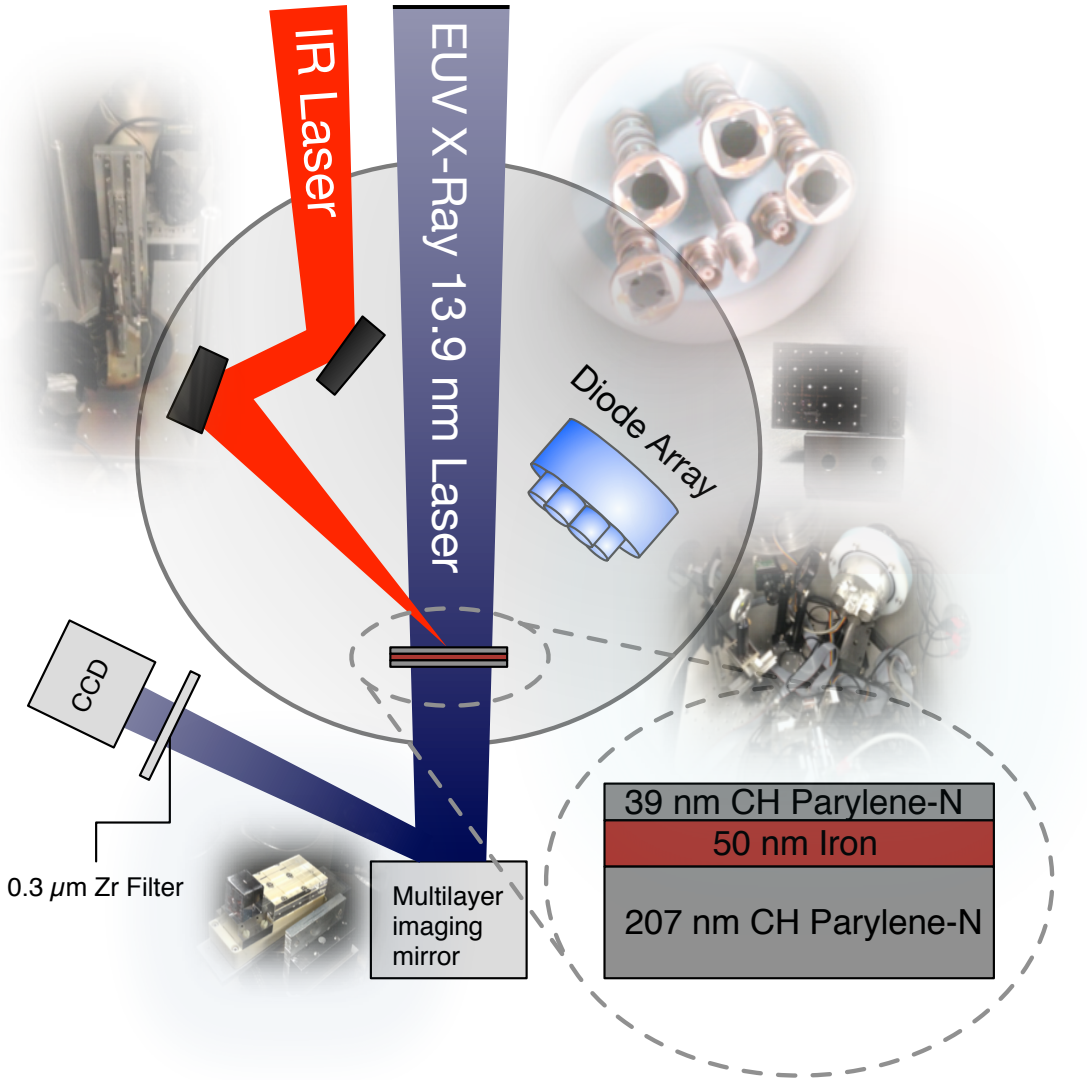

FIGURE 6.3: Experiment layout with a 3×10^{16} Wcm^{-2} laser and 10% prepulse incident upon a buried 50 nm iron layer encased in 39 - 207 nm parylene-N layers. Transmission through the iron layer was measured using an EUV laser back-lighter. A filtered x-ray diode array was used to determine hot electron temperatures.

Figure 6.5 shows a comparison between the cold solid iron CXRO transmission (black line) and the heated iron layer as a function of photon energy.

The transmission, T of the 13.9 nm x-ray laser through the buried layer is related by Beer's law to density ρ and opacity σ in the target by,

$$T = \frac{I}{I_0} = exp\left(-\int \rho\sigma dx\right) \tag{6.1}$$

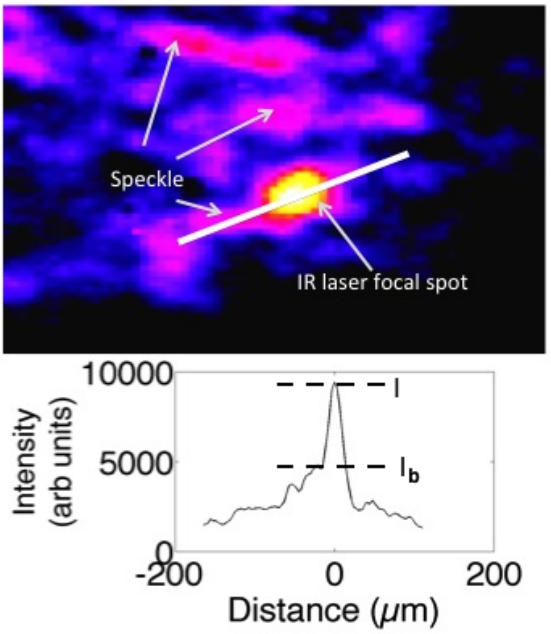

FIGURE 6.4: Transmission image of the EUV laser with the heating laser incident through the buried layer target (as labelled). The EUV laser coherance caused speckle on the focussed EUV beam at the target. The solid white line out across the focal spot shows an increased EUV transmission, T from the heated iron plasma with I_b representing the transmission through the unheated solid target).

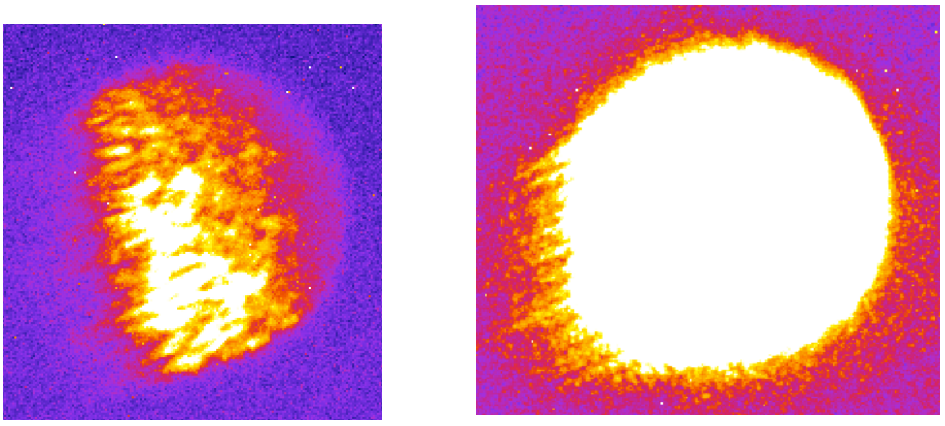

(a) (b)

FIGURE 6.5: (a) EUV transmission through the cold buried iron layer target. (b) EUV transmission when no target placed. Both images are set to the same contrast and brightness for comparison.

where I is the intensity of the EUV laser pulse that has passed through the buried layer target and I_0 is the EUV intensity incident onto the target deduced from the

transmission through an area of unheated target. The integration with respect to x is through the target thickness. Examples of the experimentally measured transmission of the target at 13.9 nm as a function of time are shown in figure 6.7 for a laser angle of incidence of 18°. Similar temporal variations of transmission were found to occur at varying laser angles of incidences from 18° to 33° (see figures 6.7, 6.8 and 6.9).

A diode array placed at angle of 35° from the target normal housed 4 diodes with filters of varied thickness, each recording a spectral region of the hot electron bremsstrahlung emission. Hot electron temperatures $\simeq 20-30$ keV were measured [51, 52] (see figure 6.6). To investigate whether the iron buried layer is heated by

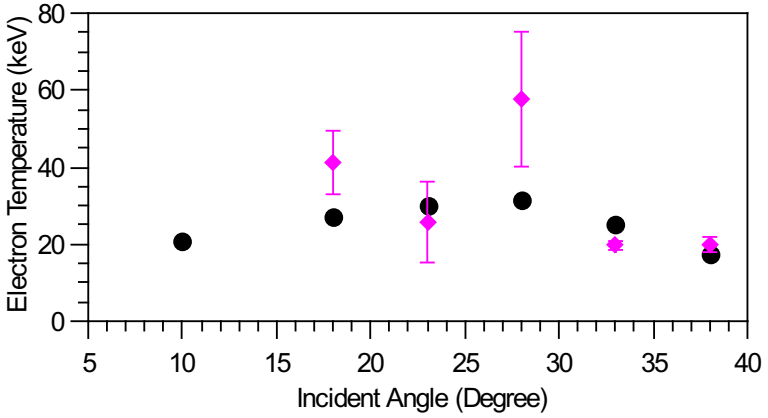

FIGURE 6.6: The hot electron temperature as a function of the laser incident angle measured using the four channel diode array (diamonds) and found using EPOCH PIC simulations with a scale length 0.65 μm (black circles). This image is taken from Culfa et al [51].

the EUV laser, a target was sequentially irradiated by 50 EUV laser shots without any infra-red laser irradiation. The transmitted EUV laser radiation remained approximately constant at a value consistent with the solid transmission of the target at 13.9 nm and there was no evidence of target damage.

6.3 Analysis and results

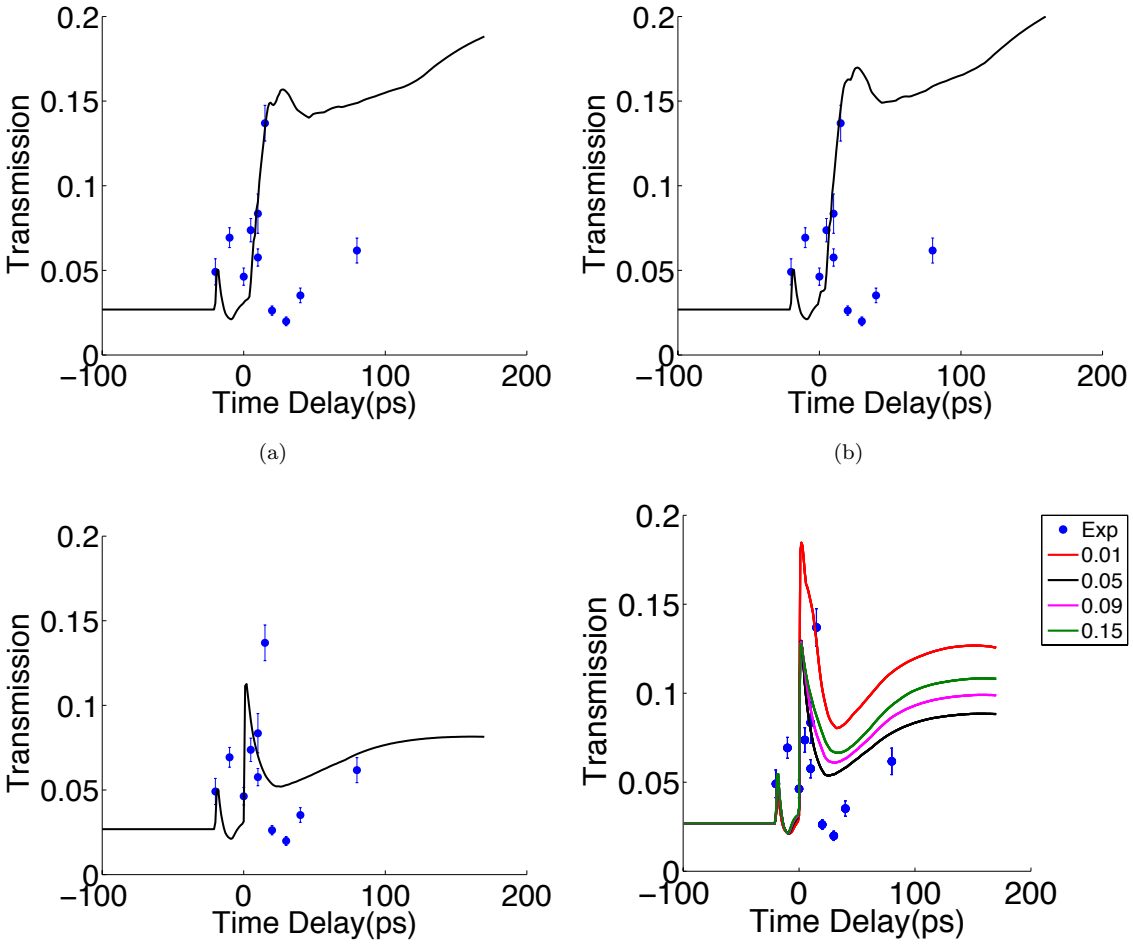

FIGURE 6.7: Experimentally measured transmitted EUV laser light through irradiated targets as a function of time (relative to the peak of the irradiating pule) overlaid with HYADES transmission simulations such that (a) radiation and hot electron heating are turned off, (b) radiation heating is turned off but hot electron heating is turned on, (c) radiation heating is turned on, hot electron heating is turned off, (d) radiation and hot electron heating are turned on for a range of flux limiter values as labelled. The heating laser irradiation peaking at 3×10^{16} Wcm^{-2} was incident at 18° with respect to the target normal and 10% of the laser energy is assumed absorbed as hot electron heating.

The one dimensional Lagrangian hydrodynamic fluid code HYADES [33] was used to simulate the infra-red laser interaction with the buried layer target. Hot electron heating, radiation transport, flux limited thermal conduction (see equation 2.23) and resonance absorption heating were modelled in the code.

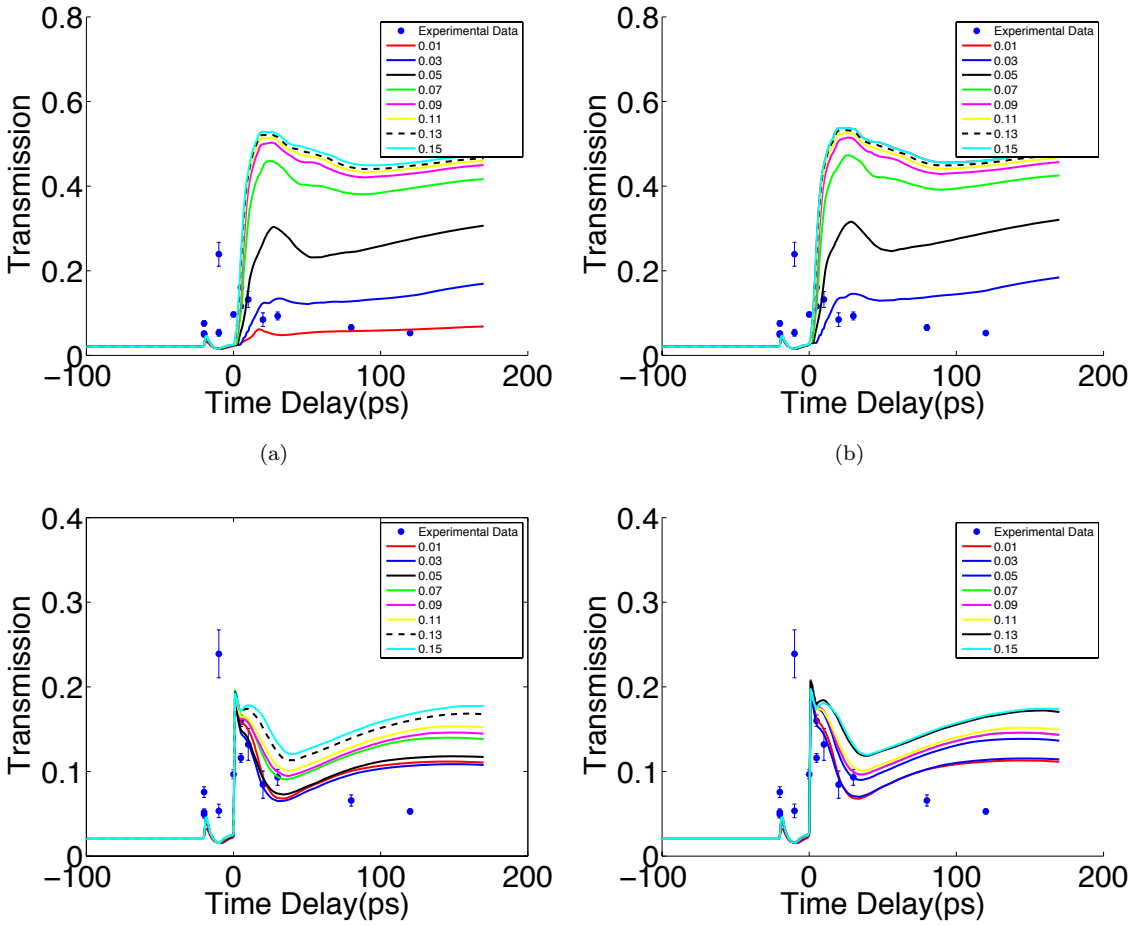

FIGURE 6.8: Same as figure 6.7 however the laser incidence angle is 28° from target normal. Higher flux limiter values predict a larger transmission through the iron layer.

The predicted laser energy-hot electron conversion efficiency for the s-polarised COMET laser ($\approx 3\%$) was lower (chapter 4) than the p-polarised LASERIX heating laser ($\approx 10\%$) which was used in this chapter. In chapter 4 the conversion efficiency was deduced using emission spectroscopy. However, in this chapter the hot electron heating of the target was taken into account by using the Key et al scaling efficiency [54] (see section 2.4.3). A nominal (typically 10%) fraction of the laser energy was deposited into the target and was distributed according to the mass density of the target (see figure 2.9).

The HYADES code simulates radiation transport by using a multigroup diffusion method (see section 4.4). The simulations shown in figure 6.10 incorporated

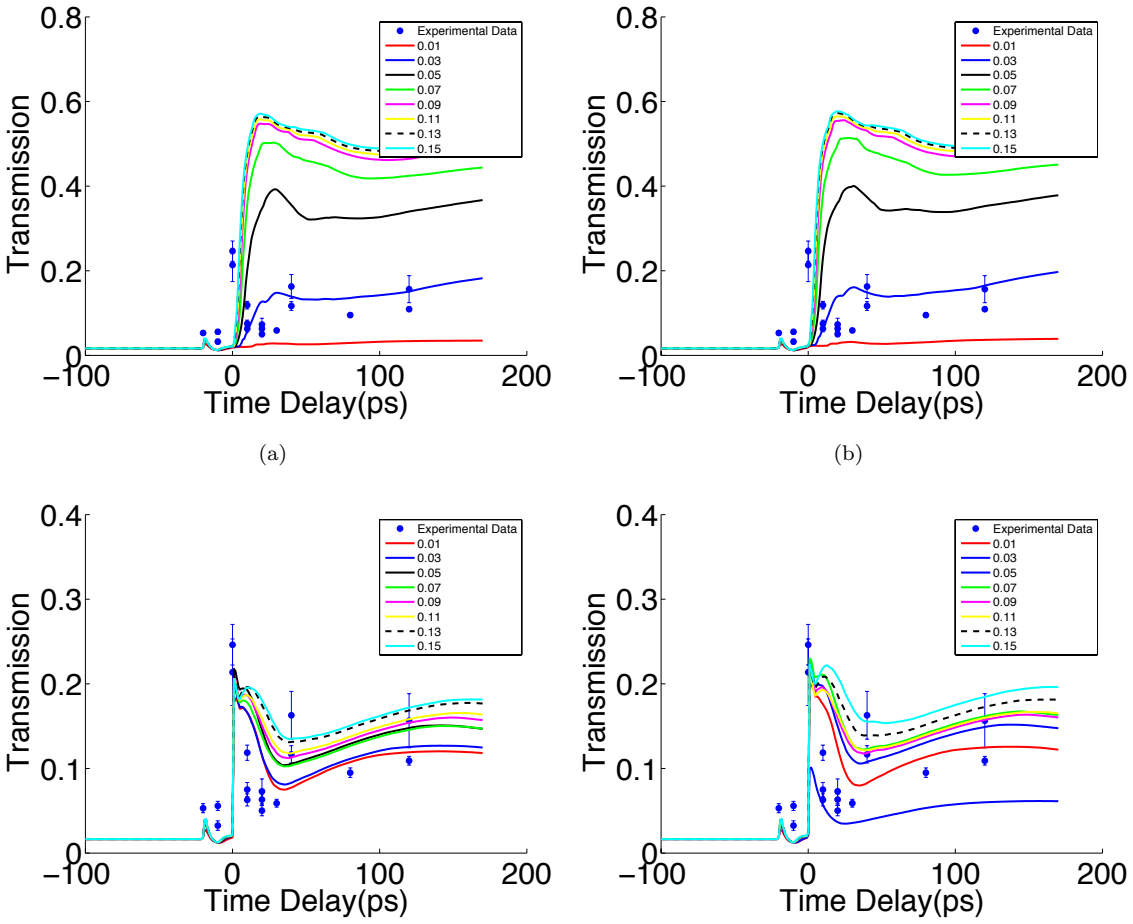

FIGURE 6.9: Same as figure 6.7 however the laser incidence is at and angle of is 33° from target normal.

100 multigroups with photon energies ranging logarithmically between 0.01 - 40 keV. To simulate electron heat conduction, the code uses the flux limited diffusion approach and a parameter scan was employed for a range of flux limiter values. The HYADES predictions for density and temperature (see figure 6.10) were post-processed using IMP opacities [62] to deduce the transmission of the 13.9 nm radiation through the target [75] (see figure 6.7). When thermal energy transport mechanisms are turned off the front mesh zone of the iron buried layer reaches electron temperatures $\simeq$ 200 eV (see figure 6.10(b)). However, when radiation transport and hot electron heating are turned on HYADES predicts a lower electron temperature of $\simeq$ 55 eV (see figure 6.10(a)).

In figures 6.7, 6.8 and 6.9 the HYADES code simulates lower transmission in the buried iron layer target when low flux limiter values are used. However, when the flux limiter is set to 0.01 the HYADES code predicts a much larger transmission compared to the experimentally recorded transmission. This phenomena may occur in the HYADES code due to the poor thermal conduction away from the critical density leading to very high temperatures in the front iron simulated zone of the buried iron target. Therefore the predicted transmission for the flux limiter when set to 0.01 is higher due to the initial high plasma temperatures. The IMP opacity code predicts lower opacities at higher thermal temperatures (see figure 4.16).

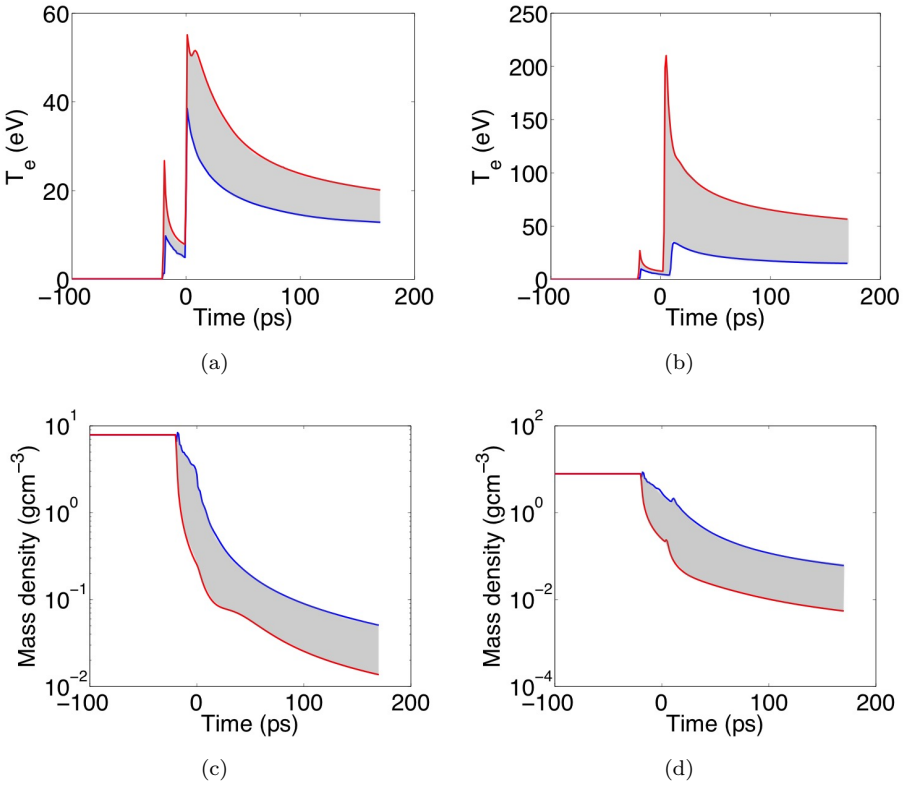

FIGURE 6.10: HYADES simulated electron temperatures, T_e and mass densities ρ as a function of time for the front (red) and rear (blue) mesh zones of the buried iron layer. The simulation used a flux limiter of 0.05 and the angle of incidence was set to 18° with respect to target normal. In the HYADES simulations the prepulse arrives 20 ps prior to the mainpulse (100 ps). Figures (a) and (c) show temperature and density conditions for the iron buried layer when energy transport mechanisms are turned on. Figures (b) and (d) show temperature and density profiles when radiation transport and hot electron heating is turned off.

The simulations best fit the experimentally measured 13.9 nm transmission when radiation transport is switched on, but hot electron heating (with energy fraction 10% as envisaged to be feasible) has a negligible effect on the simulated transmission (see figure 6.7). Simulations with a flux limiter of approximately 0.05 were found to produce EUV transmission through the targets comparable to the experimental transmission profiles (see figure 6.7(d)).

The upper limit of the multigroup photon energy was varied between (1 - 100 keV) to simulate a range of transmission profiles as a function of time through the buried iron target (see figure 6.11. The peak transmission through the iron

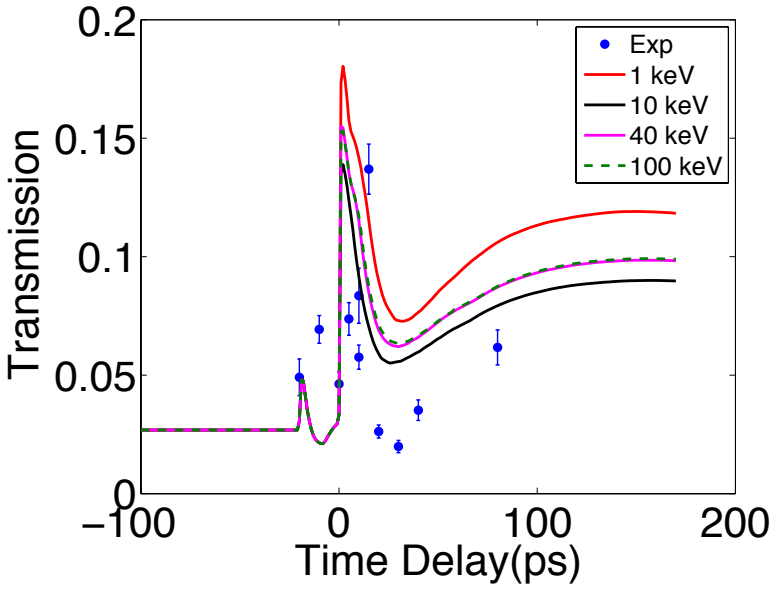

FIGURE 6.11: The transmission through the buried iron layered target was simulated using the HYADES code by varying the maximum photon energy of the multi-grouped radiation field (1 - 100 keV).

target ranged between 0.14 - 0.18 when varying the maximum photon energy of the multigroup radiation field (1 - 100 keV). The simulations show that radiation heating due to higher photon energies $>$ 40 keV does not affect the transmission through the buried iron layer.

6.3.1 The role of a pedestal prepulse on energy transport mechanisms.

The presence of an inadvertent laser pedestal which precedes a high contrast laser pulse ($\sim 10^8$) similar to those found by Wilson et al [75] can preheat the buried iron layer target. The origin of a laser pedestal is related to the finite bandwidth of the laser system and incomplete compression in CPA [30, 126] (see chapter 2).

Figure 6.12 compares the transmission of the EUV laser probing through the heated buried iron layered target, when the target is irradiated by a deliberate Gaussian prepulse of pulse duration 35 fs at time 20 ps before the 35 fs main pulse, and a laser pedestal which precedes a single high contrast laser pulse (measured using an auto-correlator). At 40 ps before the main pulse the laser pedestal has a contrast of 10^{-7} which then increases to 10^{-4} contrast 1 ps before the 35 fs main pulse. When the iron layer is irradiated with a deliberate prepulse the transmission is relatively low compared to when only a laser pedestal is present.

Figure 6.13 shows that when buried iron layered targets are irradiated by a single high contrast laser pulse the transmission through the iron layer is dependent on hot electron heating. However, when the deliberate 10% prepulse is used the hot electron heating is negligible (see figures 6.7,6.8,6.9) compared to the effect of radiation heating. Without a deliberate pre-pulse, the experimentally measured EUV transmissions show that the radiation transport has a less significant effect on the buried iron layer transmission (see figure 6.14). The production of hot electrons is dependent on parametric instabilities and resonance absorption absorption processes (see chapter 2). Chapter 2 showed that the resonance absorption efficiency proportional to $\phi(\tau)$) was dependent on the laser incident angle, θ (see figure 2.6). The relative resonance absorption efficiency $\phi(\tau)$ for the pedestal prepulse (scale length $\approx 0.2\mu$m) and deliberate prepulse (scale length $\approx 1\mu$m) was $\simeq 0.4$ and

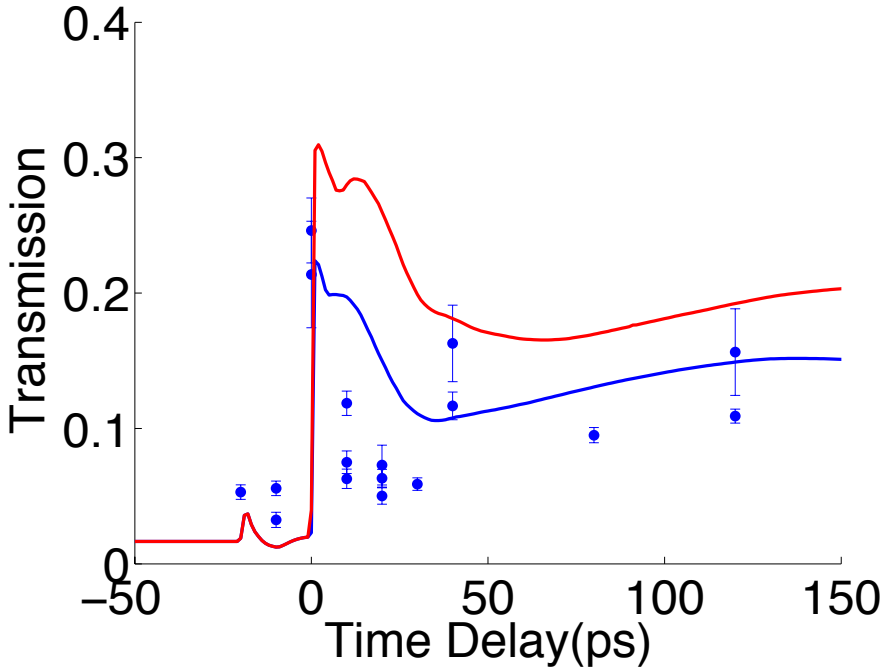

FIGURE 6.12: The temporal change in transmission of the EUV laser beam through the heated iron layer when using a deliberate prepulse of 10% of the laser energy (blue curve) or a pedastal (red curve) prepulse with 5% of the laser energy. The simulations were produced for a laser incident on the target at 33° from target normal. When a pedestal prepulse ramp is present the peak transmission is higher (≃0.3) compared to when a deliberate prepulse is used (≃0.2). The experimental results shown were produced when the laser (3×10^{16} Wcm^{-2}) irradiated the buried layer target at an incident angle of 33° from target normal. The buried layer target contained a 50 nm iron layer and a frontside 39 nm and rearside 207 nm plastic layers. A flux limiter of 0.05 was used in the HYADES code.

$\simeq 0.6$ respectively (see section 2.3.3), so we expect similar hot electron production With a deliberate pre-pulse, the larger expanding coronal plasma produced more radiation heating which can, however dominate the hot electron heating.

For hot electron temperatures > 10 keV, hot electron absorption within the iron layer is low (≤ 0.01, see figure 6.15(a)) while radiation absorption is high (see figure 6.15(b)). The absorption, A of electron kinetic energy, E in figure 6.15(a) is calculated for solid, room temperatures iron using,

$$A = 1 - exp(-\sigma_{av}(T_e)\rho\Delta x) \tag{6.2}$$

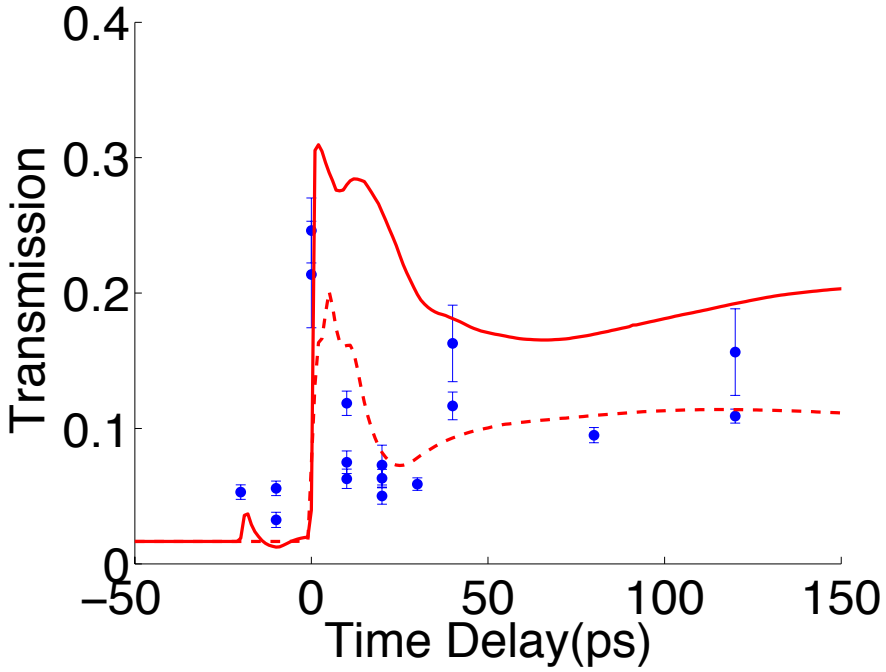

FIGURE 6.13: The transmission through the iron layer recorded by the CCD camera is shown in blue. Figure shows the transmission through the target when a single highly coherent laser pulse irradiates a buried iron target. Using HYADES the transmission was simulated when the hot electron heating was turned on (solid) and off (dashed). This figure shows that the buried iron layer is susceptible to hot electron heating when no prepulse is used.

where $\sigma_{av}(T_e)$ is the photon averaged solid iron absorption coefficient for temperature T_e. Hot electrons deposit their energy during the 35 fs main laser pulse, so the iron layer is solid and cold during the hot electron heating.

Figure 6.15(b) shows values of radiation absorption within the 50 nm iron layer calculated using the IMP [62], TOPS [104] and PROPACEOS [20] codes for conditions (see figure 6.10) when the iron layer has been heated to a maximum temperature ≈ 30 eV and some expansion of the iron layer has occurred so the density $\rho \approx 2$ gcm^{-3}. For comparison, the solid, room temperature absorption in the iron layer and the values of the opacity assumed in the HYADES radiation hydrodynamics code are also plotted in figure 6.15(b). Due to the multigroup diffusion model of radiation transport in HYADES, the opacity at photon energies < 100 eV is assumed constant and underestimates the opacities for photon energies < 30

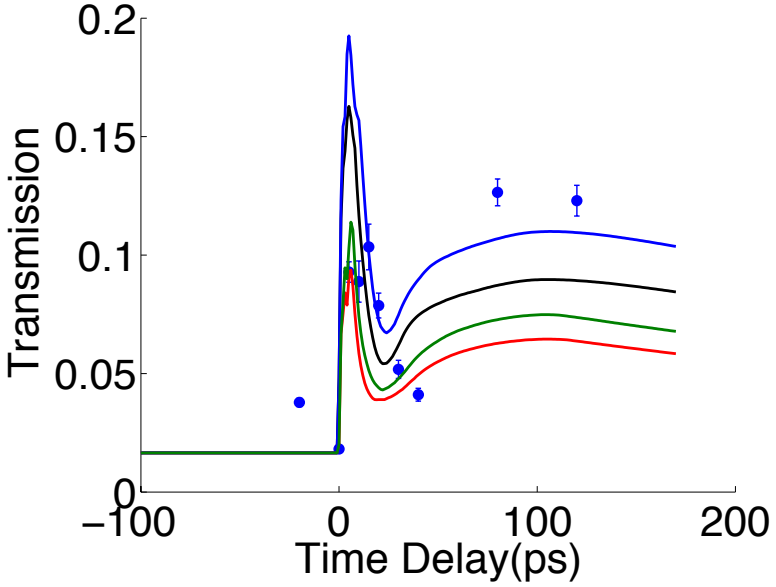

FIGURE 6.14: The transmission of the EUV laser through the buried iron layer without a prepulse. In the superimposed HYADES simulations the blue curve indicates radiation transport is off and hot electron is on, the black curve shows radiation transport and hot electron heating are both on, the green curve shows radiation transport and hot electron heating are both off, while the red curve shows radiation transport is on and hot electron transport is off. The flux limiter is set at 0.05.

eV (see figure 6.15(b)). This does not affect modelling of the radiation heating of the iron layer as the parylene-N overlay strongly absorbs photons of energy < 30 eV and the radiation does not penetrate to the iron layer.

The large expanding coronal plasma produced with the pre-pulse incident 20 ps before the main pulse reaches peak temperatures of ≈ 25 eV and consequently radiates significant radiation in the 50 - 200 eV photon energy range. Figure 6.15(b) shows that this radiation is absorbed strongly in the buried iron layer and acts to heat the iron alongside thermal conduction. Our simulations (figure 6.7) show that turning off radiation transfer in the HYADES code makes it impossible to obtain simulated EUV laser transmission values in agreement with the experimentally measured values. However, without a pre-pulse, the expanding coronal plasma size is much smaller and has a much smaller heating effect on the iron layer with a consequent much smaller effect on the EUV laser transmission (figure 6.14).

6.3.2 The accuracy of the iron opacity and the effects of oxygen impurity in the iron layer.

Figures 6.15(b) and 6.15(c) show that at the probing radiation photon energy (89eV), different opacity models agree reasonably well with the IMP opacity used for the evaluation of the EUV transmission. However, there are absorption lines centred at nearby photon energies arising from Fe^{6+} and Fe^{7+} ions $(90 - 100$ eV) [127, 128] and Fe^{7+} $(70 - 85$ eV) [129] which may affect the absorption at 89 eV. Potential broadening of the $\Delta n = 0$ transitions found within the photon range $(70 - 85$ eV) could also increase the opacity for the 89 eV EUV photons [128].

A $70-85$ eV absorption peak can be clearly seen on figure 6.15(c) for the Propaceos and TOPS opacities, but is not seen as prominently in the IMP or the HYADES code opacities. Increasing the opacity for the plasma conditions found at time 20 ps (i.e temperatures close to 20 eV and densities close to $\rho \approx 0.3$ gcm^{-3}, see figure 6.10) in post-processor modelling of the transmission of the 89 eV radiation from $\simeq 6 \times 10^4$ cm^{2}g^{-1} to $\simeq 1.1 \times 10^5$ cm^{2}g^{-1} gives a significantly better agreement of the modelled transmission with our experimental transmissions (figure 6.19). The opacity increase was implemented by increasing the 20 eV, 0.3 gcm^{-3} opacity value in a look-up table (see figure 6.17) used to post-process the 89 eV transmission to $\simeq 1.1 \times 10^5$ cm^{2}g^{-1} and leaving other IMP opacity values spaced at 10eV and 0.1 gcm^{-3} intervals unaffected. There is recent evidence that opacity values for iron may be systematically underestimated in opacity simulations [73].

Although the buried iron targets are tamped with plastic layers, oxygen can seep through the plastic over time and form iron oxide. Iron accounts for a quarter of the total opacity in the solar convection zone. Elements such as hydrogen, helium nitrogen, oxygen and carbon significantly contribute to the overall opacity of the sun [70]. In chapter 4 the emissivity of oxygen Ly-α and He-α lines were used to

predict the level of iron oxide. The targets used in chapter 4 were tamped with a frontside plastic layer of similar thickness ($\simeq$ 77 nm) compared to the targets used in this chapter ($\simeq$ 39 nm). Assuming a 10% fraction of iron oxide is present, as envisaged by the emission spectroscopy analysis in chapter 4, the radiation absorption due to oxygen is shown as a function of photon energy in figure 6.16 as calculated by the PROPACEOS code. The radiation absorption due to oxygen at 89 eV is negligible compared to the iron absorption for our measured 10% fraction[1] of oxygen in the iron layer.

The transmission through the buried iron target was investigated using an opacity look-up table calculated using the prism opacity and equation of state (PROPACEOS) code. A comparison of the opacity of the 89 eV EUV laser calculated using IMP and PROPACEOS opacity look up tables is shown in figures 4.16 and 4.15. , and figure 4.15 shows the transmission through the iron layer simulated using the PROPACEOS opacity look-up table. The iron opacity simulated by PROPACEOS is typically higher overall than the IMP opacity. As both IMP and PROPACEOS use statistical atomic models $\Delta n = 0$ transitions are not incorporated into the opacity model, therefore the transmission dip located $\approx$ 20 ps is not simulated accurately. However, overall IMP opacity better predicts the temporal change in transmission of the 89 eV EUV photons through the 50 nm thick iron layer compared to PROPACEOS.

[1]The measured fraction of oxygen is quoted as the mass percentage

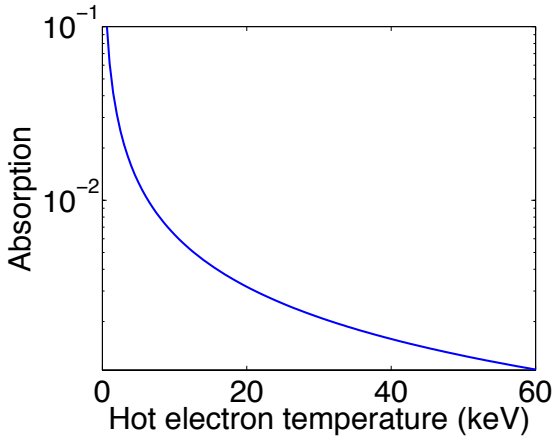

(a)

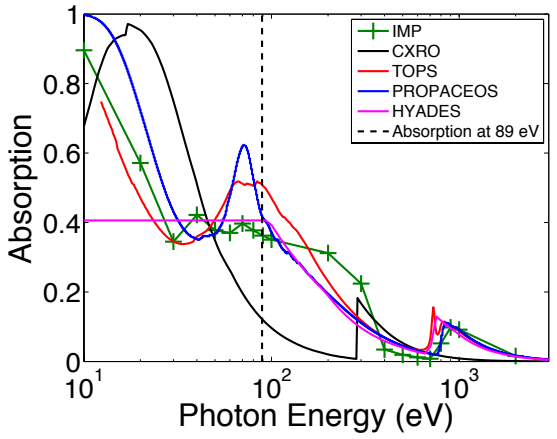

(b)

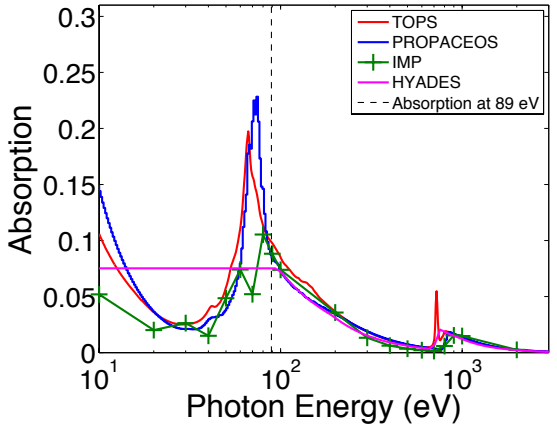

(c)

FIGURE 6.15: (a) Hot electron absorption as a function of hot electron temperature in the iron layer, (b) and (c) show radiation absorption as a function of photon energy for the 50 nm thick iron layer utilised in the experiments. The radiation absorption is calculated using IMP, TOPS, Propaceos and the HYADES in-line opacity models for iron at an electron temperature and density of (b) 30 eV and 2 gcm^{-3} and (c) 20 eV and 0.3 gcm^{-3}. The black line in (b) indicates the absorption of the 50 nm iron layer at solid density and room temperature using the CXRO filter transmission data.

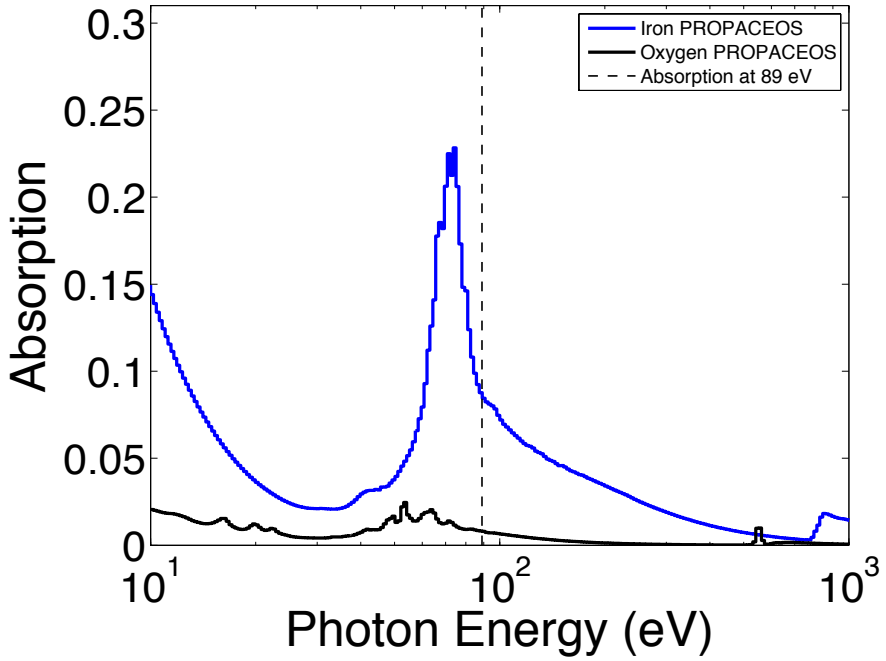

FIGURE 6.16: The radiation absorption due to iron (blue) and oxygen (black) for a 50 nm thick iron layer calculated using the PROPACEOS code. Assumed plasma conditions are 20 eV and 0.3 gcm^{-3} as found in the buried iron layer 20 ps after laser irradiation for the experiments described in this chapter. The iron is assumed to contain 10% oxygen (by weight) as found in chapter 4.

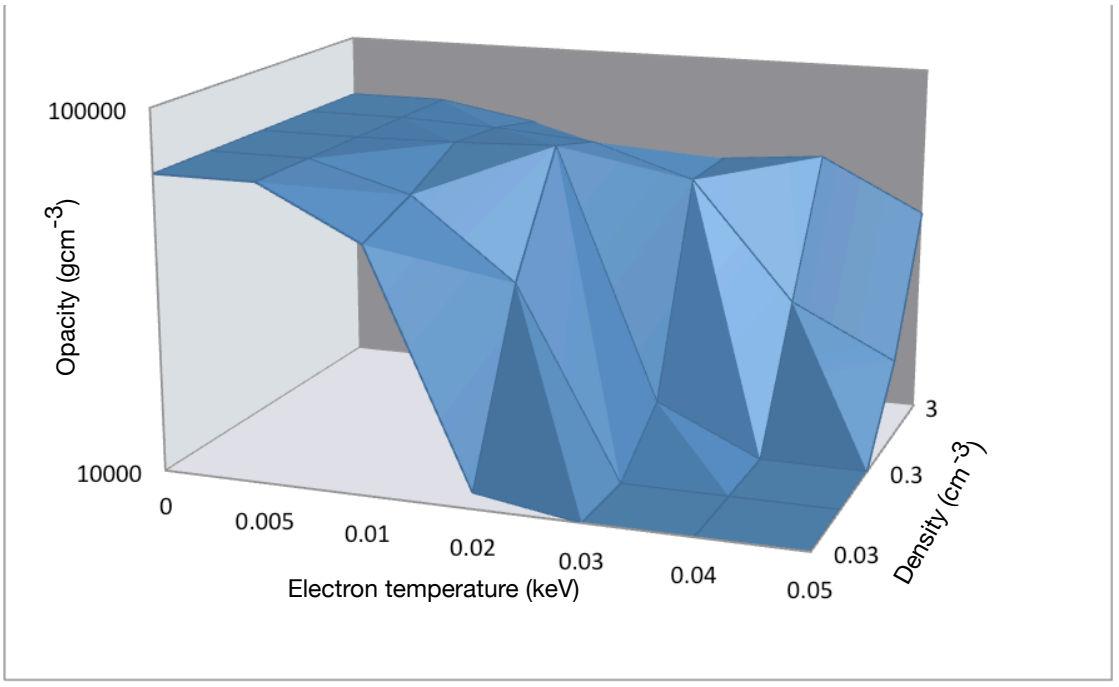

(a)

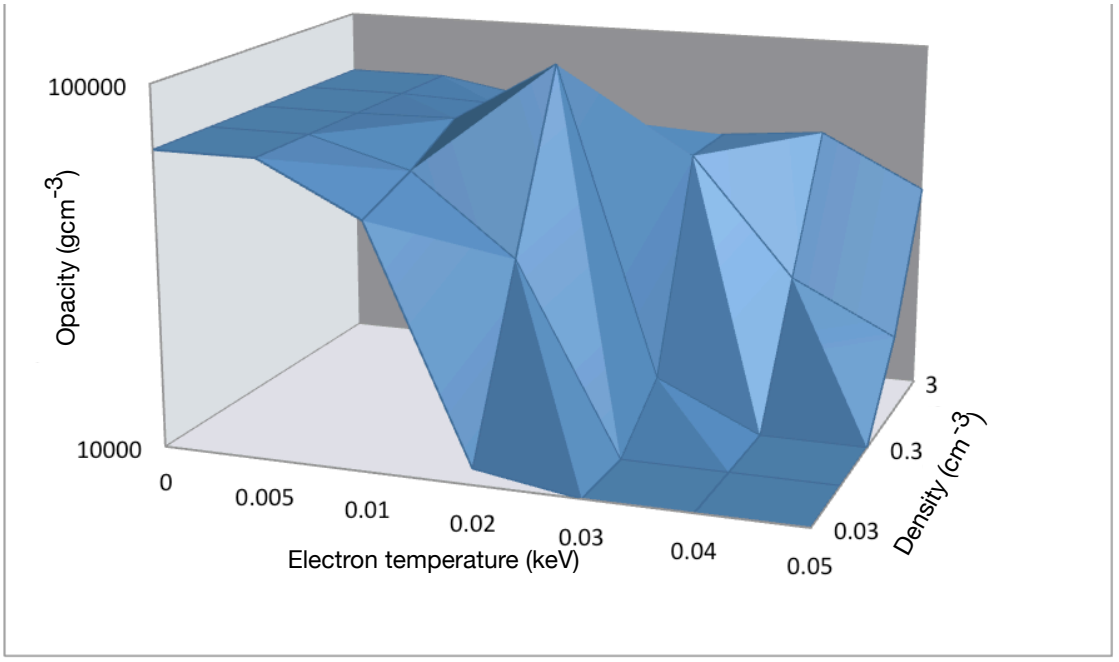

(b)

FIGURE 6.17: (a) Ionised material package (IMP) iron opacity as a function of mass density and electron temperature, T_e. (b) Modified IMP opacity look up table representing higher iron opacities at 20 eV, 0.3 gcm^{-3}. Values are calculated for 89 eV photon energy.

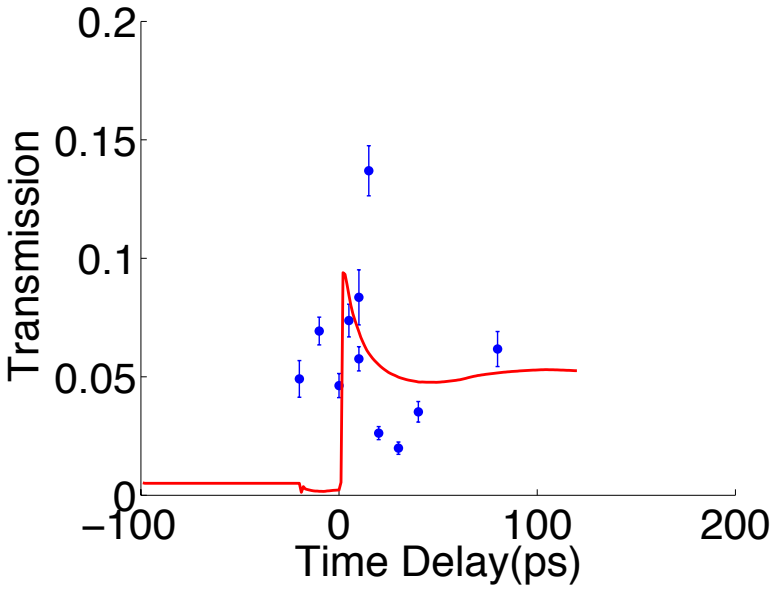

FIGURE 6.18: The transmission through the buried iron layered target is simulated using HYADES and PROPACEOS opacity. The overall larger iron opacities predicted by PROPACEOS do not accurately simulate the experimentally recorded transmission.

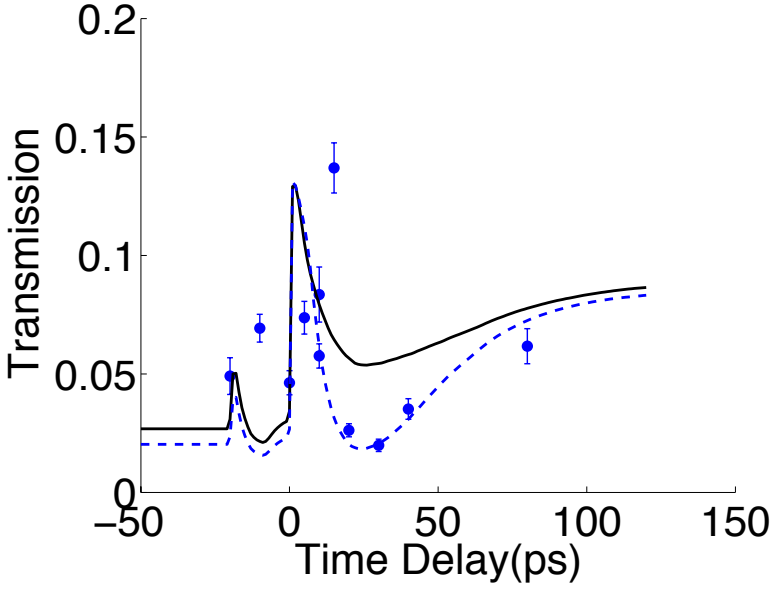

FIGURE 6.19: Simulated transmission of 89 eV radiation through the buried iron layer targets as a function of time superimposed with the experimentally measured values. Results using IMP opacities (solid black curve) and a modified opacity (dashed blue curve) are shown. The modified opacity increased opacity for iron conditions close to 20 eV and 0.3 gcm^{-3} from $\simeq 6 \times 10^4$ $\mathrm{cm}^2\mathrm{g}^{-1}$ to $\simeq 1.1 \times 10^5$ $\mathrm{cm}^2\mathrm{g}^{-1}$. The transmission profiles are simulated with a flux limiter value of 0.05 and hot electron energy dump of 10% with the infra-red laser incident at 18° to target normal.

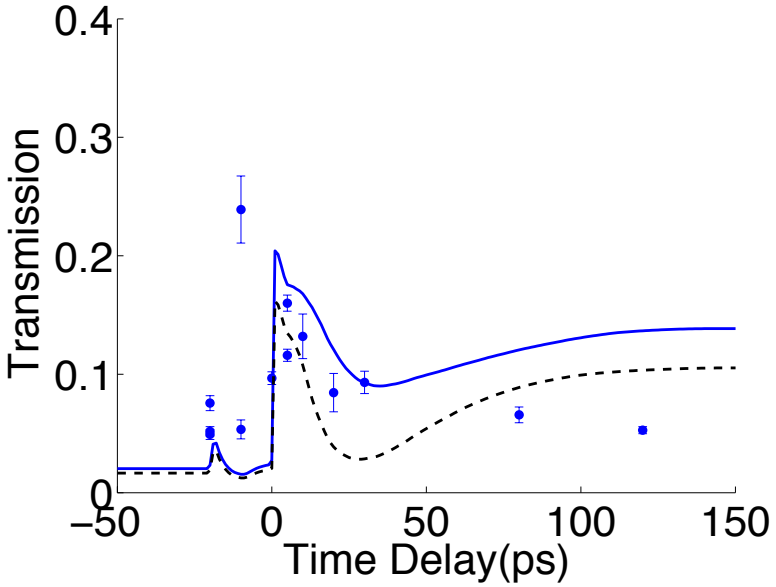

FIGURE 6.20: Same as figure 6.19 except the laser incident angle is 28° from target normal.

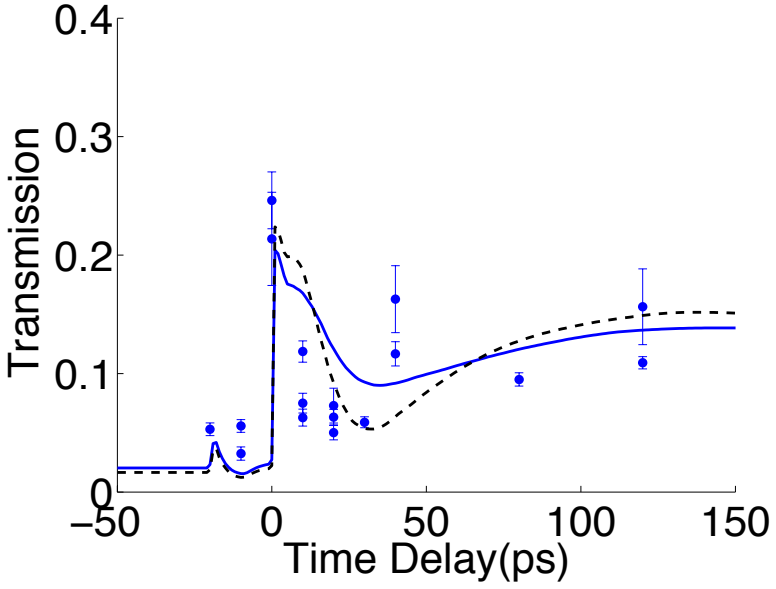

FIGURE 6.21: Same as figure 6.19 except the laser incident angle is 33° from target normal.

6.4 Conclusion

Targets containing a thin layer of iron (50 nm thick) encased in plastic have been irradiated by a short pulse (35 fs) laser focussed to irradiances 3×10^{16} Wcm^{-2}. Probing by an extreme ultraviolet (EUV) laser at wavelength 13.9 nm has enabled a measurement of the transmission of the targets which is dominated by the transmission of the iron layer. The iron layer opacity drops significantly when iron is heated and ionized to Fe^{5+} and above, where the ionisation energy is greater than the photon energy of radiation (89 eV). One dimensional fluid modelling with an opacity post-processor has shown that with a pre-pulse at level of 10% of the irradiance timed 20 ps before the main pulse, radiation heating from the emission of coronal plasma dominates the energy transport to the buried iron layer. Without a pre-pulse, radiation heating of the target is not significant. Our work illustrates the complex interplay between radiation, hot electrons and thermal electrons in heat transfer into solid targets during laser irradiation and shows that it is important to benchmark simulation codes with experimental measurements to enable the contributions from different energy transport mechanisms to be evaluated. Our work suggests that the opacity of iron at 89 eV for electron temperature 20 eV and 0.3 gcm^{-3} is higher than calculated by some models with a value $\simeq 1.1 \times 10^5$ $\mathrm{cm}^2\mathrm{g}^{-1}$.

Chapter 7

Conclusion

This thesis has investigated energy transport in high density laser produced plasmas using buried iron layer targets with a high resolution grating spectrometer (HRGS) and an extreme ultraviolet (EUV) laser as diagnostic tools. As optical lasers propagates upto the critical density, the buried iron layer is heated by energy transport mechanisms that subsequently ensue between the critical density and the ablation surface. By probing with an EUV laser and recording the characteristic L-shell emission of the iron layer, the energy transport mechanisms of radiation transport, hot electron heating and thermal electron conduction have been diagnosed.

The irradiation of buried layer targets with short pulsed lasers offer the possibility of producing high density and temperature plasmas with limited temporal and spatial gradients. Using Kirchoff's law plasma opacity can be inferred from the emissivity of the plasma when at local thermodynamic equilibrium [13]. Prior to the development of short pulsed lasers opacity experiments were limited to plasma temperatures in the range 50 - 150 eV [16]. The Atomic Weapons Establishment (AWE) has investigated the heating of buried layer targets using a short pulse laser and buried layer targets in order to benchmark opacity data at much higher

temperature ($T_e > 500$ eV) and density ($\sim 10^{24}$ cm^{-3}) conditions [14, 15]. An investigation by AWE irradiated aluminium buried layer targets using a frequency doubled laser, and K-shell spectroscopy was used to deduce plasma conditions (~ 450 eV) [17]. As part of a collaboration with AWE, this thesis extended this concept to higher Z buried iron layers and used L-shell spectroscopy to characterise temperature and density conditions [18].

Chapters 2 and 3 introduced concepts related to laser-plasma interactions, energy transport, plasma ionisation, spectroscopy and opacity. Chapter 4 detailed how the high resolution grating spectrometer was calibrated for measuring L-shell iron emission spectra. The general features and properties of the extreme ultraviolet laser, which was used to probe the buried iron layer was also discussed. The HYADES one-dimensional hydrodynamic fluid code and the collisional-radiative PrismSPECT code have been introduced. A description of the opacity codes (TOPS, PROPACEOS and IMP) which have been used to simulate the radiation absorption and transmission of the buried iron layer target are also given in chapter 4.

Chapter 5 describes the investigation at the Lawrence Livermore National Laboratory where buried iron layer targets were irradiated by 2 ps, $\sim 10^{17} - 10^{18}$ Wcm^{-2}, 0.5μm laser pulses to record time-integrated L-shell iron spectra, using a high resolution 1400 lines/mm variable line-spaced grating spectrometer. The HYADES code simulated the iron layer conditions and this data was post-processed by the collisional-radiative PrismSPECT code to produce synthetic L-shell spectra. Simulations have shown that the iron layer rapidly ionises to the Li-like state, but as the iron layer cools the emission of lower ionisation states increases. Simulations have shown that the population abundance of Li-like iron is directly dependent on hot electron heating. Therefore, the intensity of Li-like lines can be used to

diagnose the laser energy-hot electron conversion efficiency. A comparison between experimental and simulated L-shell spectra has shown that the iron layer reaches local thermodynamic equilibrium conditions. The Saha equation was used to deduce the peak electron temperature ($\sim$ 700 eV) and density (10^{24} cm^{-3}) conditions of the iron layer by taking multiple line ratios of adjacent ionisation states. To improve on the work presented in this chapter a streak camera could be used to benchmark the simulations performed in this thesis, by recording L-shell iron emission as a function of time.

Chapter 6 investigated the interplay between non-linear energy transport mechanisms by probing the buried iron layer target using an extreme ultraviolet laser. A switch in opacity in the iron layer as it is heated to Fe^{5+} or higher ionisation allows the EUV laser to use the temporal change in transmission of the iron layer as a probe of ionisation and temperature. This investigation has shown that irradiating buried iron layer targets with a deliberate prepulse produces a radiation dominated energy transport regime, compared to when an inadvertent pedestal prepulse is present. This work has shown the importance of benchmarking simulation codes to experimental measurements so that the contribution of different energy transport mechanisms can be accurately modelled.

A source of error in the simulated EUV laser transmission is the iron opacity. Simulating opacities for high Z materials like iron is particularly challenging because of the difficulty in formulating an atomic model which includes a sufficient number of electronic transitions to model opacity accurately, but also is computationally fast for everyday use. In this thesis, the radiation absorption in the iron layer was simulated using a wide range of opacity codes (IMP, PROPACEOS, TOPS and HYADES). A comparison between them has shown the importance of including $\Delta n = 0$ and resonant transitions, which can considerably increase the opacity in the iron layer, within the 70 - 90 eV spectral photon region. Recently,

experimental measurements have predicted iron opacities to be 50 - 300 % higher than previously measured [73]. This thesis also supports this claim as the drop in iron transmission at 20 ps was simulated when the iron opacity was artificially increased (in a look up table) by 100% at plasma conditions (20 eV and 0.3 gcm^{-3}) which correspond to the iron layer 20 ps after laser irradiation.

For plasmas which are produced with laser intensities below $\sim 10^{14}$ Wcm^{-2}, energy transport is dominated by radiation and thermal electron conduction. However, as lasers have became increasingly more powerful, other transport mechanisms become important, such as hot electron heating. As laser technology improves it is expected that lasers could reach intensities greater than $\sim 10^{25}$ Wcm^{-2}, which may produce quantum electrodynamic (QED) plasmas. Under such extreme laser intensities radiation transport will still play a significant role in the transfer of energy. Some of the techniques developed in this thesis could be used to diagnose energy transport in such high irradiance experiments. It is also lately that more comprehensive models of thermal energy transport will be developed and incorporated in radiation-hydrodyanmic codes. Examples of code development may include embedded Fokker-Planck modelling of thermal energy transport which will eliminate the need for flux limiter estimates. Such codes will need experimental verification using, for example the methods developed in this thesis.

Appendix A

List of publications

M. Shahzad, G. J. Tallents, A. B. Steel, L. Hobbs, D. J. Hoarty, and J. Dunn. "Electron temperature and density characterization using L-shell spectroscopy of laser irradiated buried iron layer targets." Physics of Plasmas (1994-present) 21, no. 8 (2014): 082702.

M. Shahzad, O. Culfa, A. K. Rossall, L. A. Wilson, O. Guilbaud, S. Kazamias, O. Delmas et al. "Diagnosis of energy transport in iron buried layer targets using an extreme ultraviolet laser." Physics of Plasmas (1994-present) 22, no. 2 (2015): 023301.

M. Shahzad, G.J Tallents, O. Culfa, A. K. Rossall, L. A. Wilson, S.J. Rose, O. Guilbaud, S. Kazamias, M. Pittman et al. "Diagnosis of radiation heating in iron buried layer targets." X-Ray Lasers 2014: Proceedings of the 14th International Conference on X-Ray Lasers, 2630 May 2014, Colorado, USA. Vol. 148. Springer Science & Business Media, 2014.

Tallents, G. J., M. Shahzad, A. K. Rossall, O. Guilbaud, S. Kazamias, M. Pittman, K. Cassou et al. "Probing of laser-irradiated solid targets using extreme ultraviolet radiation." In SPIE Optical Engineering+ Applications, pp. 884911-884911.

International Society for Optics and Photonics, 2013.

O. Guilbaud, S. Kazamias, K. Cassou, O. Delmas, J. Demailly, O. Neveu, D. Ros, E. Baynard, M. Shahzad et al "Seeded operation of a Ne-like Titanium soft x-ray laser: beam profile, density gradient evolution, and path towards higher density gain region" X-Ray Lasers 2014: Proceedings of the 14th International Conference on X-Ray Lasers, 2630 May 2014, Colorado, USA. Vol. 148. Springer Science & Business Media, 2014.

Bibliography

[1] Anil K Pradhan and Sultana N Nahar. *Atomic astrophysics and spectroscopy*. Cambridge University Press, 2011.

[2] John H. Nuckolls. The feasibility of inertial-confinement fusion. *Physics Today*, 35(9):24, 1982. ISSN 00319228. doi: 10.1063/1.2915258. URL http://scitation.aip.org/content/aip/magazine/physicstoday/article/35/9/10.1063/1.2915258.

[3] John Lindl. Development of the indirectdrive approach to inertial confinement fusion and the target physics basis for ignition and gain. *Physics of Plasmas (1994-present)*, 2(11):3933–4024, 1995. doi: http://dx.doi.org/10.1063/1.871025. URL http://scitation.aip.org/content/aip/journal/pop/2/11/10.1063/1.871025.

[4] Stephen E Bodner, Denis G Colombant, John H Gardner, Robert H Lehmberg, Stephen P Obenschain, Lee Phillips, Andrew J Schmitt, John D Sethian, Robert L McCrory, Wolf Seka, et al. Direct-drive laser fusion: status and prospects. *Physics of Plasmas (1994-present)*, 5(5):1901–1918, 1998.

[5] Stefano Atzeni and Jürgen Meyer-ter Vehn. *The physics of inertial fusion*. Clarendon Press, 2004.

[6] H. Nishimura, T. Endo, H. Shiraga, Y. Kato, and S. Nakai. Xray emission from highz mixture plasmas generated with intense blue laser light. *Applied Physics Letters*, 62(12):1344–1346, 1993. doi: http://dx.doi.org/10.1063/1.108725. URL http://scitation.aip.org/content/aip/journal/apl/62/12/10.1063/1.108725.

[7] LJ Suter, RL Kauffman, CB Darrow, AA Hauer, H Kornblum, OL Landen, TJ Orzechowski, DW Phillion, JL Porter, LV Powers, et al. Radiation drive in laser-heated hohlraums. *Physics of Plasmas (1994-present)*, 3(5):2057–2062, 1996.

[8] Douglas C Wilson, Paul A Bradley, Nelson M Hoffman, Fritz J Swenson, David P Smitherman, Robert E Chrien, Robert W Margevicius, DJ Thoma, Larry R Foreman, James K Hoffer, et al. The development and advantages of beryllium capsules for the national ignition facility. *Physics of Plasmas (1994-present)*, 5(5):1953–1959, 1998.

[9] M. H. Edwards, D. Whittaker, P. Mistry, N. Booth, G. J. Pert, G. J. Tallents, B. Rus, T. Mocek, M. Koslová, C. McKenna, A. Delserieys, C. L. S. Lewis, M. Notley, and D. Neely. Opacity measurements of a hot iron plasma using an x-ray laser. *Phys. Rev. Lett.*, 97:035001, Jul 2006. doi: 10.1103/PhysRevLett.97.035001. URL http://link.aps.org/doi/10.1103/PhysRevLett.97.035001.

[10] G. J. Tallents, M. H. Key, P. Norreys, D. Brown, J. Dunn, and H. Baldis. Production of hot near-solid-density plasma by electron energy transport in a laser-produced plasma. *Phys. Rev. A*, 40:2857–2859, Sep 1989. doi: 10.1103/PhysRevA.40.2857. URL http://link.aps.org/doi/10.1103/PhysRevA.40.2857.

[11] C. R. D. Brown, D. J. Hoarty, S. F. James, D. Swatton, S. J. Hughes, J. W. Morton, T. M. Guymer, M. P. Hill, D. A. Chapman, J. E. Andrew, A. J. Comley, R. Shepherd, J. Dunn, H. Chen, M. Schneider, G. Brown, P. Beiersdorfer, and J. Emig. Measurements of electron transport in foils irradiated with a picosecond time scale laser pulse. *Phys. Rev. Lett.*, 106: 185003, May 2011. doi: 10.1103/PhysRevLett.106.185003. URL `http://link.aps.org/doi/10.1103/PhysRevLett.106.185003`.

[12] B. K. F. Young, B. G. Wilson, D. F. Price, and R. E. Stewart. Measurement of x-ray emission and thermal transport in near-solid-density plasmas heated by 130 fs laser pulses. *Phys. Rev. E*, 58:4929–4936, Oct 1998. doi: 10.1103/PhysRevE.58.4929. URL `http://link.aps.org/doi/10.1103/PhysRevE.58.4929`.

[13] K Nazir, SJ Rose, A Djaoui, GJ Tallents, MG Holden, PA Norreys, P Fews, J Zhang, and F Failles. X-ray spectroscopic studies of hot, dense iron plasma formed by subpicosecond high intensity krf laser irradiation. *Applied physics letters*, 69(24):3686–3688, 1996.

[14] DJ Hoarty, SF James, CRD Brown, BM Williams, T Guymer, M Hill, J Morton, D Chapman, R Shepherd, J Dunn, et al. High temperature, high density opacity measurements using short pulse lasers. In *Journal of Physics: Conference Series*, volume 244, page 012002. IOP Publishing, 2010.

[15] DJ Hoarty, P Allan, SF James, CRD Brown, LMR Hobbs, MP Hill, JWO Harris, J Morton, MG Brookes, R Shepherd, et al. Observations of the effect of ionization-potential depression in hot dense plasma. *Physical review letters*, 110(26):265003, 2013.

[16] S.J Davidson, K Nazir, S.J Rose, R Smith, and G.J Tallents. Short-pulse laser opacity measurements. *Journal of Quantitative Spectroscopy and Radiative Transfer*, 65(13):151 – 160, 2000. ISSN 0022-4073. doi: http://dx.doi.org/10.1016/S0022-4073(99)00063-1. URL http://www.sciencedirect.com/science/article/pii/S0022407399000631.

[17] D.J. Hoarty, S.F. James, H. Davies, C.R.D. Brown, J.W.O. Harris, C.C. Smith, S.J. Davidson, E. Kerswill, B.J.B. Crowley, and S.J. Rose. Heating of buried layer targets by 1 and 2 pulses using the {HELEN} {CPA} laser. *High Energy Density Physics*, 3(12):115 – 119, 2007. ISSN 1574-1818. doi: http://dx.doi.org/10.1016/j.hedp.2007.02.007. URL http://www.sciencedirect.com/science/article/pii/S1574181807000183. Radiative Properties of Hot Dense Matter.

[18] M. Shahzad, G. J. Tallents, A. B. Steel, L. Hobbs, D. J. Hoarty, and J. Dunn. Electron temperature and density characterization using l-shell spectroscopy of laser irradiated buried iron layer targets. *Physics of Plasmas (1994-present)*, 21(8):082702, 2014. doi: http://dx.doi.org/10.1063/1.4892263. URL http://scitation.aip.org/content/aip/journal/pop/21/8/10.1063/1.4892263.

[19] Jon T. Larsen and Stephen M. Lane. Hyadesa plasma hydrodynamics code for dense plasma studies. *Journal of Quantitative Spectroscopy and Radiative Transfer*, 51(12):179 – 186, 1994. ISSN 0022-4073. doi: http://dx.doi.org/10.1016/0022-4073(94)90078-7. URL http://www.sciencedirect.com/science/article/pii/0022407394900787. Special Issue Radiative Properties of Hot Dense Matter.

[20] JJ MacFarlane, IE Golovkin, PR Woodruff, DR Welch, BV Oliver, TA Mehlhorn, and RB Campbell. Simulation of the ionization dynamics

of aluminum irradiated by intense short-pulse lasers. In *Proc. Inertial Fusion and Sciences Applications*, volume 457, 2003.

[21] GJ Pert. Hybrid model and its application for studying free expansion. *Journal of Fluid Mechanics*, 131:401–26, 1983.

[22] Simon Hooker. *Laser Physics*. OUP Oxford, 2010.

[23] CN Danson, PA Brummitt, RJ Clarke, JL Collier, B Fell, AJ Frackiewicz, S Hancock, S Hawkes, C Hernandez-Gomez, P Holligan, et al. Vulcan petawattan ultra-high-intensity interaction facility. *Nuclear Fusion*, 44(12): S239, 2004.

[24] Charles E Cook. Pulse compression-key to more efficient radar transmission. *Proceedings of the IRE*, 48(3):310–316, 1960.

[25] Olivier Delmas, Moana Pittman, Kevin Cassou, Olivier Guilbaud, Sophie Kazamias, Gabriel V. Cojocaru, Olivier Neveu, Julien Demailly, Elsa Baynard, Daniel Ursescu, and David Ros. Q-switched laser-assisted grazing incidence pumping (qagrip) for efficient soft x-ray laser generation. *Opt. Lett.*, 39(21):6102–6105, Nov 2014. doi: 10.1364/OL.39.006102. URL `http://ol.osa.org/abstract.cfm?URI=ol-39-21-6102`.

[26] James Dunn, Albert L Osterheld, Yuelin Li, Joseph Nilsen, and Vyacheslav N Shlyaptsev. Transient collisional excitation x-ray lasers with 1-ps tabletop drivers. *Selected Topics in Quantum Electronics, IEEE Journal of*, 5(6):1441–1446, 1999.

[27] Konstantin Moskalik, Alexander Kozlov, Eugeny Demin, and Ernest Boiko. The efficacy of facial skin cancer treatment with high-energy pulsed neodymium and nd: Yag lasers. *Photomedicine and laser surgery*, 27(2): 345–349, 2009.

[28] Lung Kwang Pan, Che Chung Wang, Ying Ching Hsiao, and Kye Chyn Ho. Optimization of nd: Yag laser welding onto magnesium alloy via taguchi analysis. *Optics & Laser Technology*, 37(1):33–42, 2005.

[29] James Dunn, Joseph Nilsen, Albert L Osterheld, Yuelin Li, and Vyacheslav N Shlyaptsev. Demonstration of transient gain x-ray lasers near 20nm for nickellike yttrium, zirconium, niobium, and molybdenum. *Optics letters*, 24(2):101–103, 1999.

[30] R Paul Drake. *High-energy-density physics: fundamentals, inertial fusion, and experimental astrophysics*. Springer Science & Business Media, 2006.

[31] William L Kruer. *The physics of laser plasma interactions*. Reading, MA (US); Addison-Wesley Publishing Co., 1988.

[32] LV Keldysh. Ionization in the field of a strong electromagnetic wave. *Sov. Phys. JETP*, 20(5):1307–1314, 1965.

[33] Jeff Colvin and Jon Larsen. *Extreme Physics: Properties and Behavior of Matter at Extreme Conditions*. Cambridge University Press, 2013.

[34] Paul Gibbon. *Short pulse laser interactions with matter*. World Scientific Publishing Company, 2004.

[35] Jérôme Faure, Yannick Glinec, A Pukhov, S Kiselev, S Gordienko, E Lefebvre, J-P Rousseau, F Burgy, and Victor Malka. A laser–plasma accelerator producing monoenergetic electron beams. *Nature*, 431(7008):541–544, 2004.

[36] K.B. Fournier, B.K.F. Young, S.J. Moon, M.E. Foord, D.F. Price, R.L. Shepherd, and P.T. Springer. Characterization of time resolved, buried layer plasmas produced by ultrashort laser pulses. *Journal of Quantitative Spectroscopy and Radiative Transfer*, 71(26):339 – 354, 2001. ISSN 0022-4073. doi: http://dx.doi.org/10.1016/S0022-4073(01)00080-2. URL `http://www.`

sciencedirect.com/science/article/pii/S0022407301000802. Radiative Properties of Hot Dense Matter.

[37] F Brunel. Not-so-resonant, resonant absorption. *Physical Review Letters*, 59 (1):52, 1987.

[38] Erich S Weibel. Anomalous skin effect in a plasma. *Physics of Fluids (1958-1988)*, 10(4):741–748, 1967.

[39] Sha Liu, XF Xu, RG Xie, Gang Zhang, and BW Li. Anomalous heat conduction and anomalous diffusion in low dimensional nanoscale systems. *The European Physical Journal B-Condensed Matter and Complex Systems*, 85 (10):1–20, 2012.

[40] Lyman Spitzer Jr and Richard Härm. Transport phenomena in a completely ionized gas. *Physical Review*, 89(5):977, 1953.

[41] Richard O Dendy. *Plasma physics: an introductory course*. Cambridge University Press, 1995.

[42] Shalom Eliezer. *The interaction of high-power lasers with plasmas*. CRC Press, 2002.

[43] DH Froula, JS Ross, BB Pollock, P Davis, AN James, L Divol, MJ Edwards, AA Offenberger, D Price, RPJ Town, et al. Quenching of the nonlocal electron heat transport by large external magnetic fields in a laser-produced plasma measured with imaging thomson scattering. *Physical review letters*, 98(13):135001, 2007.

[44] J Delettrez. Thermal electron transport in direct-drive laser fusion. *Canadian Journal of Physics*, 64(8):932–943, 1986.

[45] AR Bell, RG Evans, and DJ Nicholas. Elecron energy transport in steep temperature gradients in laser-produced plasmas. *Physical Review Letters*, 46(4):243, 1981.

[46] P. Martín and J. Puerta. *Plasma Physics*. Kluwer, 1998. URL `http://books.google.co.uk/books?id=dpmGnAEACAAJ`.

[47] Michael B Hooper. *Laser-Plasma Interactions 4*, volume 35. CRC Press, 1989.

[48] D Duston, RW Clark, J Davis, and JP Apruzese. Radiation energetics of a laser-produced plasma. *Physical Review A*, 27(3):1441, 1983.

[49] FN Beg, AR Bell, AE Dangor, CN Danson, AP Fews, ME Glinsky, BA Hammel, P Lee, PA Norreys, and Ma Tatarakis. A study of picosecond laser–solid interactions up to 1019 w cm- 2. *Physics of Plasmas (1994-present)*, 4(2): 447–457, 1997.

[50] Anthony L Meadowcroft and Ray D Edwards. High-energy bremsstrahlung diagnostics to characterize hot-electron production in short-pulse laser-plasma experiments. *Plasma Science, IEEE Transactions on*, 40(8):1992–2001, 2012.

[51] Ozgur Culfa. Measurements of hot electron spectra from high irradiance laser plasmas. 2014.

[52] GJ Tallents, M Shahzad, AK Rossall, O Guilbaud, S Kazamias, M Pittman, K Cassou, J Demailly, O Delmas, A Mestrallain, et al. Probing of laser-irradiated solid targets using extreme ultraviolet radiation. In *SPIE Optical Engineering+ Applications*, pages 884911–884911. International Society for Optics and Photonics, 2013.

[53] Andrew Rossall. *Characterisation and Measurement of Laser Produced Plasma Emission and Applications in Opacity Experiments.* University of York, 2011.

[54] MH Key, MD Cable, TE Cowan, KG Estabrook, BA Hammel, SP Hatchett, EA Henry, DE Hinkel, JD Kilkenny, JA Koch, et al. Hot electron production and heating by hot electrons in fast ignitor research. *Physics of Plasmas (1994-present)*, 5(5):1966–1972, 1998.

[55] V Aslanyan and GJ Tallents. Local thermodynamic equilibrium in rapidly heated high energy density plasmas. *Physics of Plasmas (1994-present)*, 21 (6):062702, 2014.

[56] Hans R Griem. Principles of plasma spectroscopy. *Proceedings of the Physical Society*, 1, 2005.

[57] O Ciricosta, SM Vinko, H-K Chung, B-I Cho, CRD Brown, T Burian, J Chalupskỳ, K Engelhorn, RW Falcone, C Graves, et al. Direct measurements of the ionization potential depression in a dense plasma. *Physical review letters*, 109(6):065002, 2012.

[58] Sang-Kil Son, Robert Thiele, Zoltan Jurek, Beata Ziaja, and Robin Santra. Quantum-mechanical calculation of ionization-potential lowering in dense plasmas. *Physical Review X*, 4(3):031004, 2014.

[59] David Salzmann. *Atomic physics in hot plasmas.* Oxford University Press, 1998.

[60] Balazs F Rozsnyai. Collisional-radiative average-atom model for hot plasmas. *Physical Review E*, 55(6):7507, 1997.

[61] WR Johnson, C Guet, and GF Bertsch. Optical properties of plasmas based on an average-atom model. *Journal of Quantitative Spectroscopy and Radiative Transfer*, 99(1):327–340, 2006.

[62] SJ Rose. Calculations of the radiative opacity of laser-produced plasmas. *Journal of Physics B: Atomic, Molecular and Optical Physics*, 25(7):1667, 1992.

[63] G Faussurier, Ch Blancard, and E Berthier. Nonlocal thermodynamic equilibrium self-consistent average-atom model for plasma physics. *Physical Review E*, 63(2):026401, 2001.

[64] John M. Harlander and Fred L. Roesler. Spatial heterodyne spectroscopy: a novel interferometric technique for ground-based and space astronomy. *Proc. SPIE*, 1235:622–633, 1990. doi: 10.1117/12.19125. URL `http://dx.doi.org/10.1117/12.19125`.

[65] M. C. McCarthy, C. A. Gottlieb, H. Gupta, and P. Thaddeus. Laboratory and astronomical identification of the negative molecular ion c6h. *The Astrophysical Journal Letters*, 652(2):L141, 2006. URL `http://stacks.iop.org/1538-4357/652/i=2/a=L141`.

[66] Hans-Joachim Kunze. *Introduction to plasma spectroscopy*, volume 56. Springer, 2009.

[67] WC Martin, J Sugar, A Musgrove, GR Dalton, WL Wiese, JR Fuhr, and DE Kelleher. Nist database for atomic spectroscopy. *NIST, Gaithersburg-MD*, 1995.

[68] J Dunn, E W Magee, R Shepherd, H Chen, S B Hansen, S J Moon, G V Brown, M-F Gu, P Beiersdorfer, and M A Purvis. High resolution soft x-ray spectroscopy of low Z K-shell emission from laser-produced plasmas.

The Review of scientific instruments, 79(10):10E314, October 2008. ISSN 1089-7623. doi: 10.1063/1.2968704. URL http://www.ncbi.nlm.nih.gov/pubmed/19044476.

[69] Walter F Huebner and W David Barfield. *Opacity*. Springer, 2014.

[70] JE Bailey, GA Rochau, RC Mancini, CA Iglesias, JJ MacFarlane, IE Golovkin, C Blancard, Ph Cosse, and G Faussurier. Experimental investigation of opacity models for stellar interior, inertial fusion, and high energy density plasmasa). *Physics of Plasmas (1994-present)*, 16(5):058101, 2009.

[71] Martin Asplund, Nicolas Grevesse, A Jacques Sauval, and Pat Scott. The chemical composition of the sun. *arXiv preprint arXiv:0909.0948*, 2009.

[72] Elisabetta Caffau, H-G Ludwig, Matthias Steffen, Bernd Freytag, and Piercarlo Bonifacio. Solar chemical abundances determined with a co5bold 3d model atmosphere. *Solar Physics*, 268(2):255–269, 2011.

[73] JE Bailey, T Nagayama, GP Loisel, GA Rochau, C Blancard, J Colgan, Ph Cosse, G Faussurier, CJ Fontes, F Gilleron, et al. A higher-than-predicted measurement of iron opacity at solar interior temperatures. *Nature*, 517 (7532):56–59, 2015.

[74] LB Da Silva, TW Barbee Jr, R Cauble, P Celliers, D Ciarlo, S Libby, RA London, D Matthews, S Mrowka, JC Moreno, et al. Electron density measurements of high density plasmas using soft x-ray laser interferometry. *Physical Review Letters*, 74(20):3991, 1995.

[75] L. A. Wilson, G. J. Tallents, J. Pasley, D. S. Whittaker, S. J. Rose, O. Guilbaud, K. Cassou, S. Kazamias, S. Daboussi, M. Pittman, O. Delmas,

J. Demailly, O. Neveu, and D. Ros. Energy transport in short-pulse-laser-heated targets measured using extreme ultraviolet laser backlighting. *Phys. Rev. E*, 86:026406, Aug 2012. doi: 10.1103/PhysRevE.86.026406. URL `http://link.aps.org/doi/10.1103/PhysRevE.86.026406`.

[76] CJ Keane, BA Hammel, DR Kania, JD Kilkenny, RW Lee, AL Osterheld, LJ Suter, RC Mancini, CF Hooper Jr, and ND Delamater. X-ray spectroscopy of high-energy density inertial confinement fusion plasmas. *Physics of Fluids B: Plasma Physics (1989-1993)*, 5(9):3328–3336, 1993.

[77] M Shahzad, O Culfa, AK Rossall, LA Wilson, O Guilbaud, S Kazamias, O Delmas, J Demailly, A Maitrallain, M Pittman, et al. Diagnosis of energy transport in iron buried layer targets using an extreme ultraviolet laser. *Physics of Plasmas (1994-present)*, 22(2):023301, 2015.

[78] Christopher Palmer, Erwin G Loewen, and RGL Thermo. *Diffraction grating handbook*. Milton Roy, 1994.

[79] A. Cornu. Sur la diffraction proprietes focales des reseaux. *C.R. Acad. Sci. (Paris)*, 80:645, 1875.

[80] Michael C Hettrick. Varied line-space gratings: past, present and future. In *29th Annual Technical Symposium*, pages 96–108. International Society for Optics and Photonics, 1986.

[81] David Attwood. *Soft x-rays and extreme ultraviolet radiation: principles and applications*. Cambridge university press, 1999.

[82] Yu Ralchenko, AE Kramida, and J Reader. Nist atomic spectra database (version 4.0). *National Institute of Standards and Technology, Gaithersburg, MD*, 2010.

[83] BC Fawcett, A Ridgeley, and TP Hughes. Line classifications for ni xxv and xxvi and new observations of fe xxiii and xxiv in laser-produced spectra. *Monthly Notices of the Royal Astronomical Society*, 188(2):365–370, 1979.

[84] Wolfgang Lothar Wiese, JR Fuhr, and TM Deters. Atomic transition probabilities of carbon, nitrogen, and oxygen: A critical data compilation. *Atomic transition probabilities of carbon, nitrogen, and oxygen: a critical data compilation. Edited by WL Wiese, JR Fuhr, and TM Deters. Washington, DC: American Chemical Society... for the National Institute of Standards and Technology (NIST) c1996. QC 453. W53 1996. Also Journal of Physical and Chemical Reference Data, Monograph 7. Melville, NY: AIP Press*, 1, 1996.

[85] EW Magee, J Dunn, GV Brown, KV Cone, J Park, FS Porter, CA Kilbourne, RL Kelley, and P Beiersdorfer. Calibration of a high resolution grating soft x-ray spectrometera). *Review of Scientific Instruments*, 81(10):10E314, 2010.

[86] Yuelin Li, G. D. Tsakiris, and R. Sigel. Self-calibration of a thinned, back-side illuminated charge coupled devices in the soft x-ray region. *Review of Scientific Instruments*, 66(1):80, 1995. ISSN 00346748. doi: 10.1063/1.1146228. URL `http://scitation.aip.org/content/aip/journal/rsi/66/1/10.1063/1.1146228`.

[87] LMR Gartside, GJ Tallents, AK Rossall, E Wagenaars, DS Whittaker, M Kozlová, J Nejdl, M Sawicka, J Polan, M Kalal, et al. Extreme ultraviolet interferometry of warm dense matter in laser plasmas. *Optics letters*, 35(22): 3820–3822, 2010.

[88] JE Bailey, GA Rochau, CA Iglesias, J Abdallah Jr, JJ MacFarlane, I Golovkin, P Wang, RC Mancini, PW Lake, TC Moore, et al. Iron-plasma

transmission measurements at temperatures above 150 ev. *Physical review letters*, 99(26):265002, 2007.

[89] Davide Bleiner, Yunieski Arbelo-Pena, Leili Masoudnia, and Mabel Ruiz-Lopez. Table-top x-ray lasers using a plasma gain-medium: limits and potentials. *Physica Scripta*, 2014(T162):014050, 2014. URL `http://stacks.iop.org/1402-4896/2014/i=T162/a=014050`.

[90] Dennis L Matthews, PL Hagelstein, MD Rosen, MJ Eckart, NM Ceglio, AU Hazi, H Medecki, BJ MacGowan, JE Trebes, BL Whitten, et al. Demonstration of a soft x-ray amplifier. *Physical review letters*, 54(2):110, 1985.

[91] Pierre Jaeglé. *Coherent sources of XUV radiation: Soft X-ray lasers and high-order harmonic generation*, volume 106. Springer, 2005.

[92] MD Rosen, PL Hagelstein, DL Matthews, EM Campbell, AU Hazi, BL Whitten, B MacGowan, RE Turner, RW Lee, G Charatis, et al. Exploding-foil technique for achieving a soft x-ray laser. *Physical review letters*, 54(2):106, 1985.

[93] PL Hagelstein. Review of radiation pumped soft x-ray lasers. *Plasma Physics*, 25(12):1345, 1983.

[94] BJ MacGowan, LB Da Silva, DJ Fields, CJ Keane, JA Koch, RA London, DL Matthews, S Maxon, S Mrowka, AL Osterheld, et al. Short wavelength x-ray laser research at the lawrence livermore national laboratory. *Physics of Fluids B: Plasma Physics (1989-1993)*, 4(7):2326–2337, 1992.

[95] G. Pert. Optimizing the performance of nickel-like collisionally pumped x-ray lasers. II. Lasers for the wavelength range 50100Å. *Physical Review A*, 75(2), February 2007. ISSN 1050-2947. doi: 10.1103/PhysRevA.75.023808. URL `http://link.aps.org/doi/10.1103/PhysRevA.75.023808`.

[96] GJ Tallents. The physics of soft x-ray lasers pumped by electron collisions in laser plasmas. *Journal of Physics D: Applied Physics*, 36(15):R259, 2003.

[97] J Dunn, AL Osterheld, R Shepherd, WE White, VN Shlyaptsev, and RE Stewart. Demonstration of x-ray amplification in transient gain nickel-like palladium scheme. *Physical review letters*, 80(13):2825, 1998.

[98] PJ Warwick, CLS Lewis, MP Kalachnikov, PV Nickles, M Schnürer, A Behjat, A Demir, GJ Tallents, D Neely, E Wolfrum, et al. Observation of high transient gain in the germanium x-ray laser at 19.6 nm. *JOSA B*, 15(6): 1808–1814, 1998.

[99] A Klisnick, J Kuba, D Ros, R Smith, G Jamelot, C Chenais-Popovics, R Keenan, SJ Topping, CLS Lewis, F Strati, et al. Demonstration of a 2-ps transient x-ray laser. *Physical Review A*, 65(3):033810, 2002.

[100] VG Kohn. On the theory of reflectivity by an x-ray multilayer mirror. *physica status solidi (b)*, 187(1):61–70, 1995.

[101] Henke. *Centre for X-ray Optics Lawrence Berkley National Laboratory.* Centre for X-ray Optics Lawrence Berkley National Laboratory. URL `henke.lbl.gov/optical_constants/filter2.html`.

[102] B. W and S. G. Buried channel charge coupled devices. February 12 1974. URL `http://www.google.com/patents/US3792322`. US Patent 3,792,322.

[103] K. G. McKay and K. B. McAfee. Electron multiplication in silicon and germanium. *Phys. Rev.*, 91:1079–1084, Sep 1953. doi: 10.1103/PhysRev.91.1079. URL `http://link.aps.org/doi/10.1103/PhysRev.91.1079`.

[104] J. Jr. Abdallah and R.E.H. Clark. *TOPS: a multigroup opacity code.* Oct 1985.

[105] NH Magee. New opacity library and sesame opacity data. *Los Alamos National Laboratory, Los Alamos, NM, M larch*, 30, 1993.

[106] C Bauche-Arnoult, J Bauche, and M Klapisch. Variance of the distributions of energy levels and of the transition arrays in atomic spectra. *Physical Review A*, 20(6):2424, 1979.

[107] Walter F Huebner, AL Merts, NH Magee Jr, and MF Argo. Astrophysical opacity library. Technical report, Los Alamos Scientific Lab., N. Mex.(USA), 1977.

[108] NH Magee, J Abdallah Jr, REH Clark, JS Cohen, LA Collins, G Csanak, CJ Fontes, A Gauger, JJ Keady, DP Kilcrease, et al. Atomic structure calculations and new los alamos astrophysical opacities. In *Astrophysical applications of powerful new databases*, volume 78, page 51, 1995.

[109] R Kodama, P A Norreys, K Mima, A E Dangor, R G Evans, H Fujita, Y Kitagawa, K Krushelnick, T Miyakoshi, N Miyanaga, T Norimatsu, S J Rose, T Shozaki, K Shigemori, A Sunahara, M Tampo, K A Tanaka, Y Toyama, T Yamanaka, and M Zepf. Fast heating of ultrahigh-density plasma as a step towards laser fusion ignition. *Nature*, 412(6849):798–802, August 2001. ISSN 0028-0836. URL `http://dx.doi.org/10.1038/35090525`.

[110] K. Eidmann, U. Andiel, F. Pisani, P. Hakel, R.C. Mancini, G.C. Junkel-Vives, J. Abdallah, and K. Witte. K-shell spectra from hot dense aluminum layers buried in carbon and heated by ultrashort laser pulses. *Journal of Quantitative Spectroscopy and Radiative Transfer*, 81(14):133 – 146, 2003. ISSN 0022-4073. doi: http://dx.doi.org/10.1016/S0022-4073(03)00067-0. URL `http://www.sciencedirect.com/science/article/pii/S0022407303000670`. Radiative Properties of Hot Dense Matter.

[111] Xiong Gang, ZHAO Yang, SHANG Wan-Li, HU Zhi-Min, ZHU Tuo, WEI Min-Xi, YANG Guo-Hong, ZHANG Ji-Yan, and YANG Jia-Min. K-shell spectra from ch-tamped aluminum layers irradiated with intense femtosecond laser pulses. *Chinese Physics Letters*, 27(9):95202, 2010. doi: 10.1088/0256-307X/27/9/095202. URL http://cpl.iphy.ac.cn/EN/abstract/article_33445.shtml.

[112] S. B. Hansen, A. S. Shlyaptseva, V. L. Kantsyrev, D. A. Fedin, N. D. Ouart, U. I. Safronova, and K. B. Fournier. Applications of advanced theoretical x-ray l-shell spectroscopy to various plasma and collision experiments. *Review of Scientific Instruments*, 74(3):1943–1946, 2003. doi: http://dx.doi.org/10.1063/1.1535276. URL http://scitation.aip.org/content/aip/journal/rsi/74/3/10.1063/1.1535276.

[113] A. Sunahara, J. A. Delettrez, C. Stoeckl, R. W. Short, and S. Skupsky. Time-dependent electron thermal flux inhibition in direct-drive laser implosions. *Phys. Rev. Lett.*, 91:095003, Aug 2003. doi: 10.1103/PhysRevLett.91.095003. URL http://link.aps.org/doi/10.1103/PhysRevLett.91.095003.

[114] Jonathan Mooney and Patanjali Kambhampati. Get the basics right: Jacobian conversion of wavelength and energy scales for quantitative analysis of emission spectra. *The Journal of Physical Chemistry Letters*, 4(19):3316–3318, 2013.

[115] Pi-sx 1300 ccd camera data sheet. URL http://www.princetoninstruments.com.

[116] V. Aslanyan and G. J. Tallents. Local thermodynamic equilibrium in rapidly heated high energy density plasmas. *Physics of Plasmas (1994-present)*, 21(6):062702, 2014. doi: http://dx.doi.org/10.1063/1.

4882235. URL http://scitation.aip.org/content/aip/journal/pop/21/6/10.1063/1.4882235.

[117] Thomas R. Preston, Sam M. Vinko, Orlando Ciricosta, Hyun-Kyung Chung, Richard W. Lee, and Justin S. Wark. The effects of ionization potential depression on the spectra emitted by hot dense aluminium plasmas. *High Energy Density Physics*, 9(2):258 – 263, 2013. ISSN 1574-1818. doi: http://dx.doi.org/10.1016/j.hedp.2012.12.014. URL http://www.sciencedirect.com/science/article/pii/S1574181813000049.

[118] RC Malone, RL McCrory, and RL Morse. Indications of strongly flux-limited electron thermal conduction in laser-target experiments. *Physical Review Letters*, 34(12):721, 1975.

[119] JF Luciani, P Mora, and J Virmont. Nonlocal heat transport due to steep temperature gradients. *Physical review letters*, 51(18):1664, 1983.

[120] Hector A Baldis, Kunioki Mima, and Akio Nishiguchi. *Laser plasma theory and Simulation*, volume 17. CRC Press, 1994.

[121] K Eidmann. Radiation transport and atomic physics modeling in high-energy-density laser-produced plasmas. *Laser and Particle Beams*, 12(02): 223–244, 1994.

[122] AR Bell, RG Evans, and DJ Nicholas. Elecron energy transport in steep temperature gradients in laser-produced plasmas. *Physical Review Letters*, 46(4):243, 1981.

[123] KB Wharton, SP Hatchett, SC Wilks, MH Key, JD Moody, V Yanovsky, AA Offenberger, BA Hammel, MD Perry, and C Joshi. Experimental measurements of hot electrons generated by ultraintense (¿ 10 19 w/cm 2) laser-plasma interactions on solid-density targets. *Physical Review Letters*, 81(4): 822, 1998.

[124] J Edwards, M Dunne, D Riley, R Taylor, O Willi, and SJ Rose. Time-resolved measurement of x-ray heating in plastic foils irradiated by intense soft-x-ray pulses. *Physical review letters*, 67(27):3780, 1991.

[125] O Guilbaud, A Klisnick, K Cassou, S Kazamias, D Ros, G Jamelot, D Joyeux, and Daniel Phalippou. Origin of microstructures in picosecond x-ray laser beams. *EPL (Europhysics Letters)*, 74(5):823, 2006.

[126] D Kaganovich, JR Peñano, MH Helle, DF Gordon, B Hafizi, and A Ting. Origin and control of the subpicosecond pedestal in femtosecond laser systems. *Optics letters*, 38(18):3635–3638, 2013.

[127] G Winhart, K Eidmann, CA Iglesias, A Bar-Shalom, E Minguez, A Rickert, and SJ Rose. Xuv opacity measurements and comparison with models. *Journal of quantitative spectroscopy and radiative transfer*, 54(1):437–446, 1995.

[128] LB Da Silva, BJ MacGowan, DR Kania, BA Hammel, CA Back, E Hsieh, R Doyas, CA Iglesias, FJ Rogers, and RW Lee. Absorption measurements demonstrating the importance of δn= 0 transitions in the opacity of iron. *Physical review letters*, 69(3):438, 1992.

[129] BC Fawcett and RD Cowan. 3p6 3dn-3p5 3d n+ 1 spectra of Fe vi and Fe vii. *Solar Physics*, 31(2):339–341, 1973.